

日中笹川医学奨学金制度 (学位取得コース) 評価書

論文博士：指導教官用



第 40 期

研究者番号： G4010

作成日：2020年3月15日

氏名	徐妍妍	XU YANYAN	性別	F	生年月日	1984.02.01
所属機関 (役職)	中日友好医院 放射科 (住院医師)					
研究先 (指導教官)	琉球大学大学院医学研究科 放射線診断治療学 (村山 貞之 教授) 琉球大学大学院医学研究科 放射線診断治療学 (山城 恒雄 講師)					
研究テーマ	超多列 CT, 超高精細 CT 等を用いた胸部疾患の研究					
専攻種別	<input checked="" type="checkbox"/> 論文博士			<input type="checkbox"/> 課程博士		

研究者評価 (指導教官記入欄)

成績状況	(優) 良 可 不可	取得単位数
		取得単位数 / 取得すべき単位数総数
学生本人が行った研究の概要		主として慢性閉塞性肺疾患 (COPD) の CT 画像に関する研究を行った。COPD の画像の研究に関して、2018 年度は 4 次元呼吸ダイナミック CT の研究として 2 本の英文原著論文を作成し、また 2019 年度は超高精細 CT の研究として 1 本の英文原著論文を完成させ、いずれも International Journal of Chronic Obstructive Pulmonary Disease 誌 (最新の IF で 3.274) より Publish された。時間に余裕があると中国の所属病院の画像情報を活用した独自の研究も行い、数本の英文原著論文等を完成させた。
総合評価		【良かった点】 ・積極的に研究に取り組んだ点。 ・積極的に周囲の研究者、医師等とのコミュニケーションを図った点。 ・琉球大学の博士の学位 (医学) を取得できた点。
		【改善すべき点】 ・特になし。あえて挙げれば日本語能力のさらなる向上が望ましい。
		【今後の展望】 ・中国に帰国後は、日本での研究の成果を生かして、呼吸器画像診断の研究に従事することが望まれる。特に、日本や米国の医学研究における厳格な倫理的基準、規範に則った医学研究を中国においても自ら実施し、中国の医学研究の水準向上に寄与されることを大いに期待する。
学位取得見込		2019年12月に下記論文の研究に対して論文博士 (医学) の学位審査会が開かれ、2020年1月の医学研究科教授会にて、琉球大学が博士号を授与する基準に達していると判断された。学長決済の後に2019年度中に博士 (医学) の学位記が授与される。 Xu Y, Yamashiro T, Moriya H, Muramatsu S, Murayama S. Quantitative Emphysema Measurement On Ultra-High-Resolution CT Scans. Int J Chron Obstruct Pulmon Dis. 2019;14 (1) :2283-2290. doi: 10.2147/COPD.S223605.
		評価者 (指導教官名) 村山 貞之 山城 恒雄

日中笹川医学奨学金制度(学位取得コース)報告書

研究者用



第 40 期

研究者番号: G4010

作成日: 2020 年 1 月 14 日

氏名	XU YANYAN	徐妍妍	性別	F	生年月日	1984.02.01
所属機関(役職)	中日友好医院 放射科 (住院医师)					
研究先 (指導教官)	琉球大学大学院医学研究科 放射線診断治療学 (村山 貞之 教授)		琉球大学大学院医学研究科 放射線診断治療学 (山城 恒雄 講師)			
研究テーマ	超多列 CT, 超高精細 CT 等を用いた胸部疾患の研究					
専攻種別	論文博士	<input checked="" type="checkbox"/>	課程博士	<input type="checkbox"/>		

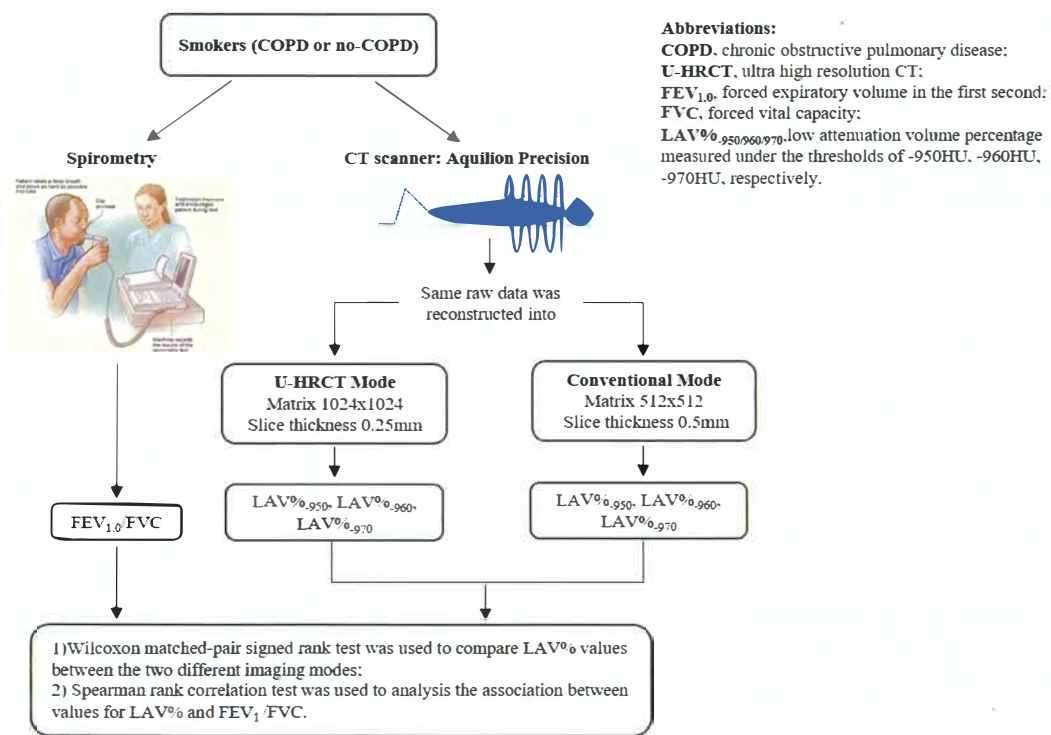
研究概要

Quantitative Emphysema Measurement On Ultra-High-Resolution CT Scans

Purpose(目的)

To evaluate the advantages of ultra-high-resolution computed tomography (U-HRCT) scans for the quantitative measurement of emphysematous lesions over conventional HRCT scans.

Approach (戦略)



Materials and methods (材料と方法)

This study included 32 smokers under routine clinical care who underwent chest CT performed by a U-HRCT scanner. Chronic obstructive pulmonary disease (COPD) was diagnosed in 13 of the 32 participants. Scan data were reconstructed by 2 different protocols: i) U-HRCT mode with a 1024×1024 matrix and 0.25-mm slice thickness and ii) conventional HRCT mode with a 512×512 matrix and 0.5-mm slice thickness. On both types of scans, lesions of emphysema were quantitatively assessed as percentage of low attenuation volume (LAV%, <-950 Hounsfield units). LAV% values determined for scan data from the U-HRCT and conventional

HRCT modes were compared by the Wilcoxon matched-pairs signed rank test. The association between LAV% and forced expiratory volume in 1 s per forced vital capacity (FEV_1/FVC) was assessed by the Spearman rank correlation test.

Results (実験結果)

Mean values for LAV% determined for the U-HRCT and conventional HRCT modes were $8.9 \pm 8.8\%$ and $7.3 \pm 8.4\%$, respectively ($P < 0.0001$). The correlation coefficients for LAV% and FEV_1/FVC on the U-HRCT and conventional HRCT modes were 0.50 and 0.49, respectively (both $P < 0.01$). Compared with conventional HRCT scans, U-HRCT scans reveal emphysematous lesions in greater detail, and provide slightly increased correlation with airflow limitation.

Discussion (考察)

In this study, we found that i) U-HRCT scans depicted emphysematous lesions in greater detail than conventional HRCT scans and ii) U-HRCT scans provided stronger correlation with spirometric airflow limitation values (FEV_1/FVC) than conventional HRCT scans. Based on these results, we believe that U-HRCT scans are useful for detecting very small emphysematous lesions in smokers and COPD patients, which could lead to increasingly accurate measurements of emphysematous lesions in daily clinical care.

Compared with conventional HRCT scanners, the advantages of U-HRCT scanners used in daily clinical care were first reported for vascular imaging, with advantages such as clear visualization of very small intracranial arteries and coronary arteries, and in addition, the artery of Adamkiewicz.¹⁻⁵ The advantages of U-HRCT scanners for temporal bone imaging were also reported, with advantages such as increased detail of the normal structures of the middle ear.⁶ The improvement in visualization of small vessels/structures as provided by U-HRCT scanners over conventional HRCT scanners is based on an improved spatial resolution by a detector of a very small size. The size was reduced for the first time in almost 30 years (fixed at 0.5 mm or 0.625 mm for several decades) by 0.5-fold. In the field of chest imaging, the improved image quality by U-HRCT scanners has been mainly reported by investigators using cadaveric human lung phantoms.⁷⁻⁹ Although it has been unclear that U-HRCT is advantageous for the quantitative analysis of chest diseases, including COPD, our observations suggest that U-HRCT shows great potential for performing quantitative measurements of the lesions of pulmonary diseases, and at the very least, providing accurate measurements of subtle and early emphysematous lesions.

In this study, with the U-HRCT mode, we reconstructed scanning data from a matrix size of 1024, which is generally 512 for clinical CT scans. This is accounted for by the following: since the detector size of the U-HRCT scanner was 0.25×0.25 mm in the x-y plane, it was ideal that the voxel size of the CT scans was smaller than 0.25 mm. However, if the scan data obtained with a conventional FOV (320 mm) were reconstructed by the 512 matrix, the voxel size would have been 0.625 mm ($320/512$), which would have been much larger than the detector size of 0.25 mm. With the use of a matrix of 1024, the voxel size would be 0.313 mm, which would be close to 0.25 mm. Our observations show that the more detailed matrix setting enabled us to measure smaller lesions of pulmonary emphysema, which is consistent with a study of U-HRCT performed on a cadaveric human lung phantom with emphysema.⁸ In our study, the emphysema indices (LAV%) on the U-HRCT scans were higher than those obtained on the conventional HRCT scans, which clearly demonstrate that the U-HRCT scanner with a 1024-matrix setting is better than the conventional HRCT scanner with a 512-matrix setting for the detection of early/small emphysematous lesions.

It is also of interest that, in our study, resetting the threshold did not seem to be necessary for the U-HRCT scans that were obtained with a thinner slice thickness than those obtained for the conventional HRCT scans. In general, a thinner HRCT slice thickness results in decreased lung density and increased image noise, which often leads to increased values of the measurements of emphysematous lesions, and requires a decreased threshold setting.¹⁰ However, in this study, the value of the LAV% obtained on the U-HRCT scans (slice thickness of 0.25 mm) was 8.9% at the threshold setting of -950 HU and 5.7% at the setting of -960 HU. Considering that the value of LAV% obtained on conventional HRCT scans (slice thickness of 0.5 mm) at the threshold setting of -950 HU was 7.3%, changing the threshold from -950 HU to -960 HU for the U-HRCT scans can be considered an over-adjustment; and therefore, the threshold setting of -950 HU can be used continuously for the quantitative assessment of emphysematous lesions on U-HRCT scans.

Furthermore, the value of LAV% obtained on the U-HRCT scans set at -950 HU showed a stronger correlation with FEV₁/FVC than the values of LAV% obtained at -960 HU or -970 HU. We believe that -950 HU, which is the most common threshold for emphysema assessment, should also be used for U-HRCT scanners. That U-HRCT does not need a new, decreased threshold setting for emphysema measurement is most probably accounted for by the use of a powerful iterative reconstruction method, which is provided for the U-HRCT scanner. The iterative reconstruction method used in this study was AIDR3D-e, which was an updated version of AIDR3D. AIDR3D can minimize the effects of image noise, which is caused by low tube current, large body habitus, or adjacent bony structures, on the measurement of emphysematous lesions. Yamashiro et al have already reported that AIDR3D resulted in stabilized quantitative measurements of emphysematous lesions on HRCT scans obtained with very different tube current settings (240, 120, and 60 mA) and reduced the image noise associated with large body habitus.¹⁰ The newly developed iterative reconstruction method (AIDR3D-e), which was used for the U-HRCT scanner in this study, would provide a similar effect on noise reduction; which might account for the unnecessary resetting of the threshold for measurement of lesions on U-HRCT scans.

The present study revealed improved detection of emphysematous lesions by the U-HRCT mode, compared with the conventional HRCT mode. A mean 1.6% increase in LAV% (using -950 HU) might not seem to be a great improvement in the daily clinical care of patients with COPD. However, a correct diagnosis of the presence of emphysema, even if it is an LAV% of 1% or 2% only, would be especially significant for smokers. If pulmonary emphysema is diagnosed from U-HRCT findings (even as low as an LAV% of 1% or 2%) in a smoker without COPD, this might be a trigger for smoking cessation. When considering the possible misdiagnosis of “no signs of pulmonary emphysema” on a conventional HRCT scan, we believe that detection of slight emphysema might produce a clinical impact. Also, U-HRCT might be useful for following a patient with COPD or emphysema. The U-HRCT scanner will be more sensitive for detecting a slight progression in emphysema than the conventional HRCT scanner. Thus, although this study only found a very small difference between the values of LAV% provided by the U-HRCT versus conventional HRCT, we believe that the U-HRCT should provide some clinical advantages.

The mean CTDIvol (13.6 mGy) in this study was higher than the value (9.5 mGy) in our previous study, which used conventional HRCT scanners with a standard tube current setting (240 mA).¹⁰ The increased exposure might be accounted for by the 2 scanning FOV settings and different focus sizes. Particularly, with selection of a large FOV and large focus size, the AEC yielded a high tube current trend automatically, which resulted in a high CTDIvol and large DLP. With the aim of minimizing a patient's radiation exposure, our next focus of investigation will be on selecting the optimal scanning FOV and focus size.

This study has limitations. First, the number of study participants with COPD was low. Second, we only assessed spirometric values; thus, other functional parameters, such as plethysmographic measurements and diffusing capacity, were not evaluated. Third, since the conventional HRCT mode (512 × 512 matrix with 0.5-mm slice thickness) was reconstructed from the same raw data from the U-HRCT scanner, the HRCT mode could not be the same mode as that on actual conventional HRCT scans from conventional HRCT scanners. However, we believe that comparing 2 different modes obtained from data on a single scan was required in order to prevent unnecessary radiation exposure to patients by repeated scanning. Fourth, since AEC was adopted for the scan protocol, the tube current varied according to the patient's body habitus. This might have caused various levels of image noise among the patients; however, AEC is the current standard CT technique for the routine clinical care of patients with chest diseases, and the differences between noise levels must have been adjusted by the iterative reconstruction algorithm. Fifth, only whole-lung emphysema measurements were determined in this study. Considering the heterogeneous distribution of emphysematous lesions, LAV% should ideally be measured in 5 different lobes. However, since a limited number of workstations were available for analyzing the U-HRCT data, the workstations, including the workstation we used, could not segment the 5 lobes.

Compared with conventional HRCT scans, U-HRCT scans reveal emphysematous lesions in greater detail (mean difference, 1.6% ± 2.2%), and obtain slightly increased correlation with airflow limitation (correlation coefficients: 0.50 vs 0.49). U-HRCT should be

useful for detecting early emphysematous lesions in light smokers or nonsmokers without COPD; such results might be a powerful tool for enabling a patient to stop smoking in order to prevent progression to COPD.

Reference(参考文献)

1. Yoshioka K, Tanaka R, Takagi H, et al. Ultra-high-resolution CT angiography of the artery of Adamkiewicz: a feasibility study. *Neuroradiology*. 2018;60(1):109–115.
2. Takagi H, Tanaka R, Nagata K, et al. Diagnostic performance of coronary CT angiography with ultra-high-resolution CT: comparison with invasive coronary angiography. *Eur J Radiol*. 2018;101:30–37.
3. Tanaka R, Yoshioka K, Takagi H, Schuijf JD, Arakita K. Novel developments in non-invasive imaging of peripheral arterial disease with CT: experience with state-of-the-art, ultra-high-resolution CT and subtraction imaging. *Clin Radiol*. 2019;74(1):51–58.
4. Nagata H, Murayama K, Suzuki S, et al. Initial clinical experience of a prototype ultra-high-resolution CT for assessment of small intracranial arteries. *Jpn J Radiol*. 2019;37(4):283–291.
5. Meijer FJ, Schuijf JD, de Vries J, et al. Ultra-high-resolution subtraction CT angiography in the follow-up of treated intracranial aneurysms. *Insights Imaging*. 2019;10(1):2.
6. Yamashita K, Hiwatashi A, Togao O, et al. Ultrahigh-resolution CT scan of the temporal bone. *Eur Arch Otorhinolaryngol*. 2018;275(11):2797–2803.
7. Yanagawa M, Hata A, Honda O, et al. Subjective and objective comparisons of image quality between ultra-high-resolution CT and conventional area detector CT in phantoms and cadaveric human lungs. *Eur Radiol*. 2018;28(12):5060–5068.
8. Hata A, Yanagawa M, Honda O, et al. Effect of matrix size on the image quality of ultra-high-resolution CT of the lung: comparison of 512×512 , 1024×1024 , and 2048×2048 . *Acad Radiol*. 2018;25(7):869–876.
9. Honda O, Yanagawa M, Hata A, et al. Influence of gantry rotation time and scan mode on image quality in ultra-high-resolution CT system. *Eur J Radiol*. 2018;103(1):71–75.
10. Yamashiro T, Miyara T, Honda O, et al. Iterative reconstruction for quantitative computed tomography analysis of emphysema: consistent results using different tube currents. *Int J Chron Obstruct Pulmon Dis*. 2015;10(1):321–327.

注: 本研究は 2019 年 10 月 8 日「**International Journal of Chronic Obstructive Pulmonary Disease**」
という雑誌より発表しました。

2. 執筆論文 Publication of thesis ※記載した論文を添付してください。Attach all of the papers listed below.

論文名 1	Quantitative Emphysema Measurement On Ultra-High-Resolution CT Scans					
掲載誌名	International Journal of Chronic Obstructive Pulmonary Disease					
	2019 年 10 月	14 巻(号)	2283 頁 ~	2290 頁	言語	English
第1著者名	Yanyan Xu	第2著者名	Tsuneo Yamashiro	第3著者名	Hiroshi Moriya	
その他著者名	Shun Muramatsu, Sadayuki Murayama					
論文名 2	Characterizing MRI features of rectal cancers with different KRAS status					
掲載誌名	BMC Cancer					
	2019 年 11 月	19(1) 巻(号)	1111 頁 ~	頁	言語	English
第1著者名	Yanyan Xu	第2著者名	Qiaoyu Xu	第3著者名	Yanhui Ma	
その他著者名	Jianghui Duan, Haibo Zhang, Tongxi Liu, Lu Li, Hongliang Sun, Kaining Shi, Sheng Xie, Wu Wang					
論文名 3	Strain measurement on four-dimensional dynamic-ventilation CT: quantitative analysis of abnormal respiratory deformation of the lung in COPD					
掲載誌名	International Journal of Chronic Obstructive Pulmonary Disease					
	2018 年 12 月	14 巻(号)	65 頁 ~	72 頁	言語	English
第1著者名	Yanyan Xu	第2著者名	Tsuneo Yamashiro	第3著者名	Hiroshi Moriya	
その他著者名	Maho Tsubakimoto, Yukihiro Nagatani, Shin Matsuoka, Sadayuki Murayama, ACTive Study Group					
論文名 4	Correlation Between Intravoxel Incoherent Motion and Dynamic Contrast-Enhanced Magnetic Resonance Imaging Parameters in Rectal Cancer					
掲載誌名	Academic Radiology					
	2019 年 7 月	26(7) 巻(号)	e134 頁 ~	e140 頁	言語	English
第1著者名	Hongliang Sun	第2著者名	Yanyan Xu	第3著者名	Qiaoyu Xu	
その他著者名	Jianghui Duan, Haibo Zhang, Tongxi Liu, Lu Li, Queenie Chan, Sheng Xie, Wu Wang					
論文名 5	Relationship between CT activity score with lung function and the serum angiotensin converting enzyme in pulmonary sarcoidosis on chest HRCT					
掲載誌名	Medicine (Baltimore)					
	2018 年 9 月	97(36) 巻(号)	e12205 頁 ~	頁	言語	English
第1著者名	Jianghui Duan	第2著者名	Yanyan Xu	第3著者名	Haixu Zhu	
その他著者名	Haibo Zhang, Shilong Sun, Hongliang Sun, Wu Wang, Sheng Xie					
論文名 6	Could IVIM and ADC help in predicting the KRAS status in patients with rectal cancer?					
掲載誌名	European Radiology					
	2018 年 7 月	28(7) 巻(号)	3059 頁 ~	3065 頁	言語	English
第1著者名	Yanyan Xu	第2著者名	Qiaoyu Xu	第3著者名	Hongliang Sun	
その他著者名	Tongxi Liu, Kaining Shi, Wu Wang					
論文名 7	Quantitative intravoxel incoherent motion parameters derived from whole-tumor volume for assessing pathological complete response to neoadjuvant chemotherapy in locally advanced rectal cancer					
掲載誌名	Journal of Magnetic Resonance Imaging:JMRI					
	2018 年 7 月	48(1) 巻(号)	248 頁 ~	258 頁	言語	English
第1著者名	Qiaoyu Xu	第2著者名	Yanyan Xu	第3著者名	Hongliang Sun	
その他著者名	Queenie Chan, Kaining Shi, Aiping Song, Wu Wang					
論文名 8	Intravoxel Incoherent Motion MRI of Rectal Cancer: Correlation of Diffusion and Perfusion Characteristics With Prognostic Tumor Markers					
掲載誌名	American Journal of Roentgenology					
	2018 年 4 月	210(4) 巻(号)	W139 頁 ~	W147 頁	言語	English
第1著者名	Hongliang Sun	第2著者名	Yanyan Xu	第3著者名	Aiping Song	
その他著者名	Kaining Shi, Wu Wang					

3. 学会発表 Conference presentation ※筆頭演者として総会・国際学会を含む主な学会で発表したものを記載

※Describe your presentation as the principal presenter in major academic meetings including general meetings or

学会名 Conference	the 75th annual meeting of KCR		
演題 Topic	The effect of adaptive statistical iterative reconstruction (ASiR-V) levels on quantitative analysis of lung function using MDCT		
開催日 date	2019 年 9 月 18 日	開催地 Coex	Seoul, Korea
形式 method	<input checked="" type="checkbox"/> 口頭発表 Oral	<input type="checkbox"/> ポスター発表 Poster	言語 Language <input type="checkbox"/> 日本語 <input checked="" type="checkbox"/> 英語 <input type="checkbox"/> 中国語
共同演者名 Co-presenter	Yanhui Ma, Hongliang Sun, Wu wang, Sheng Xie		
学会名 Conference	第78回日本医学放射線学会総会		
演題 Topic	The effect of prospective ECG-gating for airway evaluation on ventilation volume computed tomography		
開催日 date	2019 年 4 月 11 日	開催地 パシフィコ	横浜 日本
形式 method	<input checked="" type="checkbox"/> 口頭発表 Oral	<input type="checkbox"/> ポスター発表 Poster	言語 Language <input type="checkbox"/> 日本語 <input checked="" type="checkbox"/> 英語 <input type="checkbox"/> 中国語
共同演者名 Co-presenter	Hongliang Sun, Yinghao Xu		
学会名 Conference	第11回呼吸機能イメージング研究会学術集会		
演題 Topic	慢性閉塞性肺疾患における肺運動の不均一性：呼吸ダイナミックCTにおけるストレイン値解析		
開催日 date	2019 年 1 月 25 日	開催地 venue	東京都千代田区 一橋講堂
形式 method	<input type="checkbox"/> 口頭発表 Oral	<input checked="" type="checkbox"/> ポスター発表 Poster	言語 Language <input checked="" type="checkbox"/> 日本語 <input type="checkbox"/> 英語 <input type="checkbox"/> 中国語
共同演者名 Co-presenter	山城 恒雄、森谷 浩史、椿本 真穂、村山 貞之		
学会名 Conference	the 26th annual meeting ISMRM-ESMRMB		
演題 Topic	Rectal Cancer: Comparison of MRI Characteristics and Texture Analysis Between Different Tumor KRAS Status		
開催日 date	2018 年 6 月 16 日	開催地 venue	Paris Expo Porte de Versailles, Paris, France
形式 method	<input type="checkbox"/> 口頭発表 Oral	<input checked="" type="checkbox"/> ポスター発表 Poster	言語 Language <input type="checkbox"/> 日本語 <input checked="" type="checkbox"/> 英語 <input type="checkbox"/> 中国語
共同演者名 Co-presenter	Hongliang Sun, Kaining Shi, Wu Wang		

4. 受賞（研究業績）Award (Research achievement)

名称 Award name	Educational Stipend		
国名 Country	France	受賞年 Year of	2018 年 6 月
名称 Award name	Travel Award		
国名 Country	Korea	受賞年 Year of	2019 年 9 月
名称 Award name	琉放賞		
国名 Country	Japan	受賞年 Year of	2019 年 11 月

5. 本研究テーマに関わる他の研究助成金受給 Other research grants concerned with your research

受給実績 Receipt record	<input type="checkbox"/> 有 <input checked="" type="checkbox"/> 無
助成機関名称 Funding agency	
助成金名称 Grant name	
受給期間 Supported period	年 月 ~ 年 月
受給額 Amount received	円
受給実績 Receipt record	<input type="checkbox"/> 有 <input type="checkbox"/> 無
助成機関名称 Funding agency	
助成金名称 Grant name	
受給期間 Supported period	年 月 ~ 年 月
受給額 Amount received	円

6. 他の奨学金受給 Another awarded scholarship

受給実績 Receipt record	<input type="checkbox"/> 有 <input checked="" type="checkbox"/> 無
助成機関名称 Funding agency	
奨学金名称 Scholarship name	
受給期間 Supported period	年 月 ~ 年 月
受給額 Amount received	円

7. 研究活動に関する報道発表 Press release concerned with your research activities

※記載した記事を添付してください。 Attach a copy of the article described below

報道発表 Press release	<input checked="" type="checkbox"/> 有 <input type="checkbox"/> 無	発表年月日 Date of release	2018/10/1
発表機関 Released medium	好医生国际教育		
発表形式 Release method	・新聞 ・雑誌 ・Web site ・記者発表 ・その他 ()		
発表タイトル Released title	协和医生访学日本，同样拼命工作的日本医生，待遇和我们有何不同? https://mp.weixin.qq.com/s/OD6AFDgK2r_0ehrDUxZAag		

8. 本研究テーマに関する特許出願予定 Patent application concerned with your research theme

出願予定 Scheduled	<input type="checkbox"/> 有 <input checked="" type="checkbox"/> 無	出願国 Application	
出願内容(概要) Application contents			

9. その他 Others

特にありません。

指導責任者(署名)

山城 恒雄
村上 夏之



Quantitative Emphysema Measurement On Ultra-High-Resolution CT Scans

This article was published in the following Dove Press journal:
International Journal of Chronic Obstructive Pulmonary Disease

Yanyan Xu ^{1,2}

Tsuneo Yamashiro ^{1,3}

Hiroshi Moriya³

Shun Muramatsu³

Sadayuki Murayama¹

¹Department of Radiology, Graduate School of Medical Science, University of the Ryukyus, Okinawa, Japan;

²Department of Radiology, China-Japan Friendship Hospital, Beijing, People's Republic of China; ³Department of Radiology, Ohara General Hospital, Fukushima, Japan

Purpose: To evaluate the advantages of ultra-high-resolution computed tomography (U-HRCT) scans for the quantitative measurement of emphysematous lesions over conventional HRCT scans.

Materials and methods: This study included 32 smokers under routine clinical care who underwent chest CT performed by a U-HRCT scanner. Chronic obstructive pulmonary disease (COPD) was diagnosed in 13 of the 32 participants. Scan data were reconstructed by 2 different protocols: i) U-HRCT mode with a 1024×1024 matrix and 0.25-mm slice thickness and ii) conventional HRCT mode with a 512×512 matrix and 0.5-mm slice thickness. On both types of scans, lesions of emphysema were quantitatively assessed as percentage of low attenuation volume (LAV%, <-950 Hounsfield units). LAV% values determined for scan data from the U-HRCT and conventional HRCT modes were compared by the Wilcoxon matched-pairs signed rank test. The association between LAV% and forced expiratory volume in 1 s per forced vital capacity (FEV₁/FVC) was assessed by the Spearman rank correlation test.

Results: Mean values for LAV% determined for the U-HRCT and conventional HRCT modes were 8.9 ± 8.8% and 7.3 ± 8.4%, respectively ($P < 0.0001$). The correlation coefficients for LAV% and FEV₁/FVC on the U-HRCT and conventional HRCT modes were 0.50 and 0.49, respectively (both $P < 0.01$).

Conclusion: Compared with conventional HRCT scans, U-HRCT scans reveal emphysematous lesions in greater detail, and provide slightly increased correlation with airflow limitation.

Keywords: chronic obstructive pulmonary disease, computed tomography, emphysema, ultra-high-resolution CT, quantitative measurement

Introduction

Quantitative emphysema findings on CT have been frequently used by physicians as estimations for the extent of emphysema in patients with chronic obstructive pulmonary disease (COPD). The measurement is thought to be a reproducible approach for confirming the severity of emphysema, and also correlates well with spirometry values.¹⁻¹¹ The percentage of low attenuation areas/volumes for the total lung areas/volumes on thin-section CT scans are widely known to be significantly correlated with the results of various pulmonary function tests, including spirometry and diffusing capacity of the lungs for carbon monoxide.⁴⁻⁶

Although current quantitative emphysema measurements can be automatically performed by commercially available workstations and open-access software, the measurements are affected by several scanning/reconstruction parameters and other factors,

Correspondence: Tsuneo Yamashiro
Department of Radiology, Graduate School of Medical Science, University of the Ryukyus, 207 Uehara, Nishihara, Okinawa 903-0215, Japan
Tel +81-98-895-1162
Fax +81-98-895-1420
Email clatsune@yahoo.co.jp

including section thickness, reconstruction kernels, radiation dose settings, iterative reconstruction techniques, and brand of scanner.^{4-9,12,13} It has been reported that the extent of emphysema tends to increase with thinner sections and sharper reconstruction kernels.⁹ Furthermore, compared with conventional filtered-back-projection (FBP) methods, an iterative reconstruction (IR) algorithm can stabilize emphysema measurements with low-dose settings, and reduce radiation exposure without compromising image quality.¹³ Therefore, caution should be exercised with regard to quantitative emphysema measurements, particularly when they involve innovations in CT hardware and software.

Ultra-high-resolution CT (U-HRCT) scanners with ultra-small detector elements (0.25 × 0.25 mm) have recently been introduced into clinical practice.¹⁴⁻²² The size of the detector element in the U-HRCT scanner is 50% smaller than those in conventional HRCT scanners in all 3 directions (x, y, and z axes). Use of the ultra-small detector along with an ultra-small focal spot provided by the X-ray tube obtains the highest spatial resolution in CT images, as evidenced by improved visualization of small lung lesions and small vessels in the brain and body.¹⁴⁻²² Honda et al have reported that U-HRCT clearly depicts small emphysematous lesions in human cadaveric lungs, which were unclear on conventional HRCT scans.¹⁷ However, to our best knowledge, no published data are available on the advantages of the U-HRCT scanner for visualization of pulmonary emphysema in the human body, with regard to statistical differences between quantitative measurements of emphysematous lesions on U-HRCT scans versus conventional HRCT scans. We hypothesized that U-HRCT scans, which show greater spatial resolution than conventional HRCT scans, would enable improved visualization of pulmonary emphysema over conventional HRCT scans. The evidence for this would be a stronger correlation with spirometric values than seen for conventional HRCT. Thus, the purpose of this study was i) to evaluate the advantages of U-HRCT for the quantitative measurement of pulmonary emphysematous lesions and ii) to investigate whether or not the measurement of emphysematous lesions on U-HRCT scans showed a stronger correlation with spirometric values, compared with conventional HRCT.

Materials And Methods

This retrospective study was approved by the Institutional Review Board of the University of the Ryukyus. Written informed consent from enrolled participants was waived, and the delivery of data to the University of the Ryukyus was approved by the Institutional Review Board of Ohara

General Hospital. The patient data, including CT scans and clinical information, were fully anonymized at Ohara General Hospital.

Patients

Thirty-two smokers (13 COPD patients and 19 non-COPD smokers; 3 females and 29 males; mean age 71 ± 10 years) were consecutively enrolled in the study (Table 1). All study participants underwent spirometry and chest U-HRCT at Ohara General Hospital. Of all 32 participants, 11 underwent CT for known lung diseases (preoperative lung cancer, n = 3; pneumonia, n = 3; COPD, n = 5), 14 for regular follow-up (post-treatment of lung cancer, n = 4; COPD, n = 6, lung nodule, n = 3; non-COPD emphysema, n = 1), 7 for screening (abnormal shadows on chest X-ray, n = 3, indeterminate nodule, n = 2; shortness of breath, n = 1; chest pain, n = 1). Patients with obvious interstitial pneumonia or other obstructive diseases (e.g. bronchial asthma, chronic bronchitis) were excluded from this study.

CT Protocols

All CT scans were performed by a U-HRCT scanner (Aquilion Precision; Canon Medical Systems, Otawara, Tochigi, Japan). This scanner is characterized by 0.25-mm collimation (160 detector rows) in the z axis, and 1792 channels (0.25-mm detectors in the x–y plane). All participants were scanned by the U-HRCT scanner with the following settings: tube voltage = 120 kVp; tube current = automatic exposure control (AEC); collimation = 0.25 mm (super-high resolution mode); rotation time = 0.5 s, beam pitch = 0.806; field of view (FOV) = 300–350 mm (medium FOV, n= 17; large FOV, n= 15); reconstruction kernel = FC14 (for mediastinum); iterative reconstruction = adaptive iterative dose reduction using a three-dimensional processing-enhanced (AIDR3D-e) “standard” setting.

The original scan data were converted to 2 different modes (image series): i) U-HRCT mode: 1024 × 1024

Table 1 Clinical Characteristics Of The 32 Study Participants

	Mean ± SD	Range
Gender (female:male)	(3:29)	–
Age (years)	71 ± 10	(49 to 88)
Brinkman index	933 ± 505	(300 to 2480)
FVC (L)	3.1 ± 0.8	(1.8 to 4.6)
FEV ₁ (L)	2.1 ± 0.7	(0.7 to 3.6)
FEV ₁ (%predicted)	0.78 ± 0.20	(0.30 to 1.13)
FEV ₁ /FVC	0.68 ± 0.13	(0.29 to 0.88)

Abbreviations: FVC, forced vital capacity; FEV₁, forced expiratory volume in 1 s; SD, standard deviation.

matrix and a slice thickness of 0.25 mm and ii) conventional HRCT mode: 512 × 512 matrix and a slice thickness of 0.5 mm. The conventional HRCT mode imitates CT scans created by common HRCT scanners, with 0.5-mm collimation.

Radiation exposure was assessed by the volume CT dose index (CTDIvol) and the dose-length product (DLP), which were provided by the scanner in a dose information report for each patient.

Quantitative Analysis Of Lung Densitometry And Emphysematous Lesions

Both U-HRCT and conventional HRCT scans (modes) were analyzed by commercially available software (Lung Volume Measurement; Canon Medical Systems).²³ The lung volume (LV) of the entire lung and the percentage low attenuation volume (LAV%) on 3 different threshold settings (−950, −960, and −970 Hounsfield units [HUs]) were measured automatically.

Spirometry

All subjects underwent spirometry testing, including forced expiratory volume in 1 s (FEV₁) and forced vital capacity (FVC), according to American Thoracic Society standards.²⁴ The spirometric values of the study participants are shown in Table 1. Based on the criteria by the American Thoracic Society, COPD was diagnosed in 13 participants. The other 19 smokers did not satisfy the criteria for COPD (non-COPD smokers).

Statistical Analysis

Statistical analysis was performed by JMP 12.0 software (SAS Institute, Cary, NC, USA). Continuous variables were expressed as means ± standard deviation (SD). The Wilcoxon matched-pair signed rank test was used to compare CT indices, including values for LAV% obtained on U-HRCT scans and conventional HRCT scans. The association between values for LAV% and FEV₁/FVC was assessed by the Spearman rank correlation test. A *P*-value of <0.05 was considered significant.

Results

Radiation Dose Assessments

In this study, the mean CTDIvol value was 13.6 ± 6.4 mGy and mean DLP value was 549.3 ± 247.1 mGy·cm.

Quantitative Measurements Of LAV% Values Under Different Thresholds

The mean LV values were 5.25 ± 0.96 L on U-HRCT scans and 5.26 ± 0.96 L on conventional HRCT scans. Although the difference between the LV values was very small, it was found to be significant (*P*<0.001). Although the LV was minimally larger on conventional HRCT scans than on U-HRCT scans, the value for LAV% was larger on U-HRCT scans than on conventional HRCT scans under all 3 different threshold settings (Table 2, Figures 1–4). For example, at the threshold of −950 HU, the mean value for LAV% was 8.9 ± 8.8% on U-HRCT and 7.3 ± 8.4% on conventional HRCT (*P*<0.0001).

Correlations Between Quantitative Measurements Of Emphysematous Lesions And Spirometric Values

All values for LAV% measured on U-HRCT and conventional HRCT scans at different thresholds were significantly correlated with FEV₁/FVC (*P*<0.01–0.05; Table 3, Figure 5). In general, correlation coefficients were slightly decreased with reduction in the density thresholds from −950 to −970 HU. At all 3 different thresholds, the correlations with FEV₁/FVC for the values obtained for LAV%, as measured on U-HRCT scans, were stronger than the correlations for the values obtained for LAV% as measured on conventional HRCT scans (Table 3). The highest correlation coefficient in this study was provided by the U-HRCT scans at the threshold of −950 HU ($\rho = 0.50$, *P*<0.01).

Discussion

In this study, we found that i) U-HRCT scans depicted emphysematous lesions in greater detail than conventional

Table 2 Measurements Of Emphysematous Lesions Obtained On U-HRCT Scans Versus Conventional HRCT Scans At Different Density Thresholds

CT Indices	Image Mode		P-Value
	U-HRCT	Conventional HRCT	
LV (L)	5.25 ± 0.96	5.26 ± 0.96	<0.001
LAV% ₋₉₅₀ (%)	8.9 ± 8.8	7.3 ± 8.4	<0.0001
LAV% ₋₉₆₀ (%)	5.7 ± 6.5	4.6 ± 6.0	<0.0001
LAV% ₋₉₇₀ (%)	3.6 ± 4.6	2.9 ± 4.1	<0.0001

Abbreviations: LV, lung volume; LAV%₋₉₅₀/LAV%₋₉₆₀/LAV%₋₉₇₀, percentage low attenuation volume at thresholds of −950, −960, and −970 Hounsfield units; U-HRCT, ultra-high-resolution computed tomography.

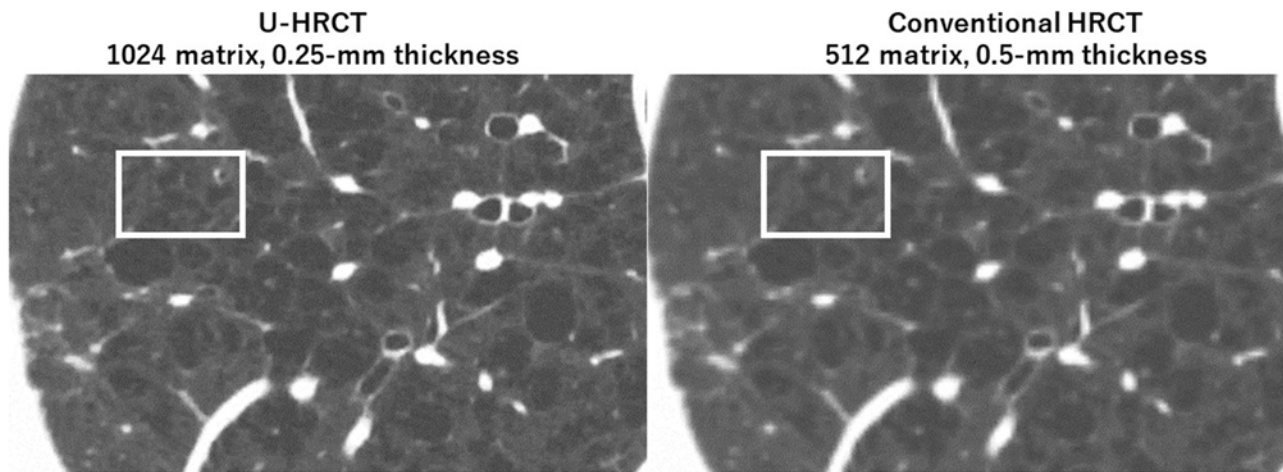


Figure 1 Visualization of lesions of pulmonary emphysema on ultra-high-resolution CT (U-HRCT) and conventional HRCT images. On an U-HRCT image (left), the margins of pulmonary emphysema are more clearly depicted than on a conventional HRCT image (right), particularly the relatively small emphysematous lesions (rectangles).

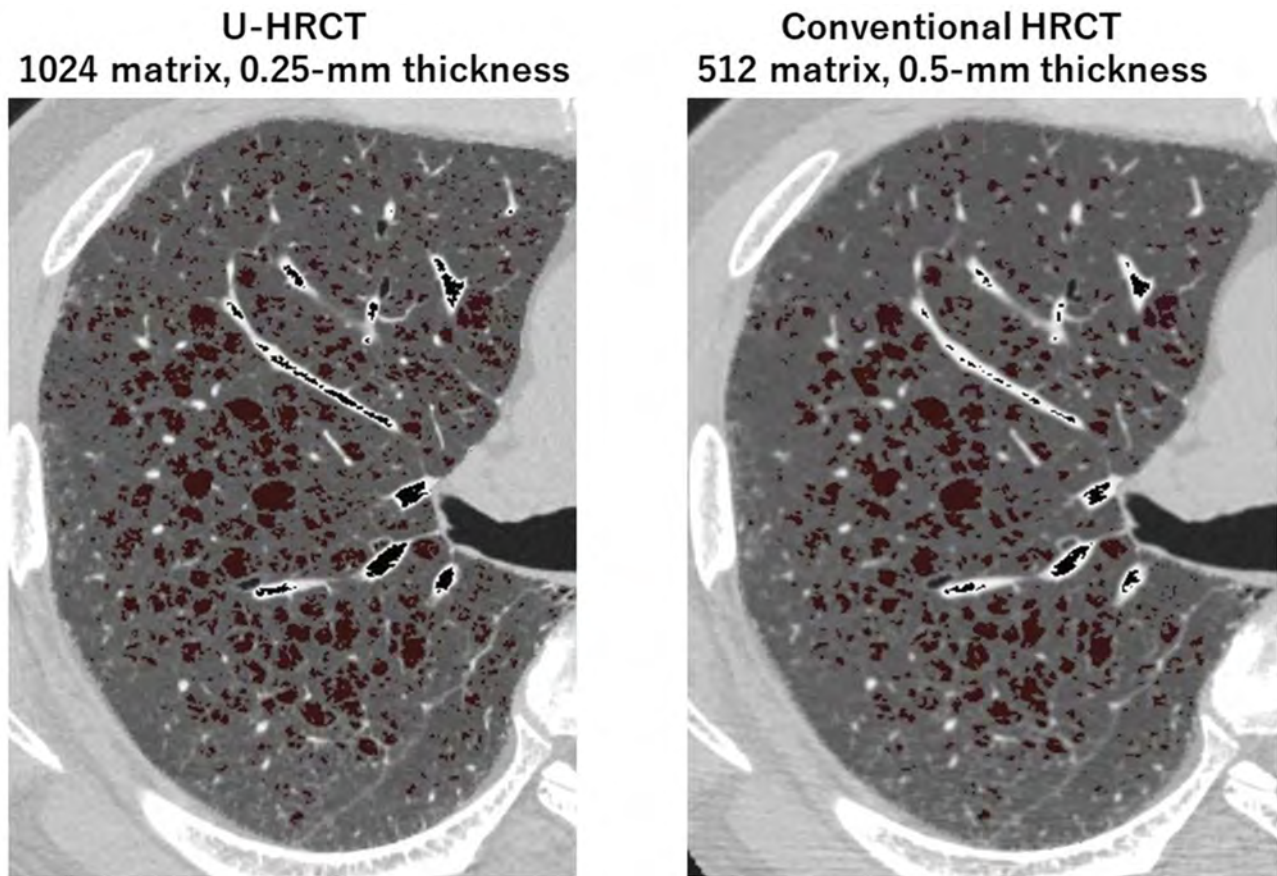


Figure 2 Ultra-high-resolution CT (U-HRCT) image compared with a conventional HRCT image for the detection of emphysema. At the threshold setting of <-950 Hounsfield units, emphysematous lesions are identified as dark-red areas on axial images. Some of the very small emphysematous lesions, which is clearly identified on the U-HRCT image (left), cannot be seen on the identical conventional HRCT image (right).

HRCT scans and ii) U-HRCT scans provided stronger correlation with spirometric airflow limitation values (FEV_1/FVC) than conventional HRCT scans. Based on these results, we believe that U-HRCT scans are useful

for detecting very small emphysematous lesions in smokers and COPD patients, which could lead to increasingly accurate measurements of emphysematous lesions in daily clinical care.

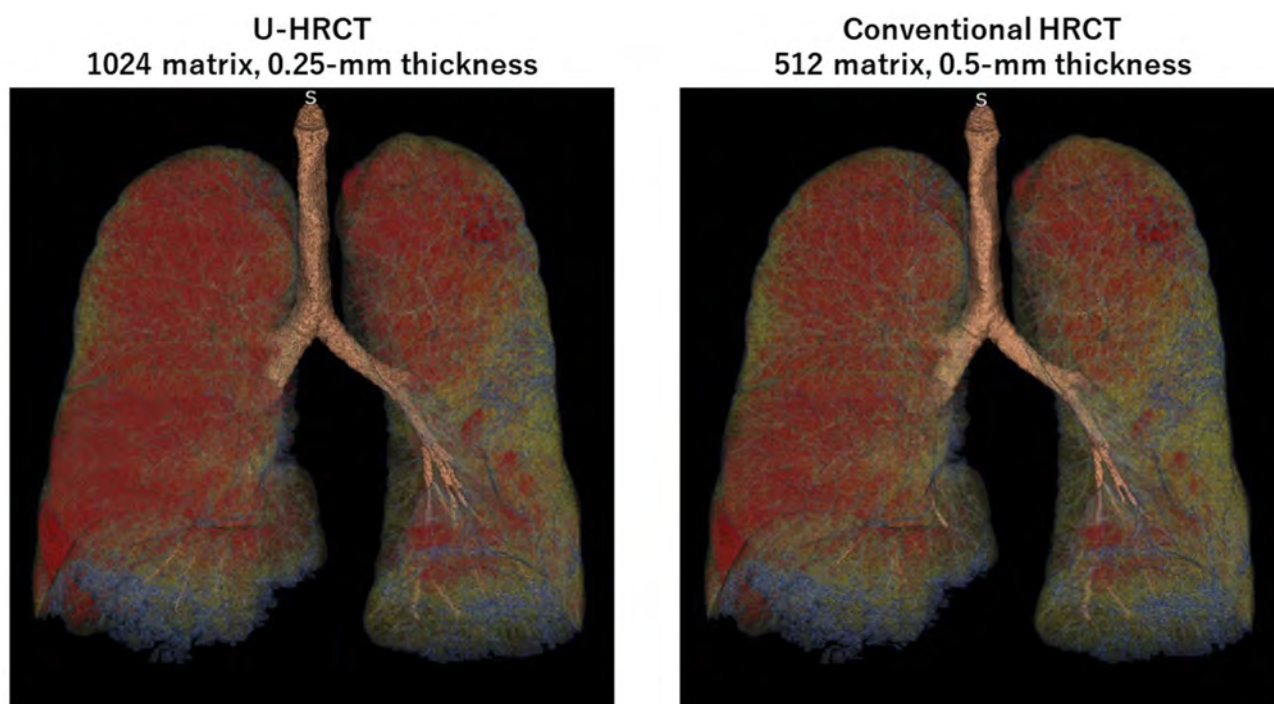


Figure 3 Quantitative measurements of lesions of pulmonary emphysema on ultra-high-resolution CT (U-HRCT) and conventional HRCT scans. Red areas are emphysematous lesions identified by the software (<-950 Hounsfield units). In this COPD patient, the percentage low attenuation volume (LAV%) was 32.8% on the U-HRCT scan (left) and 30.7% on the conventional HRCT scan (right).

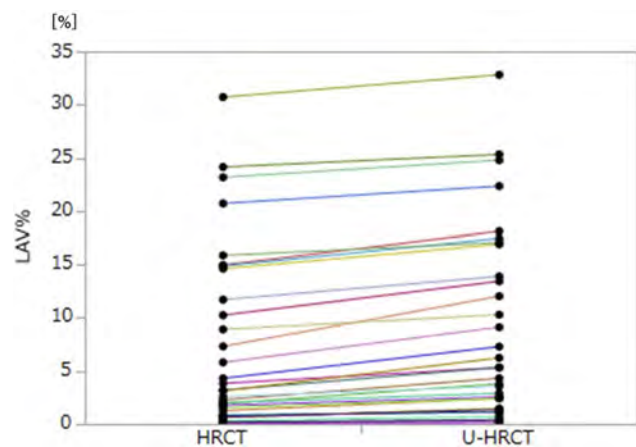


Figure 4 Comparison of the percentage of low attenuation volume (LAV%) on ultra-high-resolution CT (U-HRCT) and conventional HRCT scan modes using the threshold of -950 Hounsfield units. LAV% on HRCT scans tends to increase on U-HRCT scans.

Compared with conventional HRCT scanners, the advantages of U-HRCT scanners used in daily clinical care were first reported for vascular imaging, with advantages such as clear visualization of very small intracranial arteries and coronary arteries, and in addition, the artery of Adamkiewicz.^{18–22} The advantages of U-HRCT scanners for temporal bone imaging were also reported, with advantages such as increased detail of the normal structures of the

middle ear.²⁵ The improvement in visualization of small vessels/structures as provided by U-HRCT scanners over conventional HRCT scanners is based on an improved spatial resolution by a detector of a very small size. The size was reduced for the first time in almost 30 years (fixed at 0.5 mm or 0.625 mm for several decades) by 0.5-fold. In the field of chest imaging, the improved image quality by U-HRCT scanners has been mainly reported by investigators using cadaveric human lung phantoms.^{15–17} Although it has been unclear that U-HRCT is advantageous for the quantitative analysis of chest diseases, including COPD, our observations suggest that U-HRCT shows great potential for performing quantitative measurements of the lesions of pulmonary diseases, and at the very least, providing accurate measurements of subtle and early emphysematous lesions.

In this study, with the U-HRCT mode, we reconstructed scanning data from a matrix size of 1024, which is generally 512 for clinical CT scans. This is accounted for by the following: since the detector size of the U-HRCT scanner was 0.25×0.25 mm in the x–y plane, it was ideal that the voxel size of the CT scans was smaller than 0.25 mm. However, if the scan data obtained with a conventional FOV (320 mm) were reconstructed by the 512 matrix, the voxel size would have been 0.625 mm ($320/512$), which

Table 3 Correlations Between Values For LAV% And Airflow Limitation

Image Mode	LAV% At Different Thresholds	Correlation With FEV ₁ /FVC	
		Coefficient (ρ)	P-Value
U-HRCT	LAV% ₋₉₅₀	-0.50	<0.01
	LAV% ₋₉₆₀	-0.47	<0.01
	LAV% ₋₉₇₀	-0.40	<0.05
Conventional HRCT	LAV% ₋₉₅₀	-0.49	<0.01
	LAV% ₋₉₆₀	-0.43	<0.05
	LAV% ₋₉₇₀	-0.35	<0.05

Abbreviations: LAV%₋₉₅₀/LAV%₋₉₆₀/LAV%₋₉₇₀, percentage low attenuation volume at thresholds of -950, -960, and -970 Hounsfield units; U-HRCT, ultra-high-resolution computed tomography; FEV₁, forced expiratory volume in 1 s; FVC, forced vital capacity.

would have been much larger than the detector size of 0.25 mm. With the use of a matrix of 1024, the voxel size would be 0.313 mm, which would be close to 0.25 mm. Our observations show that the more detailed matrix setting enabled us to measure smaller lesions of pulmonary emphysema, which is consistent with a study of U-HRCT performed on a cadaveric human lung phantom with emphysema.¹⁶ In our study, the emphysema indices (LAV%) on the U-HRCT scans were higher than those obtained on the conventional HRCT scans, which clearly demonstrate that the U-HRCT scanner with a 1024-matrix setting is better than the conventional HRCT scanner with a 512-matrix setting for the detection of early/small emphysematous lesions.

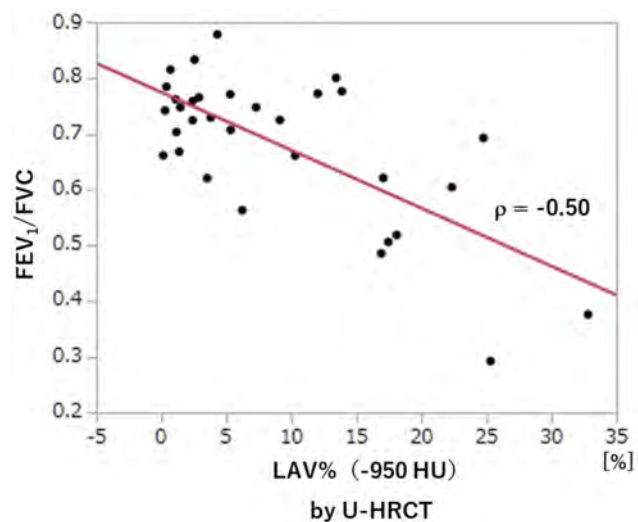


Figure 5 Correlation between FEV₁/FVC and LAV%₋₉₅₀ (U-HRCT). A significant, negative correlation is observed between LAV%₋₉₅₀ and FEV₁/FVC.

Abbreviations: FEV₁, forced expiratory volume in 1 s; FVC, forced vital capacity; LAV%₋₉₅₀, percentage low attenuation volume at a threshold of -950 Hounsfield units; U-HRCT, ultra-high-resolution computed tomography.

It is also of interest that, in our study, resetting the threshold did not seem to be necessary for the U-HRCT scans that were obtained with a thinner slice thickness than those obtained for the conventional HRCT scans. In general, a thinner HRCT slice thickness results in decreased lung density and increased image noise, which often leads to increased values of the measurements of emphysematous lesions, and requires a decreased threshold setting.²⁶ However, in this study, the value of the LAV% obtained on the U-HRCT scans (slice thickness of 0.25 mm) was 8.9% at the threshold setting of -950 HU and 5.7% at the setting of -960 HU. Considering that the value of LAV% obtained on conventional HRCT scans (slice thickness of 0.5 mm) at the threshold setting of -950 HU was 7.3%, changing the threshold from -950 HU to -960 HU for the U-HRCT scans can be considered an over-adjustment; and therefore, the threshold setting of -950 HU can be used continuously for the quantitative assessment of emphysematous lesions on U-HRCT scans. Furthermore, the value of LAV% obtained on the U-HRCT scans set at -950 HU showed a stronger correlation with FEV₁/FVC than the values of LAV% obtained at -960 HU or -970 HU. We believe that -950 HU, which is the most common threshold for emphysema assessment, should also be used for U-HRCT scanners. That U-HRCT does not need a new, decreased threshold setting for emphysema measurement is most probably accounted for by the use of a powerful iterative reconstruction method, which is provided for the U-HRCT scanner. The iterative reconstruction method used in this study was AIDR3D-e, which was an updated version of AIDR3D. AIDR3D can minimize the effects of image noise, which is caused by low tube current, large body habitus, or adjacent bony structures, on the measurement of emphysematous lesions. Yamashiro et al have already reported that AIDR3D resulted in stabilized quantitative measurements of emphysematous lesions on HRCT scans obtained with very different tube current settings (240, 120, and 60 mA) and reduced the image noise associated with large body habitus.²⁶ The newly developed iterative reconstruction method (AIDR3D-e), which was used for the U-HRCT scanner in this study, would provide a similar effect on noise reduction; which might account for the unnecessary resetting of the threshold for measurement of lesions on U-HRCT scans.

The present study revealed improved detection of emphysematous lesions by the U-HRCT mode, compared with the conventional HRCT mode. A mean 1.6% increase in LAV% (using -950 HU) might not seem to be a great

improvement in the daily clinical care of patients with COPD. However, a correct diagnosis of the presence of emphysema, even if it is an LAV% of 1% or 2% only, would be especially significant for smokers. If pulmonary emphysema is diagnosed from U-HRCT findings (even as low as an LAV% of 1% or 2%) in a smoker without COPD, this might be a trigger for smoking cessation. When considering the possible misdiagnosis of “no signs of pulmonary emphysema” on a conventional HRCT scan, we believe that detection of slight emphysema might produce a clinical impact. Also, U-HRCT might be useful for following a patient with COPD or emphysema. The U-HRCT scanner will be more sensitive for detecting a slight progression in emphysema than the conventional HRCT scanner. Thus, although this study only found a very small difference between the values of LAV% provided by the U-HRCT versus conventional HRCT, we believe that the U-HRCT should provide some clinical advantages.

The mean CTDIvol (13.6 mGy) in this study was higher than the value (9.5 mGy) in our previous study, which used conventional HRCT scanners with a standard tube current setting (240 mA).²⁶ The increased exposure might be accounted for by the 2 scanning FOV settings and different focus sizes. Particularly, with selection of a large FOV and large focus size, the AEC yielded a high tube current trend automatically, which resulted in a high CTDIvol and large DLP. With the aim of minimizing a patient’s radiation exposure, our next focus of investigation will be on selecting the optimal scanning FOV and focus size.

This study has limitations. First, the number of study participants with COPD was low. Second, we only assessed spirometric values; thus, other functional parameters, such as plethysmographic measurements and diffusing capacity, were not evaluated. Third, since the conventional HRCT mode (512 × 512 matrix with 0.5-mm slice thickness) was reconstructed from the same raw data from the U-HRCT scanner, the HRCT mode could not be the same mode as that on actual conventional HRCT scans from conventional HRCT scanners. However, we believe that comparing 2 different modes obtained from data on a single scan was required in order to prevent unnecessary radiation exposure to patients by repeated scanning. Fourth, since AEC was adopted for the scan protocol, the tube current varied according to the patient’s body habitus. This might have caused various levels of image noise among the patients; however, AEC is the current standard CT technique for the routine clinical

care of patients with chest diseases, and the differences between noise levels must have been adjusted by the iterative reconstruction algorithm. Fifth, only whole-lung emphysema measurements were determined in this study. Considering the heterogeneous distribution of emphysematous lesions, LAV% should ideally be measured in 5 different lobes. However, since a limited number of workstations were available for analyzing the U-HRCT data, the workstations, including the workstation we used, could not segment the 5 lobes.

Conclusion

Compared with conventional HRCT scans, U-HRCT scans reveal emphysematous lesions in greater detail (mean difference, 1.6% ± 2.2%), and obtain slightly increased correlation with airflow limitation (correlation coefficients: 0.50 vs 0.49). U-HRCT should be useful for detecting early emphysematous lesions in light smokers or nonsmokers without COPD; such results might be a powerful tool for enabling a patient to stop smoking in order to prevent progression to COPD.

Acknowledgments

The authors thank Mr Kenji Fujii (Canon Medical Systems) for his technical support.

Disclosure

The University of the Ryukyus and Ohara General Hospital receive a research grant from Canon Medical Systems. Ynayan Xu receives a scholarship (Sasagawa scholarship) from the Japan-China Medical Association. Tsuneo Yamashiro reports a grant from Canon Medical Systems during the conduct of the study, and grants from Ziosoft and JSR outside the submitted work. Sadayuki Murayama reports a research grant from Canon Medical Systems during the conduct of the study. The authors report no other conflicts of interest for this work.

References

1. Nakano Y, Muro S, Sakai H, et al. Computed tomographic measurements of airway dimensions and emphysema in smokers. Correlation with lung function. *Am J Respir Crit Care Med.* 2000;162(3):1102–1108.
2. Mishima M, Hirai T, Itoh H, et al. Complexity of terminal airspace geometry assessed by lung computed tomography in normal subjects and patients with chronic obstructive pulmonary disease. *Proc Natl Acad Sci U S A.* 1999;96(16):8829–8834.
3. Mets OM, de Jong PA, van Ginneken B, Gietema HA, Lammers JW. Quantitative computed tomography in COPD: possibilities and limitations. *Lung.* 2012;190(2):133–145.

4. Boedeker KL, McNitt-Gray MF, Rogers SR, et al. Emphysema: effect of reconstruction algorithm on CT imaging measures. *Radiology*. 2004;232(1):295–301.
5. Madani A, De Maertelaer V, Zanen J, Gevenois PA. Pulmonary emphysema: radiation dose and section thickness at multidetector CT quantification – comparison with macroscopic and microscopic morphometry. *Radiology*. 2007;243(1):250–257.
6. Doganay O, Matin T, Chen M, et al. Time-series hyperpolarized xenon-129 MRI of lobar lung ventilation of COPD in comparison to V/Q-SPECT/CT and CT. *Eur Radiol*. 2019;29(8):4058–4067. doi:10.1007/s00330-018-5888-y
7. Wang Z, Gu S, Leader JK, et al. Optimal threshold in CT quantification of emphysema. *Eur Radiol*. 2013;23(4):975–984.
8. Yuan R, Mayo JR, Hogg JC, et al. The effects of radiation dose and CT manufacturer on measurements of lung densitometry. *Chest*. 2007;132(2):617–623.
9. Gierada DS, Bierhals AJ, Choong CK, et al. Effects of CT section thickness and reconstruction kernel on emphysema quantification relationship to the magnitude of the CT emphysema index. *Acad Radiol*. 2010;17(2):146–156.
10. Yamashiro T, Matsuoka S, Bartholmai BJ, et al. Collapsibility of lung volume by paired inspiratory and expiratory CT scans: correlations with lung function and mean lung density. *Acad Radiol*. 2010;17(4):489–495.
11. Yamashiro T, Moriya H, Tsubakimoto M, Matsuoka S, Murayama S. Continuous quantitative measurement of the proximal airway dimensions and lung density on four-dimensional dynamic-ventilation CT in smokers. *Int J Chron Obstruct Pulmon Dis*. 2016;11(1):755–764.
12. Yamashiro T, Miyara T, Honda O, et al. Adaptive Iterative Dose Reduction using Three Dimensional Processing (AIDR3D) improves chest CT image quality and reduces radiation exposure. *PLoS ONE*. 2014;9(8):e105735.
13. Choo JY, Goo JM, Lee CH, Park CM, Park SJ, Shim MS. Quantitative analysis of emphysema and airway measurements according to iterative reconstruction algorithms: comparison of filtered back projection, adaptive statistical iterative reconstruction and model-based iterative reconstruction. *Eur Radiol*. 2014;24(4):799–806.
14. Kakinuma R, Moriyama N, Muramatsu Y, et al. Ultra-high-resolution computed tomography of the lung: image quality of a prototype scanner. *PLoS One*. 2015;10(9):e0137165.
15. Yanagawa M, Hata A, Honda O, et al. Subjective and objective comparisons of image quality between ultra-high-resolution CT and conventional area detector CT in phantoms and cadaveric human lungs. *Eur Radiol*. 2018;28(12):5060–5068.
16. Hata A, Yanagawa M, Honda O, et al. Effect of matrix size on the image quality of ultra-high-resolution CT of the lung: comparison of 512 × 512, 1024 × 1024, and 2048 × 2048. *Acad Radiol*. 2018;25(7):869–876.
17. Honda O, Yanagawa M, Hata A, et al. Influence of gantry rotation time and scan mode on image quality in ultra-high-resolution CT system. *Eur J Radiol*. 2018;103(1):71–75.
18. Yoshioka K, Tanaka R, Takagi H, et al. Ultra-high-resolution CT angiography of the artery of Adamkiewicz: a feasibility study. *Neuroradiology*. 2018;60(1):109–115.
19. Takagi H, Tanaka R, Nagata K, et al. Diagnostic performance of coronary CT angiography with ultra-high-resolution CT: comparison with invasive coronary angiography. *Eur J Radiol*. 2018;101:30–37.
20. Tanaka R, Yoshioka K, Takagi H, Schuijf JD, Arakita K. Novel developments in non-invasive imaging of peripheral arterial disease with CT: experience with state-of-the-art, ultra-high-resolution CT and subtraction imaging. *Clin Radiol*. 2019;74(1):51–58.
21. Nagata H, Murayama K, Suzuki S, et al. Initial clinical experience of a prototype ultra-high-resolution CT for assessment of small intracranial arteries. *Jpn J Radiol*. 2019;37(4):283–291.
22. Meijer FJ, Schuijf JD, de Vries J, et al. Ultra-high-resolution subtraction CT angiography in the follow-up of treated intracranial aneurysms. *Insights Imaging*. 2019;10(1):2.
23. Yamashiro T, Moriya H, Matsuoka S, et al. Asynchrony in respiratory movements between the pulmonary lobes in patients with chronic obstructive pulmonary disease: continuous measurement of lung density by 4-dimensional dynamic-ventilation CT. *Int J Chron Obstruct Pulmon Dis*. 2017;12(1):2101–2109.
24. Vestbo J, Hurd SS, Agusti AG, et al. Global strategy for the diagnosis, management, and prevention of chronic obstructive pulmonary disease: GOLD executive summary. *Am J Respir Crit Care Med*. 2013;187(4):347–365.
25. Yamashita K, Hiwatashi A, Togao O, et al. Ultrahigh-resolution CT scan of the temporal bone. *Eur Arch Otorhinolaryngol*. 2018;275(11):2797–2803.
26. Yamashiro T, Miyara T, Honda O, et al. Iterative reconstruction for quantitative computed tomography analysis of emphysema: consistent results using different tube currents. *Int J Chron Obstruct Pulmon Dis*. 2015;10(1):321–327.

International Journal of Chronic Obstructive Pulmonary Disease

Dovepress

Publish your work in this journal

The International Journal of COPD is an international, peer-reviewed journal of therapeutics and pharmacology focusing on concise rapid reporting of clinical studies and reviews in COPD. Special focus is given to the pathophysiological processes underlying the disease, intervention programs, patient focused education, and self management

protocols. This journal is indexed on PubMed Central, MedLine and CAS. The manuscript management system is completely online and includes a very quick and fair peer-review system, which is all easy to use. Visit <http://www.dovepress.com/testimonials.php> to read real quotes from published authors.

Submit your manuscript here: <https://www.dovepress.com/international-journal-of-chronic-obstructive-pulmonary-disease-journal>

RESEARCH ARTICLE

Open Access



Characterizing MRI features of rectal cancers with different KRAS status

Yanyan Xu¹, Qiaoyu Xu¹, Yanhui Ma¹, Jianghui Duan¹, Haibo Zhang¹, Tongxi Liu¹, Lu Li¹, Hongliang Sun^{1*} , Kaining Shi², Sheng Xie¹ and Wu Wang¹

Abstract

Background: To investigate whether MRI findings, including texture analysis, can differentiate KRAS mutation status in rectal cancer.

Methods: Totally, 158 patients with pathologically proved rectal cancers and preoperative pelvic MRI examinations were enrolled. Patients were stratified into two groups: KRAS wild-type group (KRAS^{wt} group) and KRAS mutation group (KRAS^{mt} group) according to genomic DNA extraction analysis. MRI findings of rectal cancers (including texture features) and relevant clinical characteristics were statistically evaluated to identify the differences between the two groups. The independent samples t test or Mann-Whitney U test were used for continuous variables. The differences of the remaining categorical polytomous variables were analyzed using the Chi-square test or Fisher exact test. A receiver operating characteristic (ROC) curve analysis was performed to evaluate the discriminatory power of MRI features. The area under the ROC curve (AUC) and the optimal cut-off values were calculated using histopathology diagnosis as a reference; meanwhile, sensitivity and specificity were determined.

Results: Mean values of six texture parameters (Mean, Variance, Skewness, Entropy, gray-level nonuniformity, run-length nonuniformity) were significantly higher in KRAS^{mt} group compared to KRAS^{wt} group ($p < 0.0001$, respectively). The AUC values of texture features ranged from 0.703~0.813. In addition, higher T stage and lower ADC values were observed in the KRAS^{mt} group compared to KRAS^{wt} group ($t = 7.086$, $p = 0.029$; $t = -2.708$, $p = 0.008$).

Conclusion: The MRI findings of rectal cancer, especially texture features, showed an encouraging value for identifying KRAS status.

Keywords: Rectal cancer, Magnetic resonance imaging, Texture, KRAS mutation

Background

Colorectal cancer (CRC) is one of the major causes of cancer-related mortality with over 1 million new cases diagnosed worldwide each year [1, 2]. It is viewed as a heterogeneous disorder due to its molecular features and relevant subtypes, and can be divided into five molecular subtypes correlated to tumor morphological features with different DNA microsatellite instability status and CpG island methylator phenotype [1]. Notably, KRAS mutation is closely linked to villous change and dysplasia [2]. Adenocarcinoma with KRAS mutation that is

considered a subgroup of CRC show a negative treatment response to epidermal growth factor receptor (EGFR)-targeted antibodies [3]. Furthermore, KRAS mutation is an established biomarker in clinical practice for CRC and is associated with distant metastasis [4], and poorer survival in CRC [5–7]. Approximately 30–40% CRCs have KRAS mutation, while rectal cancer accounts for 30–35% among CRC [8, 9]. The pre-operative neoadjuvant therapy including anti-EGFR chemotherapy has shown robust value in the management of rectal cancer [3]. Therefore, it is important to select suitable patients who could benefit from aggressive multimodality approaches and to tailor individual treatments against the disease.

* Correspondence: stentorsun@gmail.com

¹Department of Radiology, China-Japan Friendship Hospital, No.2 Yinghua East Street, Chaoyang District, Beijing 100029, People's Republic of China
Full list of author information is available at the end of the article



© The Author(s). 2019 **Open Access** This article is distributed under the terms of the Creative Commons Attribution 4.0 International License (<http://creativecommons.org/licenses/by/4.0/>), which permits unrestricted use, distribution, and reproduction in any medium, provided you give appropriate credit to the original author(s) and the source, provide a link to the Creative Commons license, and indicate if changes were made. The Creative Commons Public Domain Dedication waiver (<http://creativecommons.org/publicdomain/zero/1.0/>) applies to the data made available in this article, unless otherwise stated.

Currently, information pertaining to the KRAS status can only be gathered from the biopsy samples or postoperative specimens. Furthermore, the limitations of histological evaluation of KRAS status, such as the variability in the tissue sample and the poor DNA quality in sample results, can lead to discordance between biopsy material and final operative results [10]. Thus, efficient identification of KRAS status in patients with rectal cancer using non-invasively method would be of great clinical interest.

On the other hand, different molecular subtypes correlate with various discriminating morphological features [1]. Various MR imaging modules [11–16] (i.e. diffusion-weighted MR imaging [DWI], magnetic resonance spectroscopy [MRS], arterial spin labelling [ASL]) and advanced analysis for routine MR imaging [17–21] have been introduced in the oncologic field to evaluate tumoral biological characteristics and predict KRAS status. Nevertheless, the radiologic features of rectal cancer with KRAS mutation have not yet been fully described. Texture analysis is a noninvasive method used for assessment of the intra-tumoral heterogeneity not perceptible by human eye, which has a promising value in predicting therapy response, survival and discriminating different stages in rectal cancer [22–24]. However, to date, there have been no studies to assess whether texture analysis of MRI can be used as an imaging biomarker for KRAS status in rectal cancer.

Hence, the main objects of the present study were to 1) retrospectively analyze the differences of radiologic features in rectal cancer with different KRAS status; 2) investigate whether texture features extracted from T2 weighted image scan differentiate KRAS mutation status in rectal cancers.

Methods

Patients and tissue samples

This retrospective study was approved by the institutional review board of Institute of Clinical Medicine, China-Japan Friendship Hospital (No. 2015–012), and written informed consent was waived. A total of 220 patients underwent rectal resection for adenocarcinoma with complete clinical data and preoperative pelvic MR examination (including T2WI-high resolution sequence) between June 2013 and September 2015. Exclusion criteria included: i) pre-examination neoadjuvant chemoradiotherapy ($n = 45$) or unidentified herbal medicine therapy ($n = 5$); ii) poor image quality [heavy intestinal peristalsis artifacts ($n = 10$), too small lesions (diameter < 5 mm) or lesions difficult to identify on DWI images ($n = 2$)]. Finally, the group included in the study comprised 158 patients (106 men, 52 women) with a mean age of (60.66 ± 13.38) years (range 26–87 years). Among the 158 subjects, the data of 45 subjects were previously

analyzed with a different objective for other research [18].

Surgical pathology results from all patients were analyzed by a pathologist with 6 years' experience in gastrointestinal pathological diagnosis. Genomic DNA was extracted from formalin fixed paraffin-embedded (FFPE) tissue using QLAamp DNA FFPE Tissue kit (Qiagen, Germany), and KRAS mutations were examined by amplification refractory mutation system (ARMS) method.

Patient preparation and imaging protocol

Patients were on a low-residue diet before the exam and fasted on the day of the exam. Intramuscular injection of 10 mg anisodamine hydrochloride was given to each patient to inhibit the intestine peristalsis some 10 min before MRI examination. Pelvis MR scanning was implemented on a 3 T whole-body scanner (Ingenia, Philips Medical Systems, Best, the Netherlands) with gradient strength 45mT/m and gradient slew rate 200mT/m/ms, using a 16-channel anterior torso dS coil and a 16-channel posterior table dS coil. 2D sagittal and coronal T2W TSE sequences were performed with following parameters: TR 3761 ms, TE 110 ms, FOV 24×24 cm, slice thickness 3 mm with 0.3 mm gap, acquisition matrix 336×252 , NSA 3. Oblique axial T2W-high resolution sequence was planned perpendicularly to the bowel with tumor: TR 3865 ms, TE 100 ms, FOV 14×14 cm, slice thickness 3 mm with 0.3 mm gap, acquisition matrix 232×228 . Oblique axial diffusion weighted imaging (DWI) scan perpendicularly to the tumor was implemented using a single-shot echo planar imaging with following parameters: TE/TR 76/6000 ms, FOV 20×30 cm, slice thickness 5 mm with 0.2 mm gap, acquisition matrix 292×304 , NSA 6, 2 b values ($0, 1000 \text{s/mm}^2$).

Image analysis

All the data was transmitted to picture archiving and communication system (PACS) and Philips post-processing workstation. Two radiologists (with 11 and 7 years in gastrointestinal imaging), who were blinded to all clinical information, independently measured and recorded the following tumor features: tumor type, location, length, morphologic features, circumferential extent, T staging and the maximal extramural depth (MEMD) of tumor, N staging, circumferential resection margin (CRM), extramural vascular invasion (EMVI), ADC values, textural features. However, they were aware that the study subjects were patients with rectal cancers. For continuous variables, an average value of two observers' measurement was selected. For categorical variables, the diagnosis was determined after renegotiation by two observers if any interobserver discrepancies occurred.

Tumor type

According to the signal intensity of rectal cancers on T2WI [25], the hyperintensity was defined as a signal intensity that was similar to or brighter than the perirectal fat. Each observer quantitatively evaluated hyperintense volume in the tumor and determined the type of tumor as “mucinous” or “non-mucinous” according to the same criteria used for pathologic diagnosis (at least ≥50% of the mucin pool occupying the tumor mass [26].

Tumor location and length

Tumor location, as well as tumor length were primarily evaluated on sagittal T2-weighted images. Axial and coronal T2-weighted images were used secondarily when required. The rectum was generally divided into three parts according to the anatomic distance from the anal verge: the upper third (> 10 cm), middle third (5-10 cm), lower third (< 5 cm). The anal verge was defined as the end of the anal canal [27]. The distance between the lower margin of rectal lesion and anal verge were measured by drawing along the midline of rectal lumen in a zigzag pattern [28]. Tumor length was also measured along the intestinal lumen in a zigzag pattern.

Morphologic criteria/tumor shape

Tumor shapes were classified [27] as (a) intraluminal polypoid lesion (without abutting pericorectal tissues) (Fig. 1); (b) ulcerofungating/ulceroinfiltrative mass (Fig. 2); (c) bulky (Fig. 3). If the tumor showed growth tendency of protruding mass into colorectal lumen or limited thickening-wall with a sharp margin from the adjacent normal intestinal wall, without breaching the

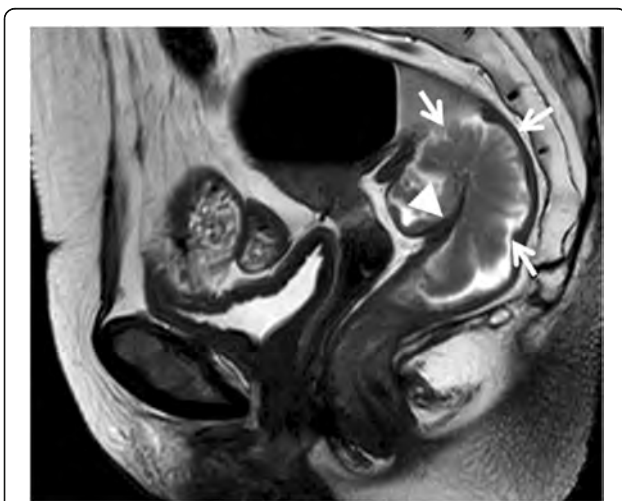


Fig. 1 Sagittal T2-weighted imaging of a rectal cancer (intermediate signal intensity) presenting as polypoid mass (arrows) protruded into lumen with distinct intestinal wall (arrow head). Result of the postoperative pathology confirmed that the tumor invaded the submucosa without extending into muscularis propria

outer margin, it was considered as the intraluminal polypoid lesion. If the tumor demonstrated wall-thickening grow tendency with abutting pericorectal tissue, and MEMD < 10 mm, it was considered as the ulcerofungating/ulceroinfiltrative mass. If the tumor showed exophytic growth tendency with disproportionately expanding component outside the imaginary line of the main tumor (MEMD ≥ 10 mm), and the outer diameter of the tumor-bearing segment was larger than that of the adjacent normal colorectal segment, then it was considered a bulky mass.

Circumferential extent

Axis bowel (clock face) was divided into quarters, C1: tumor extent ≤ 1/4 bowel circumference; C2: tumor extent > 1/4 bowel circumference and ≤ 1/2 bowel circumference; C3: tumor extent > 1/2 bowel circumference and ≤ 3/4 bowel circumference; C4: tumor extent > 3/4 bowel circumference.

Tumor and node staging

Primary tumor and lymph node stage were observed on MRI [29] by using the Tumor-Node-Metastasis (TNM) staging system. Meanwhile, the MEMD of tumor was recorded, and T3 sub-stages were then classified [30] according to different MEMD. T3 sub-stage: T3a: MEMD < 1 mm beyond muscularis propria; T3b: MEMD ≥ 1-5 mm beyond muscularis propria; T3c: MEMD > 5-15 mm beyond muscularis propria; T3d: MEMD > 15 mm beyond muscularis propria. Nodes with irregular borders, mixed signal intensity, or both were suspected for metastasis, and presence of one to three suspicious nodes was defined as stage N1 and presence of four or more as stage N2.

CRM

The potential positive margin was defined as rectal tumor spread within 1 mm of the mesorectal fascia (Fig. 3), that occurred due to tumor deposits, tumor extramural extent, EMVI, or suspicious lymph nodes [30].

EMVI

EMVI was defined as the presence of rectal tumor cells within blood vessels located beyond the muscularis propria in the mesorectal fat [30]. The following clues for EMVI (Fig. 4) were (a) vessel expanded by tumor, having irregular contour; (b) presence of tumor signal intensity within vascular structure.

ADC evaluation

Images of diffusion-weighted (DW) sequence were transferred to the Extended Workspace 4.1 (Philips Medical Systems, Best, Netherlands). Regions of interest (ROIs) were manually drawn to cover the entire tumor area on

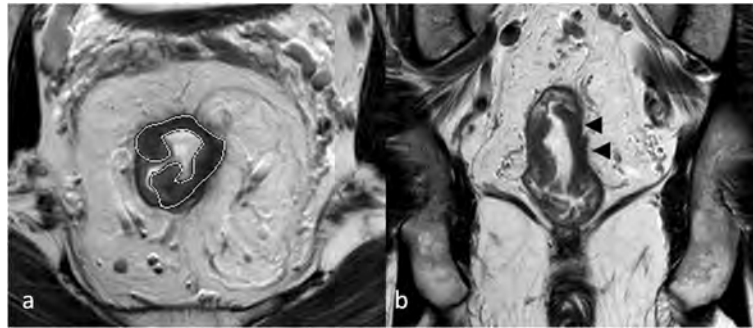


Fig. 2 T2-weighted imaging of a rectal cancer (low to intermediate signal intensity) presenting as ulceroinfiltrative mass (a, oblique axial, outline indicates tumor region) mainly extended along the intestinal wall with ambiguous muscularis propria (b, coronal, arrow head). Final pathologic results demonstrated that tumor invaded through muscularis propria to perirectal tissues

the axial slices containing all available tumor areas, which appeared as high signal on the DW images, avoiding the gas in the bowel and other anatomy structures.

Textural features

For each tumor, consecutive three axial T2W images (encompassing the tumor maximum cross-section as the middle slice) were conducted for textural analysis by using MaZda, version 4.6 (P.M. Szczypiński, Institute of Electronics, Technical University of Lodz, Poland). Free-hand ROIs were delineated with the tumor contour on axial images avoiding the inclusion of intestinal gas, liquid and anatomical structures. Although contouring was performed using T2WI images, the observers looked

at DW images, when available, to most accurately place the ROI.

Prior to analysis, MR image intensities were normalized between the range $[\mu - 3\sigma, \mu + 3\sigma]$, where μ was the mean value of gray levels inside the region of interest and σ denoted the standard deviation. Gray levels between $[\mu - 3\sigma]$ and $[\mu + 3\sigma]$ were then decimated to 64 Gy levels. This normalization procedure has been shown to minimize inter-scanner effects in MRI feature analysis [31]. Given that this analysis produced much more features than positive cases in the study, only first- and second-order texture features (three features) were selected for further analysis to avoid overfitting [32, 33]. Totally, 25 parameters, which are listed in Table 1, were extracted for each ROI on each slice. Run-length matrix (RLM) parameters were calculated four times for each ROI (vertical, horizontal, 45°, 135°) and grey-level co-occurrence matrix (GLCM) parameters were calculated

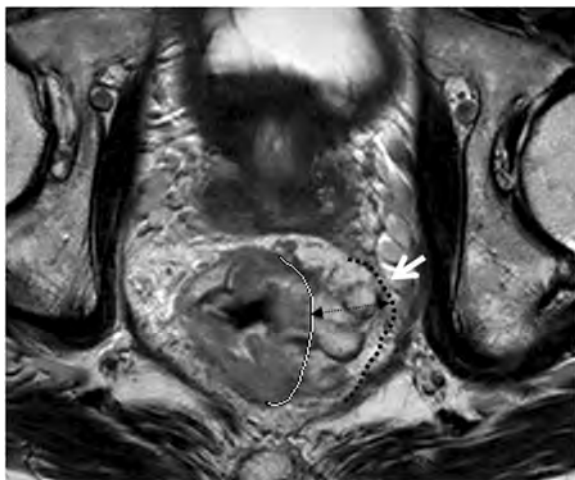


Fig. 3 Oblique axial T2-weighted imaging of a rectal mucinous adenocarcinoma (intermediate to high signal intensity) presenting as bulky mass showed significant tumor infiltration beyond the muscularis propria; the maximal extramural depth (MEMD, double-headed arrow) was over 10 mm. Meanwhile, the invasive border of rectal mass bordering the mesorectal fascia (white arrow) which led to a CRM of 0 mm. White line = muscularis propria border. Black dashed line = the mesorectal fascia

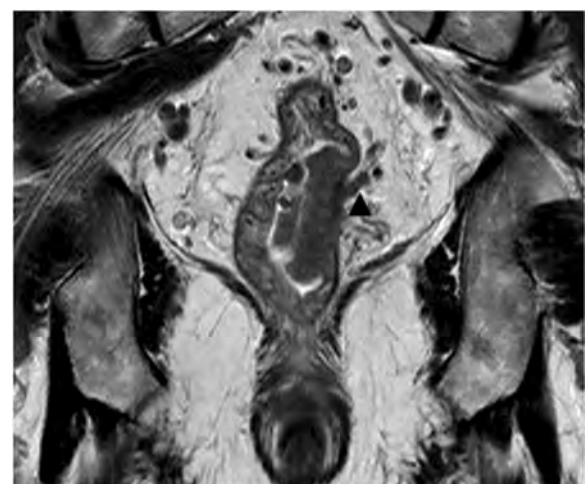


Fig. 4 Extramural vascular invasion (EMVI) involvement. Coronal T2-weighted imaging showing focal expansion of the small perirectal vessel with intermediate signal intensity (black arrow head)

Table 1 Summary of parameters belonging to first- and second-order texture features³³⁻³⁵

Texture feature	Histogram (n=9)	Run-length matrix (n=5)	Grey-level co-occurrence matrix (n=11)
Level/Order	First order	Second order	Second order
Description	Histogram where x-axis represents pixel/voxel gray level and y-axis represents frequency of occurrence	Adjacent or consecutive pixels/voxels of a single gray level in a given direction	How often pairs of pixels with specific values in a specified spatial range occur in an image
Parameters	Mean standard deviation skewness Kurtosis Perc.1% Perc.10% Perc.50% Perc.90% Perc.99%	Short run-length emphasis Long run-length emphasis Run-length non-uniformity Grey-level non-uniformity Fraction of image in runs	Angular second moment Contrast Correlation Sum of squares Inverse difference moment Sum average Sum variance Sum entropy Entropy Difference variance Difference entropy

20 times for each ROI at a variety of pixel offsets. For the comparison of textural features between tumors with different KRAS status, the mean value of gray-level histogram, RLM and GLCM parameters were used for each ROI, providing in total 25 parameters for analysis. Then, three parameters derived from gray-level histogram (*Mean, Variance, Skewness*), one parameter from gray-level co-occurrence matrix (GLCM) (*Entropy*) and two parameters from RLM (*gray-level nonuniformity* [GLNU], *run-length nonuniformity* [RLNU]) were extracted for each of the three slices based on the probability of classification error and the average correlation coefficients (POE + ACC) [34]. The detailed description of the calculated texture parameters was provided by Haralick et al. [35].

The selected feature sets were evaluated using the computer program B11, which is part of the MaZda software package. Artificial neural network (ANN) classifier [34] was employed for investigating the ability of texture feature sets to distinguish between rectal cancers with different KRAS status. The classification results were arbitrarily divided into several levels according to the misclassification rates: excellent (misclassification rates ≤ 10%), good (10% < misclassification rates ≤ 20%), moderate (20% < misclassification rates ≤ 30%), fair (30% < misclassification rates ≤ 40%), and poor (misclassification rates ≥ 40%) [36].

Statistical analysis

The statistical analysis was performed by SPSS (SPSS 17.0 for Windows, SPSS, Chicago, IL). The Kolmogorov-Smirnov test for normality was performed on

continuous variables and the graphical spread of the data was visually inspected. Descriptive statistics were shown as mean ± standard deviation (SD) or median ± interquartile range (IQR) for continuous variables, and as frequency and percentage for categorical variables. Interobserver agreement for continuous variables (ADC values, tumor length, MEMD, textural parameters) was evaluated using the intra-class correlation coefficient (ICC), and for categorical variables using Kappa of agreement. The Kappa value was interpreted as follows: < 0, poor agreement; 0 to 0.20, slight agreement; 0.21 to 0.40, fair agreement; 0.41 to 0.60, moderate agreement; 0.61 to 0.80, substantial agreement; and > 0.80, almost perfect agreement.

Patients were stratified into two groups: KRAS wild-type group (KRAS^{wt} group) and KRAS mutation group (KRAS^{mt} group) according to genomic DNA extraction and analysis. Mann-Whitney U test was used to compare variables (MEMD, texture features) with abnormal distribution for differentiation of rectal cancers with different KRAS status. The independent samples *t* test was used to compare other continuous variables (including ADC values, length and patients' age) between KRAS^{wt} and KRAS^{mt} group. Then, the differences among the other categorical variables were analyzed using the chi-square test or Fisher exact test. A receiver operating characteristic (ROC) curve analysis was performed to evaluate the discriminatory power of MRI features including ADC values, tumor shape, T stage and textural features in differentiating tumor KRAS mutation. The area under the curve (AUC) and optimal cutoff values were calculated, as well as the corresponding sensitivity

and specificity. $P < 0.05$ indicated a statistically significant difference.

Results

Patient characteristics

Of 158 patients (mean age, 60.66 ± 13.38), 143 (90.51%) had cancers detected according to symptoms such as abdominal pain, hematochezia, changes in bowel habits and diarrhea, 10 (6.33%) had screen-detected cancers, and the cancers in the remaining 5 patients (3.16%) were discovered during the examination for other diseases. According to final pathological results, 98 (62.03%) had KRAS^{wt} and 60 (37.97%) had KRAS^{mt} type cancer. MRI features and patients' clinical characteristics in KRAS^{wt} group and KRAS^{mt} group are shown in Table 2.

Quantitative textural analysis and ADC

Mean values of six texture features were significantly different in rectal cancers with different KRAS status ($p < 0.0001$). In addition, good classification results (error of 12.7%) were obtained with ANN classifier. Lower ADC values were observed in the KRAS^{mt} group compared to the KRAS^{wt} group ($t = -2.708$, $p = 0.008$). The observed results are listed in Table 2.

Conventional imaging analysis

With regard to tumor shape, the shape distribution between the two groups was quite different ($\chi^2 = 7.591$, $p = 0.022$), with higher incidences of bulky (21.67%) and less intraluminal polypoid mass (15.00%) in the KRAS^{mt} group compared to (10.20 and 31.63%, respectively) KRAS^{wt} group, respectively. In addition, higher T stage was observed more frequently in the KRAS^{mt} group compared to the KRAS^{wt} group ($\chi^2 = 7.086$, $p = 0.029$). Moreover, the mean MEMD in the KRAS^{mt} group was significantly larger than in the KRAS^{wt} group ($Z = -2.202$, $p = 0.028$), and relevant T3 sub-stage distribution in two groups showed a similar trend ($\chi^2 = 8.240$, $p = 0.041$).

Although rectal cancers with KRAS mutation were mainly located in the middle-low part of rectum and had an extent of over 3/4 bowel circumference, there was no statistical difference between the KRAS^{mt} group and the KRAS^{wt} group ($p = 0.095$ and 0.872 , respectively). Other imaging features including length, N staging, EMVI, CRM also demonstrated no significant difference between the two groups. Moreover, the incidence of mucinous adenocarcinomas in the KRAS^{mt} group was higher than in the KRAS^{wt} group. Yet, no significant difference was demonstrated ($\chi^2 = 0.346$, $p = 0.556$) between the two groups. The observed results are listed in Table 2.

ROC analysis

The ROC curve of the ADC values is shown in Fig. 5. The AUC of ADC values was 0.682 (95%CI: 0.564~0.801); at a cutoff value of $1.145 \times 10^{-3} \text{ mm}^2/\text{s}$, the sensitivity and specificity were 66.67, 62.12%, respectively. The ROC curve of the quantitative texture values is shown in Fig. 6. According to ROC curve, textural features: *Mean*, *Variance*, *Skewness*, *Entropy*, GLUN and RLUN values showed diagnostic significance with the AUC values of 0.754, 0.759, 0.703, 0.800, 0.802 and 0.813, respectively. The optimal cutoff values for the above features and their relevant sensitivity, and specificity are listed in Table 3.

Interobserver agreement

Relatively good to excellent interobserver agreement was obtained for continuous variables ADC values, tumor length, MEMD, textural features with ICC values ranging from 0.719 to 0.9487, 0.9838 to 0.9963, 0.9643 to 0.9918, and 0.6379 to 0.8159, respectively. The interobserver agreement for categorical variables measured by the Kappa value ranged from 0.729 to 1.0. EMVI had a substantial agreement (Kappa value, 0.729), while the remaining MRI features showed almost perfect agreement (Kappa value > 0.8) (Table 4).

Discussion

In the present study, we found that 1) the textural analysis based on T2 weighted images had robust value in differentiating KRAS status in rectal cancer; 2) rectal cancers with KRAS mutation showed lower ADC value and manifested as ulcerofungating/ ulceroinfiltrative mass or had bulky shape, behaving more aggressive to surrounding tissue with larger MEMD and higher T stage. To our knowledge, this study is the first that explored the potential of textural analysis for predicting KRAS status in rectal cancer based on MR images.

Although textural features are inconsistent for variable software vendors, the focus key in texture analysis has been on assessing heterogeneity in tumor images [37]. Each texture feature measures a particular property of the arrangement of pixels within ROIs. Theoretically, a number of these features are correlated with intra-tumor heterogeneity attributed to various factors including necrosis, hypoxia, angiogenesis, hemorrhage, even genetic variations [37–41]. For example, *Variance* is negatively associated with angiogenesis in CRCs without KRAS mutant, while positive association has been demonstrated between *Skewness* and angiogenesis in CRCs with KRAS mutant [41]. *Entropy* derived from GLCM measures the disorder of an image [35]. If the image is heterogeneous, many of the elements in the co-occurrence matrix will have very small values, thus implying a very large entropy [42]. In the present study, rectal cancer

Table 2 MRI features and clinical characteristics of patients with rectal cancer(n=158)

Factors	Total (No./ values)	KRAS Status		P-value
		Wild-type (n=98)	Mutant (n=60)	
Age	60.66±13.38	60.42±12.89	61.07±14.26	0.388
Gender				0.769
Male	106	66(67.35%)	40(66.67%)	
Female	52	32(32.65%)	20(33.33%)	
ADC (×10 ⁻³ mm ² /ms)	1.22±0.39	1.37±0.37	1.15±0.38	0.008*
Texture features				
Mean	66.47±14.55	62.66±10.53	73.34±18.38	<0.0001
Variance	289.19±118.96	267.65±122.51	334.39±94.27	<0.0001
Skewness	0.54±0.67	0.43±0.53	0.73±0.42	<0.0001
Entropy	1.89±0.23	1.80±0.19	1.97±0.14	<0.0001
RLUN	178.38±65.19	159.87±53.38	208.12±69.14	<0.0001
GLUN	7.53±3.44	6.55±2.83	9.26±3.33	<0.0001
Tumor location				
Upper Rectum	48	33(33.67%)	15(25.00%)	0.095
Middle Rectum	72	47(47.96%)	25(41.67%)	
Lower Rectum	38	18(18.37%)	20(33.33%)	
Tumor shape				0.022
Intraluminal polypoid mass	40	31(31.63%)	9(15.00%)	
Ulcerofungating/Ulceroinfiltrative mass	95	57(58.16%)	38(63.33%)	
Bulky	23	10(10.20%)	13(21.67%)	
Tumor length(cm)	4.12±1.68	4.04±1.62	4.25±1.78	0.446*
Tumor type				0.556
Mucinous adenocarcinoma	23	13(13.27%)	10(16.67%)	
Non-mucinous adenocarcinoma	135	85(86.73%)	50(83.33%)	
Cirumferential extent				0.872**
C1	6	4(4.08%)	2(3.33%)	
C2	56	36(36.73%)	20(33.33%)	
C3	56	34(34.69%)	22(36.67%)	
C4	40	24(24.49%)	16(26.67%)	
Radiologic T stage				0.029
T1-2	49	35(35.71%)	14(23.33%)	
T3	94	58(59.18%)	36(60.00%)	
T4	15	5(5.10%)	10(16.67%)	
T3 substage				0.041
T3a	23	19(32.76%)	4(11.11%)	
T3b	36	23(39.66%)	13(36.11%)	
T3c	23	11(18.97%)	12(33.33%)	
T3d	12	5(8.62%)	7(19.44%)	
MEMD(cm)	0.30±0.60	0.30±0.60	0.50±0.60	0.028*
N stage				0.754
N0	74	48(48.98%)	26(43.33%)	
N1	51	31(31.63%)	20(33.33%)	

Table 2 MRI features and clinical characteristics of patients with rectal cancer(n=158) (Continued)

Factors	Total (No./ values)	KRAS Status		P-value
		Wild-type (n=98)	Mutant (n=60)	
N2	23	19(19.39%)	14(23.33%)	0.664
EMVI				
Positive	34	20(20.41%)	14(23.33%)	
Negative	124	78(79.59%)	46(76.67%)	
CRM				0.337
Positive	38	28(28.57%)	13(21.67%)	
Negative	120	70(71.43%)	47(78.33%)	

Abbreviations: ADC apparent diffusion coefficient, MEMD the maximal extramural depth of tumour; EMVI extramural vascular invasion, CRM circumferential resection margin, RLNU run-length nonuniformity, GLNU grey-level nonuniformity
 *independent samples t test, data is mean ± standard deviation; Δ Mann-Whitney U test, data is data is median ± interquartile range. **Considering limited patients' numbers in subgroups of circumferential extent, reclassification was adopted as follows: C1-2, C3, and C4, and P value was the result of new categorization

with KRAS mutation had higher Entropy values compared to the KRAS^{wt} group ($p < 0.0001$). In other words, rectal cancer with KRAS mutation had higher intrinsic heterogeneity than KRAS wild-type cancers did; this intrinsic heterogeneity in KARS mutation should be addressed more in detail by further research.

Encouraging results on texture analysis for differentiating benign and malignant lymph nodes, identifying T stage and predicting outcome after chemoradiotherapy in rectal cancer have been reported by previous studies using different imaging modalities including CT, MR, and ultrasound [22–24, 43, 44]. In this study, we performed the texture analysis of rectal cancer using T2

weighted images from MR, which is the gold-standard imaging technique for preoperative staging and is also the standard routine for patients with rectal cancer at our hospital. Furthermore, MRI could reduce the impact of image noise on biological heterogeneity with higher contrast resolution and contrast-to-noise ratio compared with CT [24].

As mentioned above, the lower ADC value observed in rectal cancers with KRAS mutation may suggest an unfavorable tumor profile. Recent studies have revealed that low ADC values are associated with poorly differentiated tumors and high tumor stages in rectal cancers [45, 46] It is well known that ADC value is inversely correlated with the cellularity and positively correlated with necrosis and cystic changes in tissues. Hence, lower ADC value might reflect less necrosis, higher cellular density, and higher vascularization, suggesting the aggressiveness of the tumor profile [47]. Furthermore, it has been reported that lung metastasis is more likely to develop in CRCs with KRAS mutation than in KRAS wild-type [48]. These findings are indirectly consistent with our results.

In the present study, higher incidences of bulky CRCs were observed in the KRAS^{mt} group compared to the KRAS^{wt} group. Kim et al [27] have shown a higher incidence of bulky CRCs in the poorly differentiated CRCs than in the well- or moderately differentiated CRCs, and poor differentiation is associated with high risk of post-operative relapse in stage II CRCs [49]. Thus, it is proposed that bulky CRCs are more likely to have a poor prognosis. Actually, according to classification criteria [27], bulky tumors had exophytic growth tendency with MEMD > 10 mm in our study. Cho and colleagues [49] have reported that significantly higher 3-year recurrence rate after surgical treatment is observed in rectal cancers with MEMD > 10 mm than in tumors with MEMD ≤ 10 mm, which supported our hypothesis. Consequently, it

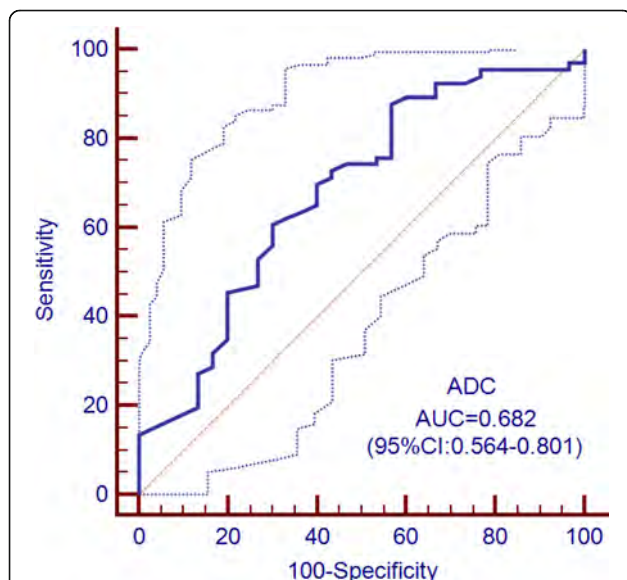
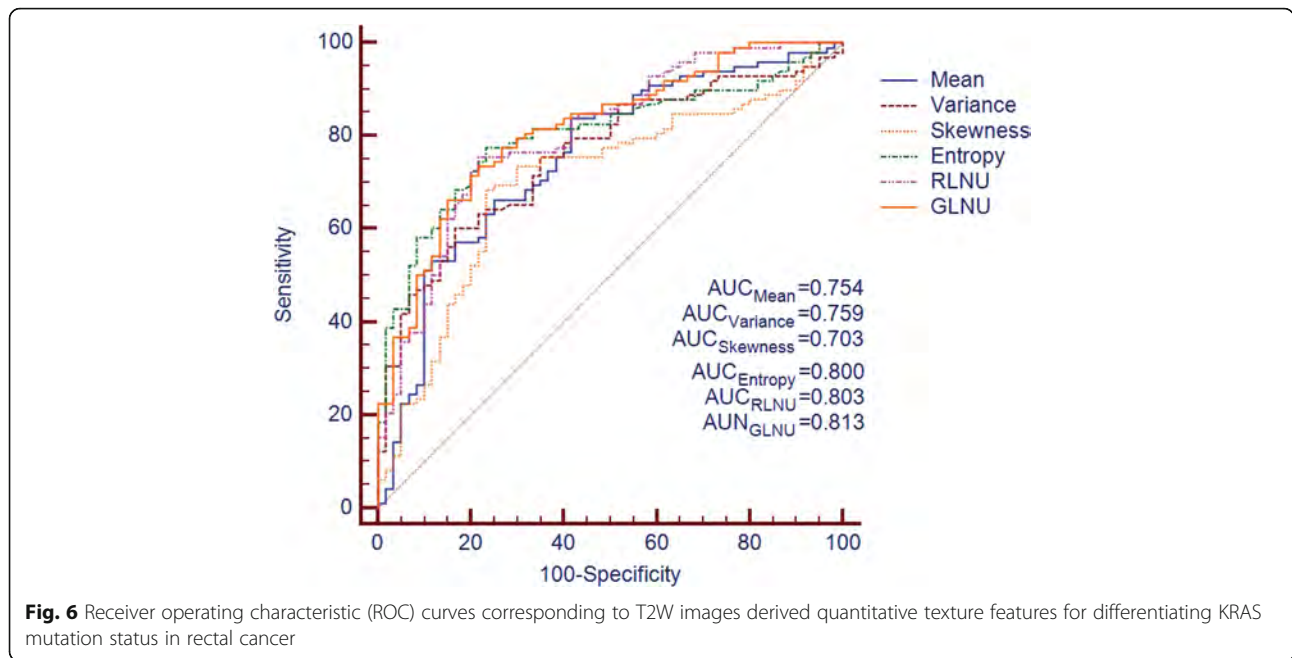


Fig. 5 Receiver operating characteristic (ROC) curves (solid line) and 95% confidence bounds (dotted lines) for ADC values in differentiating KRAS mutation status in rectal cancer



is easy to understand the relatively higher incidence of bulky CRCs in the KRAS^{mt} group.

In daily practice, the biopsy is still the routine way to get tumour mutant status before treatment. Considering the spatial and temporal intra-tumour molecular heterogeneity, the results for biopsy samples are yet to be consistent [11–13, 50]. Recently, a large prospective study [50] showed that the concordance ratio between paired biopsy and resection specimens was 82% for KRAS status. In the current study, although the best sensitivity (*Variance*) and specificity (*Mean*) of the texture features were both over 83% in the study, the sensitivity and specificity of GLNU, which harboured the best diagnostic significance (AUC = 0.813), were both lower than 80%. These findings suggest that the textural analysis can potentially provide promising MRI biomarkers for KRAS status, however, the sensitivity of it still needs to be improved in further studies.

Table 3 Receiver operator characteristics of textural parameters for predicting KRAS status

Feature	AUC	SE(AUC)	95%CI(AUC)	Criterion	Se(%)	Sp(%)
Mean	0.754	0.040	0.674–0.833	>72.072	58.33%	83.67%
Variance	0.759	0.038	0.684–0.834	>281.700	83.33%	60.20%
Skewness	0.703	0.043	0.618–0.787	>0.554	80.00%	69.39%
Entropy	0.800	0.035	0.731–0.870	>1.893	76.67%	78.57%
RLNU	0.802	0.036	0.731–0.872	>186.350	78.33%	76.53%
GLNU	0.813	0.034	0.746–0.880	>7.846	78.33%	74.49%

Abbreviation: AUC area under the curve, SE standard error, Se sensitivity, Sp specificity, RLNU run-length nonuniformity, GLNU gray-level nonuniformity

There are some limitations in the current study. First, texture features were selected using POE + ACC algorithms in combination with ANN classifiers, and merely six features were extracted for further analysis in this study. Considering that a large number of features could be generated by MaZda software and that limited subjects were included in the study selective bias may exist

Table 4 Inter-observer agreement for variables

Inter-observer agreement for variables			
Variable Type	Variable	Kappa value/ICC	95%CI
Categorical	Tumor shape	0.919	0.863-0.974
	circumferential	0.979	0.965-1.0
	T stage	0.935	0.883-0.986
	N stage	0.940	0.898-0.981
	Tumor type	0.804	0.663-0.945
	EMVI	0.729	0.599-0.857
	CRM	0.812	0.694-0.930
Continuous	ADC	0.8542	0.7190-0.9487
	Tumor length	0.9885	0.9838-0.9963
	MEMD	0.9843	0.9643-0.9918
	Mean	0.7448	0.6663-0.8069
	Variance	0.7571	0.6818-0.8159
Skewness	0.7402	0.6607-0.8032	
Entropy	0.7452	0.6670-0.8072	
GLNU	0.7239	0.6379-0.7916	
RLNU	0.7539	0.6776-0.8141	

Inter-observer agreement of categorical variables was evaluated by Kappa or weighted Kappa value, while inter-observer agreement of continuous ones was evaluated by ICC

and further studies are required. Second, due to the complexity of the technique and a high number of parameters, high variability in data acquisition could be introduced in the MRI scan, and in theory could affect the reproducibility of the final results [24]. However, the differences in texture features extracted from MR images from different scanners seem to have only a weak impact on the results of tissue discrimination [34]. Third, with regard to the genomic results, our data were restricted to the KRAS mutations located in codons 12 and 13. Nevertheless, since codons 12 and 13 KRAS mutations represent the majority of RAS mutations in CRC, our results provide a reasonable representation for tumors with RAS mutation in some degree. Fourth, considering the potential discrepancy between pre-treatment biopsy and final pathology [11–13], only the outcome from final surgical specimen were enrolled in the study. Fifth, this was a single-center study with a limited sample size, which may be the reason why only moderate predictive value of MRI features for identifying KRAS status has been observed. Further work with a larger sample size may lead to more statistically significant results.

Conclusion

Overall, our preliminary results demonstrate that MRI features, including quantitative texture analysis derived from T2 weighted images, have the potential to differentiate the KRAS status in rectal cancers. The additional texture features may provide reference information for characterizing KRAS status with the expected impact on management of individualized diagnosis and treatment of rectal cancer.

Abbreviations

ADC: Apparent diffusion coefficient; ANN: Artificial neural network; ARMS: Amplification refractory mutation system; AUC: The area under the ROC curve; CRC: Colorectal cancer; CRM: Circumferential resection margin; DWI: Diffusion weighted imaging; EGFR: Epidermal growth factor receptor; EMVI: Extramural vascular invasion; FFPE: Formalin fixed paraffin-embedded; FOV: Field of view; GLCM: Grey-level co-occurrence matrix; GLNU: Gray-level nonuniformity; ICC: Intra-class correlation coefficient; IQR: Interquartile range; KRAS: Kirsten rat sarcoma viral oncogene homolog; MEMD: Maximal extramural depth; MRI: Magnetic resonance imaging; PACS: Picture archiving and communication system; RLM: Run-length matrix; RLNU: Run-length nonuniformity; ROC: Receiver operating characteristic; ROI: Region of interest; SD: Standard deviation; TE: Echo time; TNM: Tumor Node Metastasis; TR: Repetition time; TSE: Turbo spin echo

Acknowledgements

The authors wish to thank Dr. Queenie Chan for her technical support in editing the manuscript.

Authors' contributions

YX, QX and HS designed the study, and drafted the manuscript. YM, JD, HZ, TL, LL, KS, SX, and WW participated in study design. YX, QX and HS carried out data collection, data analysis, and manuscript revision. All authors reviewed the data and approved the final version of the manuscript.

Funding

This work has received funding from the Beijing Municipal Science & Technology Commission (No. Z181100001718099), National Natural Science

Foundation of China (81501469) and National health and family planning commission public service (201402019). The funding body had no involvement in the design of the study, collection, analysis, and interpretation of data and in writing the manuscript.

Ethics approval and consent to participate

This study was approved by our institutional ethics committee. For this type of retrospective study, formal consent was not required. The study was performed in accordance with the relevant guidelines and regulations.

Consent for publication

Not applicable.

Competing interests

The authors declare that they have no competing interests.

Author details

¹Department of Radiology, China-Japan Friendship Hospital, No.2 Yinghua East Street, Chaoyang District, Beijing 100029, People's Republic of China.

²Philips Healthcare, Beijing 100001, People's Republic of China.

Received: 22 July 2019 Accepted: 6 November 2019

Published online: 14 November 2019

References

- Coppèdè F, Lopomo A, Spisni R, Migliore L. Genetic and epigenetic biomarkers for diagnosis, prognosis and treatment of colorectal cancer. *World J Gastroenterol.* 2014;20(4):943–56.
- Jass JR. Classification of colorectal cancer based on correlation of clinical, morphological and molecular features. *Histopathology.* 2007;50(1):113–30.
- Yadamsuren EA, Nagy S, Pajor L, Lacza A, Bogner B. Characteristics of advanced- and non advanced sporadic polypoid colorectal adenomas: correlation to KRAS mutations. *Pathol Oncol Res.* 2012;18(4):1077–84.
- Misale S, Di Nicolantonio F, Sartore-Bianchi A, Siena S, Bardelli A. Resistance to anti-EGFR therapy in colorectal cancer: from heterogeneity to convergent evolution. *Cancer Discov.* 2014;4(11):1269–80.
- Zhu K, Yan H, Wang R, Zhu H, Meng X, Xu X, et al. Mutations of KRAS and PIK3CA as independent predictors of distant metastases in colorectal cancer. *Med Oncol.* 2014;31(7):16.
- Qiu LX, Mao C, Zhang J, Zhu XD, Liao RY, Xue K, et al. Predictive and prognostic value of KRAS mutations in metastatic colorectal cancer patients treated with cetuximab: a meta-analysis of 22 studies. *Eur J Cancer.* 2010; 46(15):2781–7.
- Guo TA, Wu YC, Tan C, Jin YT, Sheng WQ, Cai SJ, et al. Clinicopathologic features and prognostic value of KRAS, NRAS and BRAF mutations and DNA mismatch repair status: a single-center retrospective study of 1,834 Chinese patients with stage I-IV colorectal cancer. *Int J Cancer.* 2019;145(6):1625–34.
- Boeckx N, Peeters M, Van Camp G, Pauwels P, Op de Beeck K, Deschoolmeester V. Prognostic and predictive value of RAS gene mutations in colorectal Cancer: moving beyond KRAS exon 2. *Drugs.* 2015;75(15):1739–56.
- Hardiman KM. Update on sporadic colorectal Cancer genetics. *Clin Colon Rectal Surg.* 2018;31(3):147–52.
- Andreyev HJ, Norman AR, Cunningham D, Oates J, Dix BR, Iacopetta BJ, et al. Kirsten ras mutations in patients with colorectal cancer: the 'RASCAL II' study. *Br J Cancer.* 2001;85(5):692–6.
- Rönnow CF, Uedo N, Stenfors I, Toth E, Thorlacius H. Forceps biopsies are not reliable in the workup of large colorectal lesions referred for endoscopic resection: should they be abandoned? *Dis Colon Rectum.* 2019;62(9):1063–70.
- Nelson AC, Boone J, Cartwright D, Thyagarajan B, Kincaid R, Lambert AP, et al. Optimal detection of clinically relevant mutations in colorectal carcinoma: sample pooling overcomes intra-tumoral heterogeneity. *Mod Pathol.* 2018;31(2):343–9.
- Jeantet M, Tougeron D, Tachon G, Cortes U, Archambaut C, Fromont G, et al. High Intra- and Inter-Tumoral Heterogeneity of RAS Mutations in Colorectal Cancer. *Int J Mol Sci.* 2016;17(12):E2015.
- Abdel Razek AAK. Routine and advanced diffusion imaging modules of the salivary glands. *Neuroimaging Clin N Am.* 2018;28:245–54.

15. Abdel Razek AAK. Diffusion tensor imaging in differentiation of residual head and neck squamous cell carcinoma from post-radiation changes. *Magn Reson Imaging*. 2018;54:84–9.
16. Abdel Razek AA, Samir S, Ashmalla GA. Characterization of parotid tumors with dynamic susceptibility contrast perfusion-weighted magnetic resonance imaging and diffusion-weighted Mr imaging. *J Comput Assist Tomogr*. 2017;41:131–6.
17. Razek AA, Nada N. Correlation of choline/Creatine and apparent diffusion coefficient values with the prognostic parameters of head and neck squamous cell carcinoma. *NMR Biomed*. 2016;29:483–9.
18. Xu Y, Xu Q, Sun H, Liu T, Shi K, Wang W. Could IMM and ADC help in predicting the KRAS status in patients with rectal cancer? *Eur Radiol*. 2018; 28(7):3059–65.
19. Abdel Razek AAK, Talaat M, El-Serougy L, Gaballa G, Abdelsalam M. Clinical applications of arterial spin labeling in brain tumors. *J Comput Assist Tomogr*. 2019;43:525–32.
20. Yeo DM, Oh SN, Choi MH, Lee SH, Lee MA, Jung SE. Histogram analysis of perfusion parameters from dynamic contrast-enhanced MR imaging with tumor characteristics and therapeutic response in locally advanced rectal Cancer. *Biomed Res Int*. 2018;2018:3724393.
21. Meng X, Xia W, Xie P, Zhang R, Li W, Wang M, et al. Preoperative radiomic signature based on multiparametric magnetic resonance imaging for noninvasive evaluation of biological characteristics in rectal cancer. *Eur Radiol*. 2019;29(6):3200–9.
22. Liu L, Liu Y, Xu L, Li Z, Lv H, Dong N, et al. Application of texture analysis based on apparent diffusion coefficient maps in discriminating different stages of rectal cancer. *J Magn Reson Imaging*. 2017;45(6):1798–808.
23. Jalil O, Afaq A, Ganeshan B, Patel UB, Boone D, Endozo R, et al. Magnetic resonance based texture parameters as potential imaging biomarkers for predicting long-term survival in locally advanced rectal cancer treated by chemoradiotherapy. *Color Dis*. 2017;19(4):349–62.
24. De Cecco CN, Ganeshan B, Ciolina M, Rengo M, Meinel FG, Musio D, et al. Texture analysis as imaging biomarker of tumoral response to neoadjuvant chemoradiotherapy in rectal cancer patients studied with 3-T magnetic resonance. *Investig Radiol*. 2015;50(4):239–45.
25. Hussain SM, Outwater EK, Siegelman ES. Mucinous versus nonmucinous rectal carcinomas: differentiation with MR imaging. *Radiology*. 1999;213(1): 79–85.
26. Luo C, Cen S, Ding G, Wu W. Mucinous colorectal adenocarcinoma: clinical pathology and treatment options. *Cancer Commun*. 2019;39(1):13.
27. Kim JE, Lee JM, Baek JH, Moon SK, Kim SH, Han JK, et al. Differentiation of poorly differentiated colorectal adenocarcinomas from well- or moderately differentiated colorectal adenocarcinomas at contrast-enhanced multidetector CT. *Abdom Imaging*. 2015;40(1):1–10.
28. Han NY, Kim MJ, Park BJ, Sung DJ. Location of rectal cancer as determined using rectal magnetic resonance imaging, and its relationship with pulmonary metastasis. *Turk J Gastroenterol*. 2014;25(6):661–8.
29. Taylor FG, Swift RI, Blomqvist L, Brown G. A systematic approach to the interpretation of preoperative staging MRI for rectal cancer. *AJR Am J Roentgenol*. 2008;191(6):1827–35.
30. Nougaret S, Reinhold C, Mikhael HW, Rouanet P, Bibeau F, Brown G. The use of MR imaging in treatment planning for patients with rectal carcinoma: have you checked the "DISTANCE"? *Radiology*. 2013;268(2):330–44.
31. Collewet G, Strzelecki M, Mariette F. Influence of MRI acquisition protocols and image intensity normalization methods on texture classification. *Magn Reson Imaging*. 2004;22(1):81–91.
32. Szczypiński PM, Strzelecki M, Materka A, Klepaczko A. MaZda—a software package for image texture analysis. *Comput Methods Prog Biomed*. 2009; 94(1):66–76.
33. Lubner MG, Smith AD, Sandrasegaran K, Sahani DV, Pickhardt PJ. CT texture analysis: definitions, applications, biologic correlates, and challenges. *Radiographics*. 2017;37(5):1483–503.
34. Mayerhoefer ME, Breitsenseher MJ, Kramer J, Aigner N, Hofmann S, Materka A. Texture analysis for tissue discrimination on T1-weighted MR images of the knee joint in a multicenter study: transferability of texture features and comparison of feature selection methods and classifiers. *J Magn Reson Imaging*. 2005;22(5):674–80.
35. Haralick R, Shanmugam K, Dinstein I. Textural features for image classification. *IEEE Trans Syst Man Cybern*. 1973;3:610–21.
36. Yan L, Liu Z, Wang G, Huang Y, Liu Y, Yu Y, Liang C. Angiomyolipoma with minimal fat: differentiation from clear cell renal cell carcinoma and papillary renal cell carcinoma by texture analysis on CT images. *Acad Radiol*. 2015; 22(9):1115–21.
37. Miles KA, Ganeshan B, Hayball MP. CT texture analysis using the filtration-histogram method: what do the measurements mean? *Cancer Imaging*. 2013;13(3):400–6.
38. Gerashchenko TS, Denisov EV, Litviakov NV, Zavyalova MV, Vtorushin SV, Tsyganov MM, et al. Intratumor heterogeneity: nature and biological significance. *Biochemistry (Mosc)*. 2013;78(11):1201–15.
39. Nelson DA, Tan TT, Rabson AB, Anderson D, Degenhardt K, White E. Hypoxia and defective apoptosis drive genomic instability and tumorigenesis. *Genes Dev*. 2004;18(17):2095–107.
40. Ng F, Ganeshan B, Kozarski R, Miles KA, Goh V. Assessment of primary colorectal cancer heterogeneity by using whole-tumor texture analysis: contrast-enhanced CT texture as a biomarker of 5-year survival. *Radiology*. 2013;266(1):177–84.
41. Ganeshan B, Ziauddin X, Goh V, Rodriguez-Justo M, Engledow A, Taylor S, et al. Quantitative imaging biomarkers from PET-CT as potential correlates for angiogenesis and hypoxia in colorectal cancer. Vienna: European Society of Radiology; 2012.
42. Andrea B, Flavio P. An investigation of the textural characteristics associated with gray level co-occurrence matrix statistical parameters. *IEEE Trans Geoscience Remote Sensing*. 1995;33:293–304.
43. Chen SJ, Lin CH, Chang CY, et al. Characterizing the major sonographic textural difference between metastatic and common benign lymph nodes using support vector machine with histopathologic correlation. *Clin Imaging*. 2012;36(4):353–9.e2.
44. Bayanati H, E Thornhill R, Souza CA, et al. Quantitative CT texture and shape analysis: can it differentiate benign and malignant mediastinal lymph nodes in patients with primary lung cancer? *Eur Radiol*. 2015;25(2):480–7.
45. Curvo-Semedo L, Lambregts DM, Maas M, Beets GL, Caseiro-Alves F, Beets-Tan RG. Diffusion-weighted MRI in rectal cancer: apparent diffusion coefficient as a potential noninvasive marker of tumor aggressiveness. *J Magn Reson Imaging*. 2012;35:1365–71.
46. Sun Y, Tong T, Cai S, Bi R, Xin C, Gu Y. Apparent diffusion coefficient (ADC) value: a potential imaging biomarker that reflects the biological features of rectal cancer. *PLoS One*. 2014;9:e109371.
47. Xiao-ping Y, Jing H, Fei-ping L, Yin H, Qiang L, Lanlan W, et al. Intravoxel incoherent motion MRI for predicting early response to induction chemotherapy and chemoradiotherapy in patients with nasopharyngeal carcinoma. *J Magn Reson Imaging*. 2016;43(5):1179–90.
48. Pereira AA, Rego JF, Morris V, Overman MJ, Eng C, Garrett CR, et al. Association between KRAS mutation and lung metastasis in advanced colorectal cancer. *Br J Cancer*. 2015;112(3):424–8.
49. Cho SH, Kim SH, Bae JH, Jang YJ, Kim HJ, Lee D, et al. Prognostic stratification by extramural depth of tumor invasion of primary rectal cancer based on the Radiological Society of North America proposal. *AJR Am J Roentgenol*. 2014;202(6):1238–44.
50. Sclafani F, Wilson SH, Cunningham D, et al. Analysis of KRAS, NRAS, BRAF, PIK3CA and TP53 mutations in a large prospective series of locally advanced rectal cancer patients. *Int J Cancer*. 2019. <https://doi.org/10.1002/ijc.32507> [Epub ahead of print].

Publisher's Note

Springer Nature remains neutral with regard to jurisdictional claims in published maps and institutional affiliations.

Ready to submit your research? Choose BMC and benefit from:

- fast, convenient online submission
- thorough peer review by experienced researchers in your field
- rapid publication on acceptance
- support for research data, including large and complex data types
- gold Open Access which fosters wider collaboration and increased citations
- maximum visibility for your research: over 100M website views per year

At BMC, research is always in progress.

Learn more biomedcentral.com/submissions



Strain measurement on four-dimensional dynamic-ventilation CT: quantitative analysis of abnormal respiratory deformation of the lung in COPD

This article was published in the following Dove Medical Press journal:
International Journal of COPD

Yanyan Xu^{1,2}
Tsuneo Yamashiro¹
Hiroshi Moriya³
Maho Tsubakimoto¹
Yukihiro Nagatani⁴
Shin Matsuoka⁵
Sadayuki Murayama¹

On behalf of ACTIve Study Group

¹Department of Radiology, Graduate School of Medical Science, University of the Ryukyus, Nishihara, Okinawa, Japan; ²Department of Radiology, China-Japan Friendship Hospital, Beijing, Republic of China; ³Department of Radiology, Ohara General Hospital, Fukushima-City, Fukushima, Japan; ⁴Department of Radiology, Shiga University of Medical Science, Otsu, Shiga, Japan; ⁵Department of Radiology, St Marianna University School of Medicine, Kawasaki, Kanagawa, Japan

Purpose: Strain measurement is frequently used to assess myocardial motion in cardiac imaging. This study aimed to apply strain measurement to pulmonary motion observed by four-dimensional dynamic-ventilation computed tomography (CT) and to clarify motion abnormality in COPD.

Materials and methods: Thirty-two smokers, including ten with COPD, underwent dynamic-ventilation CT during spontaneous breathing. CT data were continuously reconstructed every 0.5 seconds. In the series of images obtained by dynamic-ventilation CT, five expiratory frames were identified starting from the peak inspiratory frame (first expiratory frame) and ending with the fifth expiratory frame. Strain measurement of the scanned lung was performed using research software that was originally developed for cardiac strain measurement and modified for assessing deformation of the lung. The measured strain values were divided by the change in mean lung density to adjust for the degree of expiration. Spearman's rank correlation analysis was used to evaluate associations between the adjusted strain measurements and various spirometric values.

Results: The adjusted strain measurement was negatively correlated with FEV₁/FVC ($\rho=-0.52$, $P<0.01$), maximum mid-expiratory flow ($\rho=-0.59$, $P<0.001$), and peak expiratory flow ($\rho=-0.48$, $P<0.01$), suggesting that abnormal deformation of lung motion is related to various patterns of expiratory airflow limitation.

Conclusion: Abnormal deformation of lung motion exists in COPD patients and can be quantitatively assessed by strain measurement using dynamic-ventilation CT. This technique can be expanded to dynamic-ventilation CT in patients with various lung and airway diseases that cause abnormal pulmonary motion.

Keywords: COPD, computed tomography, CT, dynamic-ventilation CT, strain measurement, emphysema

Introduction

Strain analysis, which can express deformation of a tissue or organ in the human body, has been mainly used to assess myocardial motion using various four-dimensional (4D) imaging modalities, including echocardiography, magnetic resonance imaging (MRI), and computed tomography (CT).¹⁻¹¹ Although various parameters based on strain measurements have been advocated by different software vendors, it is commonly accepted in the field of cardiology that strain is a sensitive parameter to assess regional function of the myocardium.⁴⁻¹¹ It has also been reported that strain measurements reveal minor left ventricular modifications in athletes with common anomalies (ie, bicuspid aortic valve),³ which might be masked by apparently normal values of

Correspondence: Tsuneo Yamashiro
Department of Radiology, Graduate School of Medical Science, University of the Ryukyus, 207 Uehara, Nishihara, Okinawa 903-0215, Japan
Tel +81 98 895 1162
Fax +81 98 895 1420
Email clatsune@yahoo.co.jp

global cardiac function parameters, such as ejection fraction and stroke volume.^{12,13}

In cardiology, a higher value of myocardial strain observed on MRI or echocardiography usually indicates better myocardial movement, because strong systolic–diastolic movements result in large deformation of the measured myocardium. However, it has also been shown that myocardial strain is heterogeneous in patients with dilated cardiomyopathy, suggesting heterogeneity of myocardial contractile function.⁵ Joseph et al presented color contour maps based on MRI strain measurements in patients with dilated cardiomyopathy and concluded that myocardial systolic strain has a heterogeneous regional distribution.⁵

In patients with COPD, the destruction of normal “mesh-like” structures of pulmonary tissue results in pulmonary emphysema and leads to a reduction of lung compliance, causing inhomogeneous transmission of lung motion during the respiratory cycle.¹⁴ Furthermore, the heterogeneous distribution of emphysematous changes and airway diseases also intensify the heterogeneity of lung movement during ventilation,^{15–17} which has been clearly confirmed in recent studies using 4D dynamic-ventilation CT and other imaging techniques.^{18–20} These recent studies have demonstrated the existence of asynchrony between the right and left lungs, between the proximal airways and lung, and among different lung lobes. However, to the best of our knowledge, there is no published information on motion abnormality of the entire scanned lung. Considering the similar physiologic characteristics of the lungs and heart (both show cyclic movements and changes in volume), we hypothesized that the quantitative strain measurement used in cardiology could be transferred to pulmonary 4D-CT imaging and generate new knowledge on normal and abnormal respiratory movements of the lungs. Also, we predicted that heterogeneity of lung motion, which would be similar to strain heterogeneity in dilated cardiomyopathy, can be demonstrated as abnormal deformation, or a high strain value in the targeted portion of the lungs.

Thus, the goals of this study were the following: 1) to first measure lung strain using 4D dynamic-ventilation CT, 2) to clarify abnormal deformation of lung motion by strain measurement, and 3) to assess correlations between strain and COPD severity.

Materials and methods

The Institutional Review Board at Ohara General Hospital approved this retrospective study. Based on the national guideline of the Japanese Government, the Institutional Review Board at Ohara General Hospital waived written informed

consent from enrolled patients for this study. Dynamic-ventilation CT and spirometry were performed as part of routine clinical care at Ohara Medical Center (part of Ohara General Hospital). This study was also part of the Area-detector Computed Tomography for the Investigation of Thoracic Diseases (ACTIve) Study, a multicenter research alliance in Japan. Also, the subjects’ data utilized in this study were previously analyzed with a different objective for other research.²⁰

Subjects

Thirty-two smokers (4 females and 28 males; mean age 70 ± 12 years) underwent both spirometry and chest CT (conventional and dynamic-ventilatory scans) at Ohara Medical Center. As the same patients were previously analyzed with a different objective,²⁰ the detailed information regarding the study population is described in the [Supplementary material](#). Patient data analyzed in this study, such as CT scans and clinical information, were anonymized and maintained with strict confidentiality.

CT scanning

All patients were scanned with a 320-row MDCT scanner (Aquilion ONE, Canon Medical Systems, Otawara, Tochigi, Japan) for both conventional (static) and dynamic-ventilatory scans. The detailed information regarding the CT scanning is described in the [Supplementary material](#).

Image analysis – lung density measurement on dynamic-ventilation CT

Using commercially available software (Lung Volume Measurement, Canon Medical Systems), the mean lung density (MLD) of the scanned lung (< 160 mm in the Z-axis) was measured automatically in each frame. On the time curve of MLD, the peak inspiratory frame (= first expiratory frame) was defined as the lowest MLD on the curve. The expiratory phase was defined as the frames starting from the peak inspiratory frame (first expiratory frame), and the MLD values for the first to fifth expiratory frames were obtained for this study.

Image analysis – strain measurement on dynamic-ventilation CT

Strain measurement on the dynamic-ventilation CT was performed using in-house research software installed in a commercially available workstation for 4D-CT analysis (PhyZiodynamics, Ziosoft, Tokyo, Japan). In brief, the software measured the “maximum principal strain” values (Figure 1), which were originally used in cardiac imaging

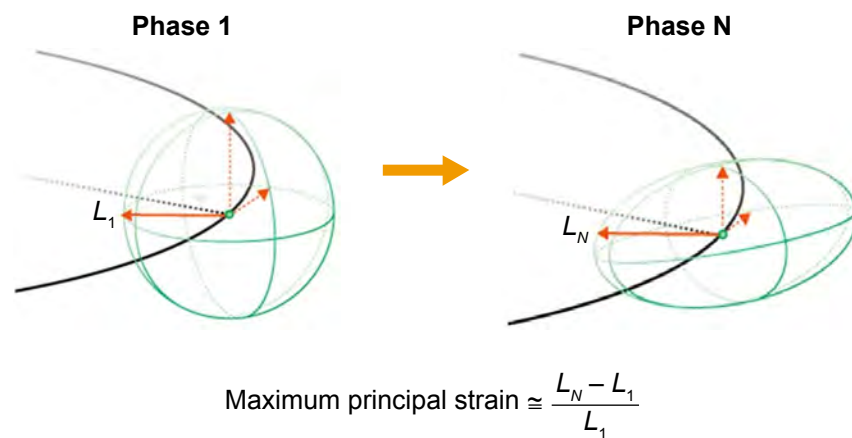


Figure 1 Illustrations for the concept of “principal strain”.

Notes: The maximum principal strain is calculated based on expansion of the principal direction (L) from the starting (standard) point (phase 1) to the measured point (phase N). L_N at phase N becomes large when the original sphere changes its shape strongly at phase N.

but newly modified to assess lung motion. Using the motion coherence algorithm, dynamic-ventilation CT data could be analyzed at any given point in the imaging space using image matching and model matching algorithms that produce the matrix of the motion vectors. Maximum principal strain was calculated directly at the composition/interpolation stage, based on the motion vector at any point in the space. The maximum principal strain was calculated at the points in the space during ventilation, based on expansion of the principal direction from the starting (standard) frame (first expiratory frame = peak inspiratory frame) to the second to fifth expiratory frames. Figure 2 shows an example of a serial change in the maximum principal strain in each frame of the

expiratory phase. The software automatically excluded the upper and lower marginal zones that were not included in the scanning field during inspiration, even if they were included during expiration.

Strain values for the second to fifth expiratory frames were divided by the changes in MLD between the first and second to fifth frames to adjust each strain value by the degree of expiration. Finally, adjusted strain values for the second to fifth frames were summed to express the total strain measurement during expiration. The sum of the adjusted strain values could be considered to express abnormal deformation of lung motion, which was discriminated from physiologic deformation in lung areas with normal exhalation.

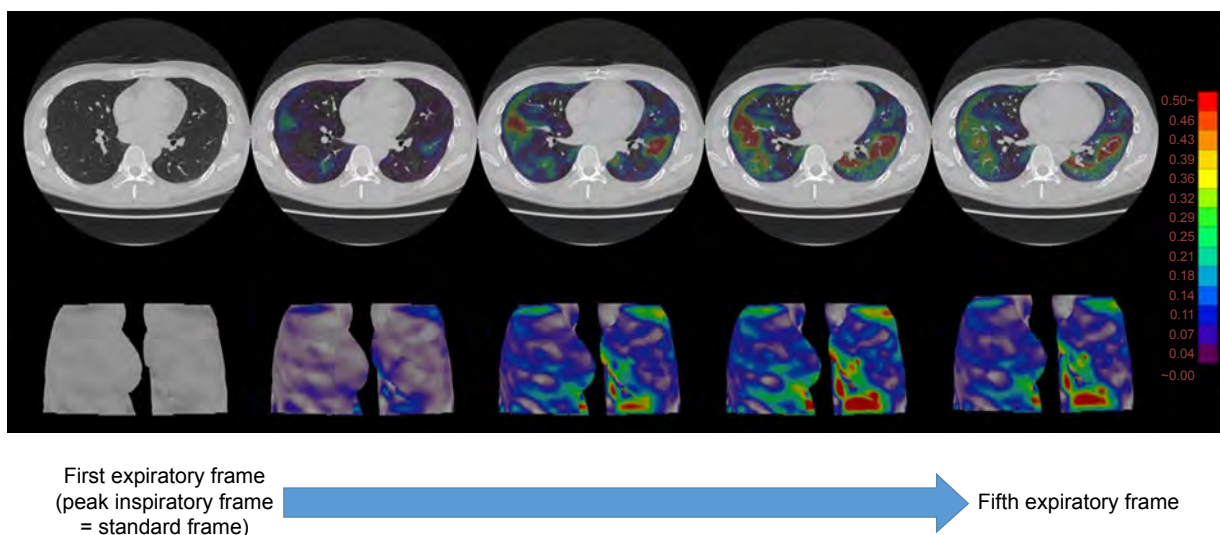


Figure 2 Example of serial changes in strain maps in a patient with COPD.

Note: From the first expiratory frame (left, the peak inspiratory frame) to the fifth expiratory frame, high strain values are observed as red areas, which are different from the gravity-dependent dorsal areas.

Table 1 Clinical characteristics of 32 subjects

Characteristics	Mean ± SD	(Range)
Gender (female:male)	(4:28)	–
Age (years)	70±12	(36–84)
Smoking index (pack-years)	46±21	(2–100)
Smoking status (ex-smoker: current smoker)	(16:16)	–
FEV ₁ (L)	2.20±0.93	(0.54–4.07)
FEV ₁ /FVC	0.73±0.12	(0.41–0.92)
MMFR (L/s)	1.84±1.21	(0.28–4.97)
PEF (L)	5.23±2.67	(1.35–10.5)

Abbreviations: MMFR, maximum mid-expiratory flow rate; PEF, peak expiratory flow.

Image analysis – emphysema measurement by conventional chest CT

Based on the data of the helical CT scans, an emphysema measurement was performed using the same software for the MLD measurement (Lung Volume Measurement, Canon Medical Systems). The percent low attenuation volume (LAV%, < -950 Hounsfield units [HU]) of the whole lung was automatically measured.

Spirometry

All subjects performed spirometry, including FEV₁ and FVC, maximum mid-expiratory flow rate (MMFR), and peak expiratory flow (PEF), according to American Thoracic Society standards.²¹ The spirometric values from the study participants are shown in Table 1. Spirometry was performed within 2 weeks of the chest CT.

Statistical analysis

Data are expressed as mean ± SD. Spearman’s rank correlation analysis was used to evaluate the associations among

the CT indices or between the CT indices and the spirometric values. A *P*-value of <0.05 was considered significant. All statistical analyses were performed using JMP 12.0 software (SAS Institute Inc., Cary, NC, USA).

Results

MLD measurement on dynamic-ventilation CT and emphysema index on conventional CT

Based on dynamic-ventilation CT, the mean MLD values were -871.0±37.3 and -821.5±55.8 HU for the first and fifth expiratory frames, respectively. The MLD values for the first and fifth expiratory frame demonstrated positive correlations with all spirometric values; the MLD at the fifth expiratory frame demonstrated a stronger correlation with FEV₁/FVC ($\rho=0.75$, $P<0.0001$) compared to the MLD at the first expiratory frame (Table 2). Based on helical CT for the whole lung, the mean LAV% (emphysema index) was 10.8%±14.8% and correlated with multiple spirometric values except for FEV₁ (Table 2).

Strain measurement on dynamic-ventilation CT

The mean adjusted strain for expiration was 24.7±18.0 (range, 5.9–72.6). Generally, higher strain values were observed in patients with lower spirometric values, and negative correlations were found between strain and all spirometric values ($\rho=-0.48$ to -0.59 , $P<0.01$) (Table 2) (Figures 3 and 4, [Movies S1](#) and [S2](#)). This implies that homogeneous lung motion would be limited and lost in patients with more severe COPD. Particularly, the correlation coefficient between adjusted strain and the maximum mid-expiratory

Table 2 Correlations between CT measurements and spirometric values

CT measurement	Mean ± SD (range)	Correlation coefficients (ρ)			
		FEV ₁	FEV ₁ /FVC	MMFR	PEF
Dynamic-ventilation CT					
MLD at the first expiratory frame	-871.0±37.3 (-949.6 to -812.9)	0.45 ($P<0.01$)	0.59 ($P<0.001$)	0.57 ($P<0.001$)	0.53 ($P<0.01$)
MLD at the fifth expiratory frame	-821.5±55.8 (-938.7 to -729.8)	0.48 ($P<0.01$)	0.75 ($P<0.0001$)	0.67 ($P<0.001$)	0.57 ($P<0.001$)
Adjusted strain measurement	24.7±18.0 (5.9 to 72.6)	-0.55 ($P<0.01$)	-0.52 ($P<0.01$)	-0.59 ($P<0.001$)	-0.48 ($P<0.01$)
Helical CT					
LAV%	10.8±14.8 (0 to 52.0)	-0.33 (NS)	-0.73 ($P<0.0001$)	-0.57 ($P<0.001$)	-0.38 ($P<0.05$)

Note: The first expiratory frame is the same as the peak inspiratory frame.

Abbreviations: LAV%, percent low attenuation volume (< -950 Hounsfield units); MLD, mean lung density; MMFR, maximum mid-expiratory flow rate; NS, not significant; PEF, peak expiratory flow.

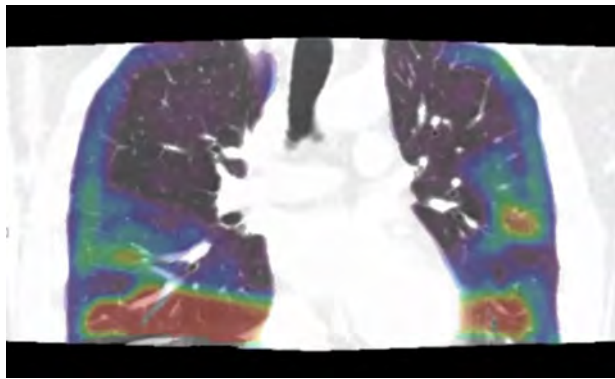


Figure 3 Strain mapping of a non-COPD smoker (during expiration, 39-year-old male, $FEV_1/FVC = 0.92$).

Note: During expiration, high strain values (red areas) are observed just above the diaphragm and around interlobar fissures, suggesting that deformation of the lung would be physiologic due to normal expiration.

airflow was slightly higher ($\rho = -0.59$, $P < 0.001$) than those with other spirometric values.

Discussion

In this study, we applied quantitative strain measurement to 4D dynamic-ventilation CT images and found the following: 1) the strain measurement adjusted by the degree of expiration can be used for assessment of abnormal lung deformation during ventilation and 2) the adjusted strain measurement demonstrates negative correlations with several spirometric values. These observations suggest that abnormal pulmonary deformation by ventilation can be expressed by abnormally high strain values, and strain analysis can provide quantitative information that may reflect uneven, heterogeneous lung movement in various pulmonary and airway diseases. We currently believe that early heterogeneous changes in lung motion can be detected by abnormally high strain values

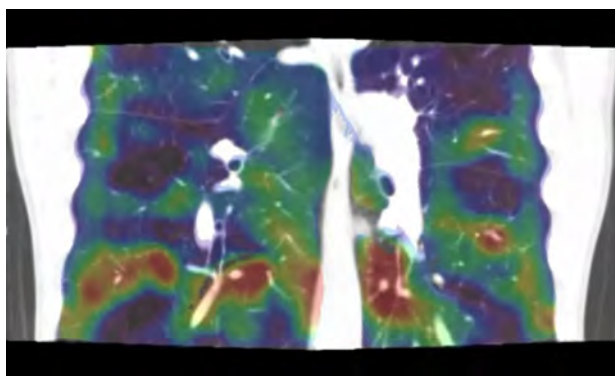


Figure 4 Strain mapping of a severe COPD patient (during expiration, 70-year-old male, $FEV_1/FVC = 0.41$).

Note: Compared with a non-COPD smoker (Figure 3), high strain areas (red areas) are scattered in the lungs, suggesting that these deformations are abnormal and caused by COPD.

in patients with various diseases, such as bronchiectasis, non-tuberculosis mycobacteria, and interstitial lung diseases, which may precede clinical symptoms or abnormalities found by other conventional lung function tests.

Strain measurement has been widely used in cardiology for describing multidimensional deformations or underlying structural changes of muscular fibers, observed by various modalities (such as MRI, CT, and echocardiography).¹⁻¹³ Generally, as the normal myocardium contracts in systole and expands in diastole, high strain values are observed in the normal parts of the heart. In contrast to the normal myocardium, ischemic myocardium or scarred cardiac segments do not contract as well, causing heterogeneous deformation and abnormally low strain values.²² In addition, tethering effects of segments adjacent to area of myocardial infarction also cause an abnormal deformation pattern.^{23,24} Thus, quantitative strain measurement can be used to detect regional myocardial dysfunction in patients with ischemic heart disease, cardiomyopathies, hypertension, and valvular disease.²⁵ Furthermore, strain analysis has been explored to evaluate heterogeneity of myocardial contractile function in patients with dilated cardiomyopathy. Three-dimensional color contour maps based on strain values using MRI accurately visualize heterogeneous contraction in patients with dilated cardiomyopathy.⁵ In other words, in the field of cardiology, strain measurement should be “uniformly high” throughout the myocardium and reduced or heterogeneous strain values imply underlying myocardial dysfunction by various diseases.²⁶

In the current study, we attempted to introduce strain measurement to 4D dynamic-ventilation CT during free breathing. As strain values express deformation of targeted structures, we expected that two different types of deformation must have existed in the lung: normal deformation of the lung due to inhalation/exhalation and abnormal regional deformation caused by heterogeneous ventilation due to COPD (emphysema and airway disease). Normal deformation of the lung would appear at lung areas with large respiratory movements, such as the lung bottom adjacent to the diaphragm and the dorsal part of the lung in the supine position (Figure 3). In contrast, abnormal deformation may be observed throughout the lung without any specific locations, because this abnormal deformation is caused by heterogeneous ventilation or partial air-trapping due to emphysema and airway disease of COPD (Figure 4). To distinguish these two different deformation patterns, we adjusted measured strain values by the degree of expiration in this study. The changes in MLD between the first and the second to fifth respiratory frames indicate the

magnitude of exhalation during the expiratory phase. Even if large deformation occurs by deep (sufficient) expiration in a relatively healthy subject, the high strain values are adjusted by large changes in MLD. In contrast, the value of strain itself may be intermediate in patients with severe COPD without large expiratory movements, but the adjusted strain value may be quite large because of small changes in MLD (insufficient expiration) due to limited airflow. Using this method, we successfully extracted “abnormal” deformation of the lung, which was expressed as the adjusted strain value, and this should be closely associated with heterogeneous lung movements.

The mechanical properties of the lung tissue are mainly determined by collagen and elastic fibers, demonstrating viscoelastic behavior during deflation and inflation.¹⁵ Normally, the stresses under constant ventilation are homogeneously transmitted throughout the entire lung.²⁷ However, in COPD patients, in addition to loss of pulmonary elastic recoil, heterogeneous distribution of pulmonary emphysema and abnormalities of thoracic structures (such as narrowed/collapsed airways and the flattened diaphragm) must result in asynchronous transmission of physical stress in the lung during ventilation, which causes heterogeneous pulmonary movement. Although heterogeneity or asynchrony of lung/airway motion has been reported in COPD patients,^{17–20} this is the first study to quantitatively assess abnormal deformation in the entire scanned lung using strain measurement.

Interestingly, in the current study, adjusted strain was negatively correlated with FEV₁, FEV₁/FVC, MMFR, and PEF. Although the strength of the correlations was intermediate, these correlations suggest that pulmonary motion heterogeneity may be caused by various patterns, such as proximal airway disease, small airway disease, and lung parenchymal abnormalities. Thus, it should be possible to expand strain measurement by dynamic-ventilation CT to other lung/airway diseases, such as asthma, cystic fibrosis, or even diffuse lung disease, which have not been a target of quantitative motion analysis of the lung and airways. Currently, several different approaches have been described using novel CT techniques to measure respiratory changes in lung volume and the emphysema index. These new approaches, including our approach of dynamic-ventilation CT, should generate new information on the pathophysiology of various lung diseases.²⁸

There were several limitations of the present study. First, a limited number of subjects were enrolled. These preliminary results should be reproduced with a larger cohort. Second, MLD and adjusted strain were calculated from part of the lung on 4D dynamic-ventilation CT due to the limited scan length in the Z-axis

(≤160 mm). Thus, selection bias of the lung location would have influenced the strain measurements. Third, the adjusted strain measurements were extracted from the expiratory phase only. As it is known that CT indices at the expiratory phase show higher correlations than at the inspiratory phase,²⁹ we focused on the expiratory phase only. However, strain measurements during inspiration may provide additional insight into pulmonary physiology, and these measurements should be performed in future studies. Fourth, several patients enrolled in the current study had resectable thoracic neoplasms. Although no patient had a large mass invading the chest wall or proximal airways, the presence of thoracic tumor may have influenced the strain measurement. Fifth, other coexisting diseases caused by smoking, such as chronic bronchitis or slight interstitial changes, may have influenced the strain measurement. Ideally, healthy subjects without a smoking history should have been enrolled as a control group to assess the normal respiratory deformation of the lung.

In conclusion, strain analysis using 4D dynamic-ventilation CT is feasible to quantify the abnormal deformation of lung motion in patients with COPD. This technique can be expanded to various lung and airways diseases, in a manner that is similar to cardiac imaging.

Acknowledgments

The authors greatly thank Mr Shun Muramatsu (Ohara General Hospital) for his great help in scanning patients. The authors also thank Dr Shinsuke Tsukagoshi (Canon Medical Systems) and Mr Yasuhiro Kondo (Ziosoft) for their technical support. The ACTive Study Group currently consists of the following institutions: Ohara General Hospital, Fukushima City, Fukushima, Japan (Kotaro Sakuma, MD, Hiroshi Moriya, MD, PhD); Saitama International Medical Center, Saitama Medical University, Hidaka, Saitama, Japan (Fumikazu Sakai, MD, PhD); Kanagawa Cardiovascular and Respiratory Center, Yokohama, Kanagawa, Japan (Tae Iwasawa, MD, PhD); Shiga University of Medical Science, Otsu, Shiga, Japan (Yukihiro Nagatani, MD, Norihisa Nitta, MD, Kiyoshi Murata, MD); Osaka University, Suita, Osaka, Japan (Masahiro Yanagawa, MD, PhD, Osamu Honda, MD, PhD, Noriyuki Tomiyama, MD, PhD); Osaka Medical College, Takatsuki, Osaka, Japan (Mitsuhiro Koyama, MD, PhD); Tenri Hospital, Tenri, Nara, Japan (Yuko Nishimoto, MD, Satoshi Noma, MD, PhD); Kobe University, Kobe, Hyogo, Japan (Yoshiharu Ohno, MD, PhD); University of Occupational and Environmental Health, Kitakyushu, Fukuoka, Japan (Takatoshi Aoki, MD, PhD); University of the Ryukyus, Nishihara, Okinawa, Japan (Tsuneo Yamashiro, MD, Maho Tsubakimoto, MD, PhD, Yanyan Xu, MD,

Sadayuki Murayama, MD, PhD). University of the Ryukyus, Ohara General Hospital, and Shiga University of Medical Science receive a research grant from Canon Medical Systems (formerly Toshiba Medical Systems). University of the Ryukyus also receives a research grant from Ziosoft. Xu Y receives a scholarship (Sasagawa scholarship) from the Japan China Medical Association. Yamashiro T received a research grant from the Japan Society for the Promotion of Science (Kakenhi-16K19837).

Disclosure

The authors report no conflicts of interest in this work.

References

- Pedrizetti G, Sengupta S, Caracciolo G, et al. Three-dimensional principal strain analysis for characterizing subclinical changes in left ventricular function. *J Am Soc Echocardiogr*. 2014;27(10):1041–1050.
- Mor-Avi V, Lang RM, Badano LP, et al. Current and evolving echocardiographic techniques for the quantitative evaluation of cardiac mechanics: ASE/EAE consensus statement on methodology and indications endorsed by the Japanese Society of Echocardiography. *J Am Soc Echocardiogr*. 2011;24(3):277–313.
- Stefani L, De Luca A, Toncelli L, Pedrizetti G, Galanti G. 3D strain helps relating LV function to LV and structure in athletes. *Cardiovasc Ultrasound*. 2014;12(1):33.
- Tanabe Y, Kido T, Kurata A, et al. Three-dimensional maximum principal strain using cardiac computed tomography for identification of myocardial infarction. *Eur Radiol*. 2017;27(4):1667–1675.
- Joseph S, Moazami N, Cupps BP, et al. Magnetic resonance imaging-based multiparametric systolic strain analysis and regional contractile heterogeneity in patients with dilated cardiomyopathy. *J Heart Lung Transplant*. 2009;28(4):388–394.
- McComb C, Carrick D, McClure JD, et al. Assessment of the relationships between myocardial contractility and infarct tissue revealed by serial magnetic resonance imaging in patients with acute myocardial infarction. *Int J Cardiovasc Imaging*. 2015;31(6):1201–1209.
- Buckert D, Tibi R, Cieslik M, et al. Myocardial strain characteristics and outcomes after transcatheter aortic valve replacement. *Cardiol J*. 2018;25(2):203–212.
- Di Franco A, Kim J, Rodriguez-Diego S, et al. Multiplanar strain quantification for assessment of right ventricular dysfunction and non-ischemic fibrosis among patients with ischemic mitral regurgitation. *PLoS One*. 2017;12(9):e0185657.
- Helle-Valle TM, Yu WC, Fernandes VR, Rosen BD, Lima JA. Usefulness of radial strain mapping by multidetector computer tomography to quantify regional myocardial function in patients with healed myocardial infarction. *Am J Cardiol*. 2010;106(4):483–491.
- Miyagi H, Nagata M, Kitagawa K, et al. Quantitative assessment of myocardial strain with displacement encoding with stimulated echoes MRI in patients with coronary artery disease. *Int J Cardiovasc Imaging*. 2013;29(8):1779–1786.
- Maret E, Liehl M, Brudin L, Todt T, Edvardsen T, Engvall JE. Phase analysis detects heterogeneity of myocardial deformation on cine MRI. *Scand Cardiovasc J*. 2015;49(3):149–158.
- Simpson RM, Keegan J, Firmin DN. MR assessment of regional myocardial mechanics. *J Magn Reson Imaging*. 2013;37(3):576–599.
- Jiang K, Yu X. Quantification of regional myocardial wall motion by cardiovascular magnetic resonance. *Quant Imaging Med Surg*. 2014;4(5):345–357.
- Lai-Fook SJ. Lung parenchyma described as a prestressed compressible material. *J Biomech*. 1977;10(5–6):357–365.
- Faffe DS, Zin WA. Lung parenchymal mechanics in health and disease. *Physiol Rev*. 2009;89(3):759–775.
- Sciurba FC, Rogers RM, Keenan RJ, et al. Improvement in pulmonary function and elastic recoil after lung-reduction surgery for diffuse emphysema. *N Engl J Med*. 1996;334(17):1095–1099.
- Stahr CS, Samarage CR, Donnelley M, et al. Quantification of heterogeneity in lung disease with image-based pulmonary function testing. *Sci Rep*. 2016;6(1):29438.
- Estrada L, Torres A, Sarlabous L, et al. Estimation of bilateral asynchrony between diaphragm mechanomyographic signals in patients with chronic obstructive pulmonary disease. *Conf Proc IEEE Eng Med Biol Soc*. 2014;2014:3813–3816.
- Yamashiro T, Moriya H, Tsubakimoto M, Matsuoka S, Murayama S. Continuous quantitative measurement of the proximal airway dimensions and lung density on four-dimensional dynamic-ventilation CT in smokers. *Int J Chron Obstruct Pulmon Dis*. 2016;11(1):755–764.
- Yamashiro T, Moriya H, Matsuoka S, et al. Asynchrony in respiratory movements between the pulmonary lobes in patients with COPD: continuous measurement of lung density by 4-dimensional dynamic-ventilation CT. *Int J Chron Obstruct Pulmon Dis*. 2017;12(1):2101–2109.
- Vestbo J, Hurd SS, Agustí AG, et al. Global strategy for the diagnosis, management, and prevention of chronic obstructive pulmonary disease: GOLD executive summary. *Am J Respir Crit Care Med*. 2013;187(4):347–365.
- Haugaa KH, Smedsrud MK, Steen T, et al. Mechanical dispersion assessed by myocardial strain in patients after myocardial infarction for risk prediction of ventricular arrhythmia. *JACC Cardiovasc Imaging*. 2010;3(3):247–256.
- Edvardsen T, Gerber BL, Garot J, Bluemke DA, Lima JA, Smiseth OA. Quantitative assessment of intrinsic regional myocardial deformation by Doppler strain rate echocardiography in humans: validation against three-dimensional tagged magnetic resonance imaging. *Circulation*. 2002;106(1):50–56.
- Force T, Kemper A, Perkins L, Gilfoil M, Cohen C, Parisi AF. Overestimation of infarct size by quantitative two-dimensional echocardiography: the role of tethering and of analytic procedures. *Circulation*. 1986;73(6):1360–1368.
- Jeung MY, Germain P, Croisille P, El ghannudi S, Roy C, Gangi A. Myocardial tagging with MR imaging: overview of normal and pathologic findings. *Radiographics*. 2012;32(5):1381–1398.
- Nagao M, Yamasaki Y, Yonezawa M, et al. Geometrical characteristics of left ventricular dyssynchrony in advanced heart failure. Myocardial strain analysis by tagged MRI. *Int Heart J*. 2014;55(6):512–518.
- Cai J, Altes TA, Miller GW, et al. MR grid-tagging using hyperpolarized helium-3 for regional quantitative assessment of pulmonary biomechanics and ventilation. *Magn Reson Med*. 2007;58(2):373–380.
- Ley-Zaporozhan J, Ley S, Mews J, Weinheimer O, Kandel S, Rogalla P. Changes of emphysema parameters over the respiratory cycle during free breathing: preliminary results using respiratory gated 4D-CT. *COPD*. 2017;14(6):597–602.
- Yamashiro T, Matsuoka S, Bartholmai BJ, et al. Collapsibility of lung volume by paired inspiratory and expiratory CT scans: correlations with lung function and mean lung density. *Acad Radiol*. 2010;17(4):489–495.

International Journal of COPD**Dovepress****Publish your work in this journal**

The International Journal of COPD is an international, peer-reviewed journal of therapeutics and pharmacology focusing on concise rapid reporting of clinical studies and reviews in COPD. Special focus is given to the pathophysiological processes underlying the disease, intervention programs, patient focused education, and self management protocols.

This journal is indexed on PubMed Central, MedLine and CAS. The manuscript management system is completely online and includes a very quick and fair peer-review system, which is all easy to use. Visit <http://www.dovepress.com/testimonials.php> to read real quotes from published authors.

Submit your manuscript here: <http://www.dovepress.com/international-journal-of-chronic-obstructive-pulmonary-disease-journal>

Correlation Between Intravoxel Incoherent Motion and Dynamic Contrast-Enhanced Magnetic Resonance Imaging Parameters in Rectal Cancer

Hongliang Sun, MD, Yanyan Xu, MD, Qiaoyu Xu, MD, Jianghui Duan, MD, Haibo Zhang, MD, Tongxi Liu, MD, Lu Li, MD, Queenie Chan, PhD, Sheng Xie, MD, Wu Wang, MD

Abbreviations

D	Diffusion coefficient
D*	Pseudo-diffusion coefficient
DCE-MRI	dynamic contrast-enhanced magnetic resonance imaging
DWI	Diffusion-weighted imaging
f	Perfusion fraction
FFE	fast field echo
IVIM	Intravoxel incoherent motion
K^{trans}	transfer constant between blood plasma and extravascular extracellular space

Rationale and Objectives: This study aimed to determine the correlation between intravoxel incoherent motion (IVIM) and multiphase dynamic contrast-enhanced magnetic resonance imaging (DCE-MRI) quantitative parameters in patients with rectal cancer.

Materials and Methods: Ninety-seven patients with rectal cancer were included in this study. All pelvic MRI examinations were performed in a 3.0 T MR unit, including diffusion-weighted imaging with 16 b values, DCE-MRI with two different flip angles (5° and 10° , respectively), and T1-fast field echo sequences as the reference. The IVIM perfusion-related parameters (f , perfusion fraction; D^* , pseudo-diffusion coefficient; $f \cdot D^*$, the multiplication of the two parameters) were calculated by biexponential analysis. Quantitative DCE-MRI parameters were transfer constant (K^{trans}) between blood plasma and extravascular extracellular space), K_{ep} (rate between extravascular extracellular space and blood plasma), V_e (extravascular volume fraction), V_p (plasma volume fraction), and area under the gadolinium concentration curve. Interobserver agreements were evaluated using the intraclass correlation coefficient and Bland–Altman analysis. A p value <0.05 indicated a statistically significant difference.

Results: The study included 75 males and 22 females with a median age of 58.8 years (range, 26–85years). Interobserver reproducibility for IVIM perfusion-related parameters and DCE-MRI quantitative parameters was good to excellent (intraclass correlation coefficient = 0.8618–0.9181, intraclass correlation coefficient = 0.7826–0.9088, respectively). Moderate correlations were found between $f \cdot D^*$ and K^{trans} ($r = 0.533$; $p < 0.001$), and relatively weak correlations between D^* and K^{trans} ($r = 0.389$; $p < 0.001$), D^* and V_p ($r = 0.442$; $p < 0.001$), $f \cdot D^*$ and V_p ($r = 0.466$; $p < 0.001$), and f and V_p ($r = -0.234$; $p = 0.021$).

Acad Radiol 2018; ■:1–7

Reprint requests: No.

Grant Support: This work was supported by grants from Beijing Municipal Science & Technology Commission (No. Z181100001718099), the National Natural Science Foundation of China (No. 81501469) and the Health Industry Special Scientific Research Project of National Health and Family Planning Commission of the People's Republic of China (No. 201402019).

From the Department of Radiology, China-Japan Friendship Hospital, No.2 Yinghua East Street, Chaoyang District, Beijing 100029, China (H.S., Y.X., Q.X., J.D., H.Z., T.L., L.L., S.X., W.W.); Philips Healthcare, Shatin, New Territories, Hong Kong, China (Q.C.). Received May 22, 2018; revised August 24, 2018; accepted August 24, 2018. **Address correspondence to:** H.S. e-mail: stentorsun@gmail.com

© 2018 The Association of University Radiologists. Published by Elsevier Inc. All rights reserved.

<https://doi.org/10.1016/j.acra.2018.08.012>

K_{ep}
rate between EES and blood
plasma

ROI
Region of interest

TE
Echo time

TR
Repetition time

TSE
Turbo spin echo

V_e
extravascular volume fraction

V_p
plasma volume fraction

Conclusion: IVIM perfusion-related parameters, especially $f \cdot D^*$, demonstrated moderate correlations with DCE-MRI quantitative parameters in rectal cancer.

Key Words: Rectal cancer; intravoxel incoherent motion; dynamic contrast-enhanced; magnetic resonance imaging.

© 2018 The Association of University Radiologists. Published by Elsevier Inc. All rights reserved.

INTRODUCTION

Tumor angiogenesis plays a vital role in tumor growth and progressively invasion, and evaluation of tumor angiogenesis activity is quite helpful for diagnosis, prognostic evaluation, and therapeutic monitoring of rectal cancer (1–2). T1-weighted dynamic contrast-enhanced magnetic resonance imaging (DCE-MRI) is a well-established technique used to map quantitative perfusion and permeability parameters, which indirectly reflect tumor microcirculation. It has been proved that perfusion parameters of DCE-MRI correlated with tumor angiogenesis and molecular markers in rectal cancer (3–7). Previous clinical studies (8–10) also demonstrated the potential value of DCE-MRI in monitoring treatment response of rectal cancer to neoadjuvant chemoradiation. However, DCE-MRI could not provide perfusion information without the injection of intravenous contrast media, which was a dilemma, particularly in patients with renal insufficiency or individuals with severe allergies to intravenous gadolinium-based contrast media.

Intravoxel incoherent motion diffusion-weighted imaging (IVIM-DWI) (11) is another attractive functional MRI technique that provides parameters reflecting tissue perfusion without intravenous contrast injection. IVIM-DWI consists of a series of diffusion-weighted acquisitions with a wide range of b values, subsequently, allowing for simultaneous acquisition of both microcirculatory and diffusivity information. Furthermore, Le Bihan and Turner (12,13) provided the equations that linked perfusion-related IVIM parameters and conventional perfusion parameters in the brain, stating that theoretical relationships existed between f and blood volume, D^* and mean transit time, and flow-related parameters and blood flow. Therefore, IVIM perfusion-related parameters were assumed to be theoretically associated with DCE-MRI parameters. If perfusion information of rectal cancer can be evaluated using IVIM-DWI, then IVIM-DWI may possibly serve as a surrogate for DCE-MRI to some degree, eventually bringing down the need for contrast agent injection.

Although the potential ability of IVIM-DWI parameters in probing tumor microcirculation is fascinating, no clear relationships between perfusion-related IVIM parameters and DCE-MRI quantitative parameters in rectal cancers have been reported.

Therefore, this study aimed to evaluate the relationship between perfusion-related IVIM parameters and DCE-MRI quantitative parameters in patients with rectal cancer, and to explore the possibility of noninvasively evaluating tumor perfusion using DWI in the future.

MATERIALS AND METHOD

Patients

This retrospective study was approved by the ethics committee of the hospital, and written informed consent was obtained in all cases.

Totally, 152 consecutive patients with biopsy-proven rectal cancers, waiting to undergo initial staging investigations, were recruited. After imaging examinations (including MRI), although surgery was performed in all patients, the other therapy procedures including chemoradiation therapy were individually tailored.

However, patients who met any of the following criteria were excluded from the late evaluation: (1) prior rectal surgery (rectal cancer resection [$n = 2$], polypectomy [$n = 1$], anal fistulectomy [$n = 1$], and rectal prolapse surgery [$n = 1$]); (2) pre-examination chemoradiation therapy ($n = 20$) or unidentified herbal medicine therapy ($n = 7$); (3) poor image quality (heavy intestinal peristalsis or heavy susceptibility artifacts [$n = 5$], too small lesion [diameter < 5 mm], or difficult to identify on images [$n = 6$]); and (4) mucinous adenocarcinoma ($n = 12$). Finally, 97 patients (75 men and 22 women; mean age, 58.8 years; age range, 26–85 years) were enrolled in the final analysis. Selected patient and tumor characteristics are shown in Table 1.

MRI Examination

Patients had low-residue diet before examination and fasted on the day of examination. Intramuscular injection of 10 mg

TABLE 1. Patient and Tumor Characteristics

Characteristic	No.
Patient number	97
Age (year)	
Mean (range)	58.8 (26–85)
Sex (M/F)	75/22
Tumor length (cm)	4.06 ± 1.75
Radiologic T stage	
T1–2	30 (30.93%)
T3	55 (56.70%)
T4	12 (12.37%)
Tumor location (distance from the anal verge)	
Upper (>10 cm)	15 (15.46%)
Middle (5–10 cm)	40 (41.24%)
Lower (<5 cm)	42 (43.30%)

anisodamine hydrochloride was given to each patient to inhibit intestinal peristalsis. The patients had to lie on the table without moving to minimize the possible motion artifacts or deformation introduced during the examination.

Pelvic MRI scanning was implemented on a 3T whole-body scanner (Ingenia, Philips Medical Systems, Best, the Netherlands) with a gradient strength 45 mT/m and a gradient switching rate 200 mT/(m·ms), using a 16-channel anterior torso dS coil and a 16-channel posterior table dS coil. 2D Sagittal and coronal T2-weighted turbo spin echo sequences were performed with the following parameters: repetition time (TR) 4347 ms, echo time (TE) 102 ms, Echo-train length 21, field of view (FOV) 24 × 24 cm², slice thickness 4 mm with 0.4-mm gap, acquisition matrix 336 × 246, and number of signals averaged (NSA) 1. A 2D oblique axial T2-weighted turbo spin echo sequence was planned perpendicularly to the tumor axis using the following parameters: TR 4522 ms, TE 102 ms, FOV 18 × 18 cm², slice thickness 3.5 mm with 0.35-mm gap, and acquisition matrix 300 × 296.

Oblique axial IVIM–MRI scan was performed using a single-shot echo-planar imaging pulse sequence in free breathing with the following parameters: TE/TR 76/4000 ms, FOV 40 × 32 cm², slice thickness 6 mm with 0.6-mm gap, acquisition matrix 160 × 102, echo-planar imaging (EPI) factor 35, bandwidth 3113.1, number of slices 20, fat saturation technique SPectral Attenuated Inversion Recovery and 16 *b* values (0, 10, 20, 30, 40, 60, 80, 100, 150, 200, 400, 800, 1000, 1200, 1500, and 2000 s/mm²). When *b* values were 0, 10, 20, 30, 40, 60, 80, 100, 150, 200, 400 s/mm², the NSA was 1. When *b* value was 800 s/mm², the NSA was 2. When *b* values were 1000, 1200, 1500, and 2000 s/mm², the NSA was 3. The scan time of single IVIM was 5 minutes.

DCE-MRI (40 dynamic phases) used a 3D fast field echo sequence with fat suppression on the oblique axial plane (the same as IVIM–MRI sequence). Two precontrast T1-fast field echo sequences with different flip angles (5° and 10°, respectively) were set as references to calculate the baseline

T1 relaxation time per pixel (baseline T1 map). The two reference series were identical to the DCE sequences in terms of, for example, FOV, orientation, resolution, slice thickness, and number of slices. Scan parameters of DCE-MRI were as follows: TR/TE 1.63/3.3 ms; flip angle 15°; acquisition matrix 252 × 222; FOV 304 × 362 mm²; slice thickness 1.5 mm; and number of slices 70; the temporal resolution 2 seconds. The total scan time of DCE-MRI (40 dynamic phases) was approximately 4.8 minutes.

A gadolinium-based agent gadopentetate dimeglumine (Magnevist; Bayer Healthcare, Berlin, Germany) was intravenously injected at a flow rate of 2.5 ml/s and at a dose of 0.2 ml/kg of body weight, followed by a 20-ml saline flush with a high-pressure injector.

Image Analysis

The IVIM perfusion-related parameters (*f*, perfusion fraction; *D*^{*}, pseudo-diffusion coefficient) and the flow-related parameter (*fD*^{*}) were calculated using the biexponential model described by Le Bihan et al. (11,12) as follows:

$$S_b/S_0 = (1-f) \exp(-bD) + f \exp(-bD^*)$$

where *S_b* is the signal intensity in the pixel with diffusion gradient, *S₀* is the signal intensity in the pixel without diffusion gradient, *D* is the true diffusion as reflected by pure molecular diffusion, *f* is the fractional perfusion related to microcirculation, and *D*^{*} is the pseudo-diffusion coefficient related to perfusion. The raw data of diffusion-weighted images were transferred to an EWS4.1 workstation and analyzed using in-house software (IDL6.3 software, Colorado).

Quantitative DCE-MRI parameters were *K*^{trans} (transfer constant between blood plasma and extravascular extracellular space [EES]), *K*_{ep} (rate between EES and blood plasma), *V*_e (extravascular volume fraction), *V*_p (plasma volume fraction), and AUC (area under the gadolinium concentration curve). The pharmacokinetic calculation was done on a pixel-by-pixel basis using a two-compartment model. The calculation was based on the extended Tofts model (14) as follows:

$$C(t) = V_p C_a(t) + K^{trans} e^{-tK_{ep}} * C_a(t)$$

where *C(t)* is the contrast concentration in tissue and *C_a(t)* is the arterial input function. DCE-MRI data were transferred to an advantage workstation using T1 permeability software (Intellispace portal workstation, Philips Medical Systems).

K^{trans} and DWI images (*b* = 1000 s/mm²) were used as references to determine the lesion areas on corresponding IVIM and DCE maps (Fig 1).

Regions of interest (ROIs) were manually drawn to cover the entire tumor area slice by slice, avoiding the inclusion of intestinal gas, liquid, and anatomical structures. Necrotic and large cystic areas by visual view were excluded from ROI. An ROI of the lesion was manually drawn on the basis of the DWI images (*b* = 1000 s/mm²), and the values of *f* and

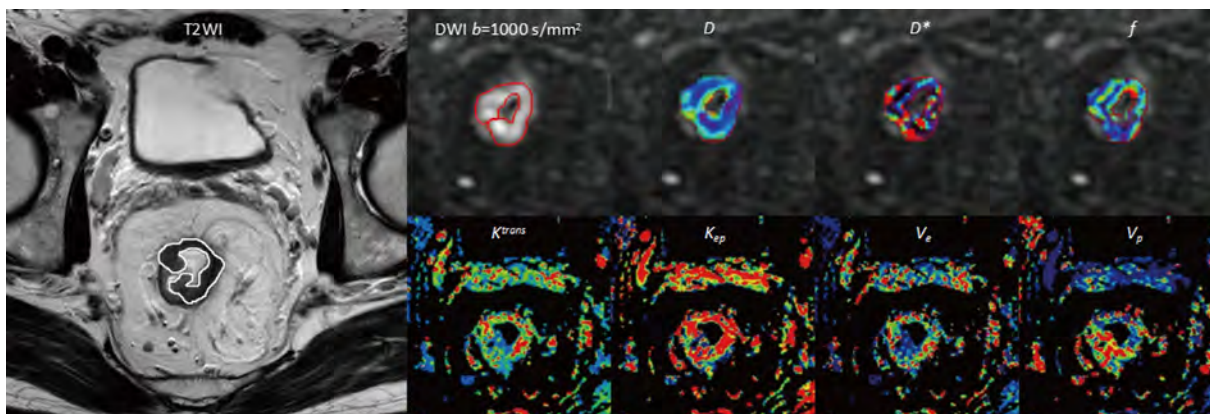


Figure 1. Images in a 53-year-old man with moderately differentiated rectal cancer. The border of the lesion on the T2WI image was manually drawn. The top row small images: DWI ($b = 1000 \text{ s/mm}^2$) and IVIM-DWI parameter images (D , D^* , and f); the bottom row small images: corresponding DCE-MRI quantitative parameter images (K^{trans} , K_{ep} , V_e , and V_p). DCE-MRI, dynamic contrast-enhanced magnetic resonance imaging; DWI, Diffusion-weighted imaging; IVIM-DWI, intravoxel incoherent motion diffusion-weighted imaging.

D^* were obtained automatically for measuring the IVIM parameters. For DCE-MRI measurements, an arterial input function obtained from the iliac artery was applied for modeling procedure. Then, the following maps were obtained automatically: K^{trans} , K_{ep} , V_e , V_p , and AUC. Eventually, an ROI of the lesion was manually drawn on the basis of the K^{trans} map, and the corresponding values of K^{trans} , K_{ep} , V_e , V_p , and AUC were obtained automatically.

Two experienced radiologists (10 and 6 years, respectively, in gastrointestinal imaging) placed the ROIs and analyzed all the IVIM and DCE-MRI images independently. The data generated by the two observers were used to calculate interobserver reliability.

Statistical Analysis

All analyses were performed using statistical software SPSS17.0 (SPSS 17.0 for Windows, SPSS, Illinois). Normality testing was performed using the Shapiro–Wilk test and homogeneity-of-variance testing using the Levene test. Continuous variables were expressed as mean \pm standard

deviation or median \pm interquartile range. Correlations between f and all quantitative DCE-MRI parameters were analyzed using Pearson's or Spearman's correlation coefficients, respectively. D^* and $f \cdot D^*$ were also similarly analyzed. Interobserver reliability was evaluated using the intraclass correlation coefficient (ICC) and Bland–Altman analysis. Correlation coefficient $|r|$ of 0–0.5, 0.5–0.8, and >0.8 was considered as poor, moderate, and high correlations, respectively. A p value <0.05 was considered to indicate a statistically significant difference.

RESULTS

Interobserver Reliability

The measurement consistency between two observers was evaluated by ICC and Bland–Altman analysis (Table 2). ICC and Bland–Altman bias values for IVIM and DCE-MRI quantitative parameters indicated good to excellent interobserver reliability. (ICC_{IVIM}, 0.8618–0.9181, ICC_{DCE}, 0.7826–0.9088; Bias_{IVIM}, 0.5%–2.8%, Bias_{DCE}, –10.4%–5.3%).

TABLE 2. Interobserver Reliability in Assessing IVIM and DCE-MRI Parameters

Parameters	ICC (95% CI)	Bland–Altman Bias (95% CI), %
f	0.9181 (0.8643–0.9554)	0.5 (–39.7 to 40.7)
D^*	0.8618 (0.8334–0.8843)	2.8 (–49.7 to 55.3)
$f \cdot D^*$	0.8817 (0.8540–0.9306)	2.3 (–53.6 to 58.2)
K^{trans}	0.9088 (0.8344–0.9655)	5.1 (–55.2 to 65.4)
K_{ep}	0.8774 (0.8221–0.9163)	5.3 (–62.3 to 72.9)
V_e	0.7826 (0.6749–0.8547)	–10.4 (–140.6 to 119.8)
V_p	0.9021 (0.8571–0.9335)	–1.6 (–52.2 to 49.0)
AUC	0.8445 (0.8181–0.8825)	–2.9 (–33.8 to 28.0)

AUC, area under the gadolinium concentration curve; D^* , pseudo-diffusion coefficient; DCE-MRI, dynamic contrast-enhanced magnetic resonance imaging; f , perfusion fraction; $f \cdot D^*$, the multiplication of the two parameters; ICC, intraclass correlation coefficient; IVIM, intravoxel incoherent motion; K_{ep} , rate between EES and blood plasma; K^{trans} , transfer constant between blood plasma and extravascular extracellular space; V_e , extravascular volume fraction; V_p , plasma volume fraction; 95% CI, 95% confidence interval.

Tissue Perfusion Parameters

The IVIM perfusion parameters were as follows: $f = (17.02 \pm 8.37)\%$, $D^* = (15.83 \pm 55.56) \times 10^{-3} \text{ mm}^2/\text{s}$, $fD^* = (2.04 \pm 5.69) \times 10^{-3} \text{ mm}^2/\text{s}$.

The DCE-MRI quantitative parameters were as follows: $K^{\text{trans}} = (2.00 \pm 4.20) \text{ min}^{-1}$, $K_{\text{ep}} = (0.99 \pm 0.87) \text{ min}^{-1}$, $V_e = 1.76 \pm 3.61$, $V_e = 0.49 \pm 0.88$, and $\text{AUC} = 46.96 \pm 21.29$.

Correlations Between Parameters of IVIM and DCE-MRI

Moderate correlations were found between fD^* and K^{trans} ($r = 0.533$; $p < 0.001$), and relatively weak correlation between D^* and K^{trans} ($r = 0.389$; $p < 0.001$), D^* and V_p ($r = 0.442$; $p < 0.001$), fD^* and V_p ($r = 0.466$; $p < 0.001$), and f and V_p ($r = -0.234$; $p = 0.021$; Table 3).

DISCUSSION

The present study investigated the correlations between IVIM perfusion-related parameters and quantitative DCE-MRI perfusion metrics in rectal cancer to evaluate the ability of IVIM-DWI to measure tumor perfusion. The results showed that fD^* was moderately related to K^{trans} , and relatively weak correlations were also found between D^* and K^{trans} ($r = 0.389$), D^* and V_p ($r = 0.442$), fD^* and V_p ($r = 0.466$), and f and V_p ($r = -0.234$). The findings supported the aforementioned hypothesis that potential relationships existed between IVIM and DCE-MRI perfusion parameters to some degree.

fD^* allowed the estimation of relative perfusion or blood flow in the tumor microcirculation (13), which was thought to depend on the interplay among the microvascular anatomy, vascular permeability, and blood flow dynamics. In contrast, K^{trans} was defined as transfer constant between blood plasma and EES, reflecting vascular permeability when

contrast uptake was limited by vascular endothelial leakiness (15,16). Furthermore, K^{trans} was possibly related to tumor angiogenesis, and higher mean K^{trans} value was observed in epidermal growth factor receptor-positive rectal cancer (3). Therefore, the moderate correlation between fD^* and K^{trans} in this study suggested that fD^* was associated with vascular permeability and blood flow in rectal cancer. Similar results were reported in studies on non-small-cell lung cancer, head and neck squamous cell cancer, breast lesions, and cervical cancers (17–21).

The f value was a measure of the fractional volume of capillary blood flow in each voxel, while D^* was reported to be proportional to blood velocity and mean capillary segment length (11), which were heterogeneous in the tortuous tumor vasculature. Thus, f and D^* indirectly reflected the increased immature vessels and capillary permeability. Furthermore, in an animal study of human colorectal cancer (HT29) implanted mice model, f and D^* were significantly associated with the tumor microvessel density, which was considered as a surrogate marker for angiogenesis (22). Moreover, delivery of the tracer to the tissues was still dependent on intravascular flow even with the use of diffusible tracers (12,13). Thus, a relationship between perfusion parameters quantified by DWI and tracer kinetic methods could plausibly be deduced (13).

However, the aforementioned relationship is still controversial, as evident from the published studies (17–21, 23–26). In the present study, relatively weak correlations were observed between f , D^* , and DCE-MRI parameters, especially f and V_p ($r = -0.234$). Possible reasons for the discrepancy reported in some studies (26,27) and the present study were as follows: (1) the fast component of f and D^* measured by DWI might comprise more than one physiologic process in some organs (eg, glandular secretion, ductal flow, and cerebrospinal fluid flow) (28–30); (2) the evolution time of DWI sequence for significant water exchange was limited and thus the signal could be interpreted as separate intra- and extravascular compartments, with the parameters f and D^* referring to the intravascular compartments. In contrast, DCE-MRI tracked contrast continuously over much longer periods (several minutes) and thus necessarily involved intravascular, extravascular, and exchange dynamics. Thus, the parameters of the DCE-MRI model reflected not only the microvascular volume or flow but also some composite encompassing total tracer transit (24); (3) signal intensity would be affected by different b -value selection, especially low b value ($\leq 200 \text{ s/mm}^2$) (31–32); and (4) non-negligible heterogeneity within an individual tumor (17). Further studies and a more standardized approach to data collection (IVIM-DWI or DCE-MRI sequence) and analysis are needed to verify the conflicting results published in the literature.

In addition, careful consideration should also be given to the interobserver reliability of IVIM and DCE-MRI parameters. Compared to other parameters, relatively larger range of 95% confidence interval limits of agreement in V_e has been

TABLE 3. Correlation Coefficient Between IVIM Perfusion-Related Parameters and Perfusion Measurements From DCE-MRI

Variables	f		fD^*		D^*	
	r	p	R	p	r	p
K^{trans}	0.068	0.506	0.533	<0.001	0.389	<0.001
K_{ep}	0.144	0.768	-0.077	0.452	-0.093	0.641
V_e	0.094	0.358	-0.130	0.658	-0.166	0.773
V_p	-0.234	0.021	0.466	<0.001	0.442	<0.001
AUC	-0.140	0.771	-0.110	0.838	-0.120	0.845

AUC, area under the gadolinium concentration curve; D^* , pseudo-diffusion coefficient; DCE-MRI, dynamic contrast-enhanced magnetic resonance imaging; f , perfusion fraction; fD^* , the multiplication of the two parameters; ICC, intraclass correlation coefficient, IVIM, intravoxel incoherent motion; K_{ep} , rate between EES and blood plasma; K^{trans} , transfer constant between blood plasma and extravascular extracellular space; V_e , extravascular volume fraction; V_p , plasma volume fraction.

observed in this study. V_e is one of the perfusion parameters derived from DCE-MRI data, reflecting the situation in EES, however, it was less consistent (21). The following factors may contribute to large variability in V_e . One factor is tumor angiogenesis, abnormal vessels have been heterogeneously distributed, and the vascular space and EES could be variable (3,4). Furthermore, the high ratio of advanced cancer in subjects (69.07% rectal cancer \geq T3 stage) may intensify the variability in the study. Another possible factor is that V_e can vary with edema around the lesion (33). Therefore, V_e may be less reliable and needs to be further studied.

This study had several limitations. First, only patients with pathologically proven rectal adenocarcinoma were included and evaluated in this study. Second, the optimal b -value selection for rectal cancer was not assessed. Different b -value selection methods affected the IVIM parameter estimates, especially f (34,35). The clinical tolerance and IVIM characterization both were taken into consideration. Further, 16 b values were used in this study, and half of them were less than 200 s/mm². Third, other analysis methods for IVIM estimation, such as nonnegative least squares fitting, were not introduced (36). Fourth, the perfusion parameters derived from IVIM and DCE-MRI were not correlated with the histopathological results (such as the microvascular density). However, the purpose of the present study was not to identify the correlation between MR parameters and histopathology, but the relationship between the MR parameters derived using different techniques.

In conclusion, IVIM-DWI could be performed without the administration of exogenous contrast medium, making it a safer and more convenient method for patients, especially for individuals with renal insufficiency. Furthermore, the present study implied that IVIM perfusion-related parameters, especially $f \cdot D^*$, demonstrated moderate correlations with quantitative perfusion parameters derived from DCE-MRI in rectal cancer. Thus, the rectal IVIM-DWI analysis can provide both diffusion and perfusion information, which has a potential value in evaluating treatment response, differentiating cancer recurrence from radiofibrosis in patients with rectal cancer without exogenous contrast agent.

REFERENCES

- Folkman J. What is the evidence that tumors are angiogenesis dependent? *J Natl Cancer Inst* 1990; 82:4–6.
- Choi HJ, Hyun MS, Jung GJ, et al. Tumor angiogenesis as a prognostic predictor in colorectal carcinoma with special reference to mode of metastasis and recurrence. *Oncology* 1998; 55:575–581.
- Yeo DM, Oh SN, Jung CK, et al. Correlation of dynamic contrast-enhanced MRI perfusion parameters with angiogenesis and biologic aggressiveness of rectal cancer: preliminary results. *J Magn Reson Imaging* 2015; 41:474–480.
- Yao WW, Zhang H, Ding B, et al. Rectal cancer: 3D dynamic contrast-enhanced MRI; correlation with microvascular density and clinicopathological features. *Radiol Med* 2012; 116:366–374.
- Tuncbilek N, Karakas HM, Altaner S. Dynamic MRI in indirect estimation of microvessel density, histologic grade, and prognosis in colorectal adenocarcinomas. *Abdom Imaging* 2004; 29:166–172.
- de Lussanet QG, Backes WH, Griffioen AW, et al. Dynamic contrast-enhanced magnetic resonance imaging of radiation therapy-induced microcirculation changes in rectal cancer. *Int J Radiat Oncol Biol Phys* 2005; 63:1309–1315.
- Zhang XM, Yu D, Zhang HL, et al. 3D dynamic contrast-enhanced MRI of rectal carcinoma at 3T: correlation with microvascular density and vascular endothelial growth factor markers of tumor angiogenesis. *J Magn Reson Imaging* 2008; 27:1309–1316.
- Lim JS, Kim D, Baek SE, et al. Perfusion MRI for the prediction of treatment response after preoperative chemoradiotherapy in locally advanced rectal cancer. *Eur Radiol* 2012; 22:1693–1700.
- Intven M, Reerink O, Philippens ME. Dynamic contrast enhanced MR imaging for rectal cancer response assessment after neo-adjuvant chemoradiation. *J Magn Reson Imaging* 2015; 41:1646–1653.
- Martens MH, Subhani S, Heijnen LA, et al. Can perfusion MRI predict response to preoperative treatment in rectal cancer? *Radiother Oncol* 2015; 114:218–223.
- Le Bihan D, Breton E, Lallemand D, et al. Separation of diffusion and perfusion in intravoxel incoherent motion MR imaging. *Radiology* 1988; 168:497–505.
- Le Bihan D, Breton E, Lallemand D, et al. MR imaging of intravoxel incoherent motions: application to diffusion and perfusion in neurologic disorders. *Radiology*. 1986; 161:401–407.
- Le Bihan D, Turner R. The capillary network: a link between IVIM and classical perfusion. *Magn Reson Med* 1992; 27:171–178.
- Tofts PS, Brix G, Buckley DL, et al. Estimating kinetic parameters from dynamic contrast-enhanced T(1)-weighted MRI of a diffusible tracer: standardized quantities and symbols. *J Magn Reson Imaging* 1999; 10:223–232.
- Zahra MA, Hollingsworth KG, Sala E, et al. Dynamic contrast-enhanced MRI as a predictor of tumour response to radiotherapy. *Lancet Oncol* 2007; 8:63–74.
- Barnes SL, Whisenant JG, Loveless ME, Yankeelov TE. Practical dynamic contrast enhanced MRI in small animal models of cancer: data acquisition, data analysis, and interpretation. *Pharmaceutics* 2012; 4:442–478.
- Shi C, Liu D, Xiao Z, et al. Monitoring tumor response to antivascular therapy using non-contrast intravoxel incoherent motion diffusion-weighted MRI. *Cancer Res* 2017; 77:3491–3501.
- Fujima N, Yoshida D, Sakashita T, et al. Intravoxel incoherent motion diffusion-weighted imaging in head and neck squamous cell carcinoma: assessment of perfusion-related parameters compared to dynamic contrast-enhanced MRI. *Magn Reson Imaging* 2014; 32:1206–1213.
- Lee EY, Hui ES, Chan KK, et al. Relationship between intravoxel incoherent motion diffusion-weighted MRI and dynamic contrast-enhanced MRI in tissue perfusion of cervical cancers. *J Magn Reson Imaging* 2015; 42:454–459.
- Kim JH, Kim CK, Park BK, et al. Dynamic contrast-enhanced 3-T MR imaging in cervical cancer before and after concurrent chemoradiotherapy. *Eur Radiol* 2012; 22:2533–2539.
- Liu C, Wang K, Chan Q, et al. Intravoxel incoherent motion MR imaging for breast lesions: comparison and correlation with pharmacokinetic evaluation from dynamic contrast-enhanced MR imaging. *Eur Radiol* 2016; 26:3888–3898.
- Lee HJ, Rha SY, Chung YE, et al. Tumor perfusion-related parameter of diffusion-weighted magnetic resonance imaging: correlation with histological microvessel density. *Magn Reson Med* 2014; 71:1554–1558.
- Suo S, Lin N, Wang H, et al. Intravoxel incoherent motion diffusion-weighted MR imaging of breast cancer at 3.0 tesla: comparison of different curve-fitting methods. *J Magn Reson Imaging* 2015; 42:362–370.
- Patel J, Sigmund EE, Rusinek H, et al. Diagnosis of cirrhosis with intravoxel incoherent motion diffusion MRI and dynamic contrast-enhanced MRI alone and in combination: preliminary experience. *J Magn Reson Imaging* 2010; 31:589–600.
- Xu XQ, Choi YJ, Sung YS, et al. Intravoxel Incoherent motion MR imaging in the head and neck: correlation with dynamic contrast-enhanced MR imaging and diffusion-weighted imaging. *Korean J Radiol* 2016; 17:641–649.
- Marzi S, Stefanetti L, Sperati F, et al. Relationship between diffusion parameters derived from intravoxel incoherent motion MRI and perfusion measured by dynamic contrast-enhanced MRI of soft tissue tumors. *NMR Biomed* 2016; 29:6–14.
- Guo Z, Zhang Q, Li X, et al. Intravoxel incoherent motion diffusion weighted MR imaging for monitoring the instantly therapeutic efficacy of radiofrequency ablation in rabbit VX2 tumors without evident links between conventional perfusion weighted images. *PLoS One* 2015; 10:e0127964.

28. Kwong KK, McKinstry RC, Chien D, et al. CSF-suppressed quantitative single-shot diffusion imaging. *Magn Reson Med* 1991; 21:157–163.
29. Zhang L, Murata Y, Ishida R, et al. Functional evaluation with intravoxel incoherent motion echo-planar MRI in irradiated salivary glands: a correlative study with salivary gland scintigraphy. *J Magn Reson Imaging* 2001; 14:223–239.
30. Thoeny HC, De Keyzer F, Oyen RH, et al. Diffusion-weighted MR imaging of kidneys in healthy volunteers and patients with parenchymal diseases: initial experience. *Radiology* 2005; 235:911–917.
31. Iima M, Reynaud O, Tsurugizawa T, et al. Characterization of glioma microcirculation and tissue features using intravoxel incoherent motion magnetic resonance imaging in a rat brain model. *Invest Radiol* 2014; 49:485–490.
32. Liu C, Liang C, Liu Z, et al. Intravoxel incoherent motion (IVIM) in evaluation of breast lesions: comparison with conventional DWI. *Eur J Radiol* 2013; 82:e782–e789.
33. Tofts PS. Modeling tracer kinetics in dynamic Gd-DTPA MR imaging. *J Magn Reson Imaging* 1997; 7:91–101.
34. Lemke A, Stieltjes B, Schad LR, et al. Toward an optimal distribution of b values for intravoxel incoherent motion imaging. *Magn Reson Imaging* 2011; 29:766–776.
35. Zhang JL, Sigmund EE, Rusinek H, et al. Optimization of b-value sampling for diffusion-weighted imaging of the kidney. *Magn Reson Med* 2012; 67:89–97.
36. Keil VC, Mädler B, Gielen GH, et al. Intravoxel incoherent motion MRI in the brain: impact of the fitting model on perfusion fraction and lesion differentiability. *J Magn Reson Imaging* 2017; 46:1187–1199.

Relationship between CT activity score with lung function and the serum angiotensin converting enzyme in pulmonary sarcoidosis on chest HRCT

Jianghui Duan, MD^a, Yanyan Xu, MD^a, Haixu Zhu, MD^b, Haibo Zhang, MD^a, Shilong Sun, BS^a, Hongliang Sun, MD^{a,*}, Wu Wang, MD^a, Sheng Xie, MD^a

Abstract

To address the reliability of CT activity score (CTAS) and investigate the relationships between CTAS, lung function changes after treatment and the serum angiotensin-converting enzyme (SACE) levels.

Fifty-seven sarcoidosis patients underwent chest high-resolution CT (HRCT) and spirometry, as well as SACE examination, were retrospectively analyzed. Follow-up spirometry in each patient was obtained about 6 months after the initial spirometry. The correlations between CTAS and pulmonary function changes were evaluated by Spearman correlation analysis. According to SACE status, patients were divided into normal and high level 2 subgroups. Comparisons of pulmonary function parameters, HRCT abnormalities extent scores between SACE normal and high 2 subgroups were performed with the Mann-Whitney *U* test or Independent samples *t* test.

CTAS demonstrated significant correlations with lung function changes ($\Delta\%VC$: $\rho=0.543$, $P<.001$; $\Delta FEV_{1.0}/FVC$: $\rho=0.417$, $P=.001$; $\Delta\%TLC$: $\rho=0.309$, $P=.019$). In addition, worse initial lung function, larger changes of lung function, and higher extent scores of HRCT were observed in SACE high-level subgroup.

The findings of this study suggest that CTAS of initial HRCT is a promising index for disease activity in pulmonary sarcoidosis to some degree. Prospective studies with large cohort designed to address further verification are warranted before wide clinical practice.

Abbreviations: %TLC = total lung capacity as percent of the predicted value, %VC = vital capacity as percent of the predicted value, CTAS = CT activity score, EBUS-TBNA = endobronchial ultrasound-guided transbronchial needle aspiration, FEV_{1.0} = forced expiratory volume in the first second, FVC = forced vital capacity, GGO = ground-glass opacity, HRCT = high-resolution CT, HU = Hounsfield units, IQR = interquartile range, IST = interlobular septal thickening, SACE = serum angiotensin-converting enzyme, TBLB = transbronchial lung biopsy, WASOG = World Association of Sarcoidosis and Other Granulomatous Disorders.

Keywords: disease activity, high-resolution computed tomography, lung function, sarcoidosis, serum angiotensin converting enzyme

1. Introduction

Sarcoidosis is a multisystem granulomatous disorder with unclear etiology and unpredictable course.^[1–3] The clinical course and the prognosis are related to the symptoms at onset

Editor: Eleonore Fröhlich.

This work has received funding from Beijing Municipal Science and Technology Commission No. Z181100001718099, the National Natural Science Foundation of China (81501469), and the Health Industry Special Scientific Research Project of National Health and Family Planning Commission of the People's Republic of China (201402019).

The authors have no conflicts of interest to disclose.

^a Department of Radiology, China-Japan Friendship Hospital, Beijing,

^b Department of Radiology, The People's Hospital of Xinjiang Uyghur Autonomous Region, Urumqi, China.

* Correspondence: Hongliang Sun, Department of Radiology, China-Japan Friendship Hospital, Beijing 100029, China (e-mail: stentorsun@gmail.com).

Copyright © 2018 the Author(s). Published by Wolters Kluwer Health, Inc. This is an open access article distributed under the Creative Commons Attribution-NoDerivatives License 4.0, which allows for redistribution, commercial and non-commercial, as long as it is passed along unchanged and in whole, with credit to the author.

Medicine (2018) 97:36(e12205)

Received: 25 September 2017 / Accepted: 13 August 2018

<http://dx.doi.org/10.1097/MD.00000000000012205>

and to extent of disease, ranging from an acute self-limited process to progressive fibrosis of the lung or other organs.^[4–8] In sarcoidosis treatment, the search for disease activity marker that associates with organ function (i.e., pulmonary function) is ongoing.^[9–25] Respiratory tract involvement is evaluated by regular clinical examinations, chest X-ray, and pulmonary function testing (spirometry). The most encouraging indicator for disease activity in clinical trial was pulmonary function testing, which showed the correlation with pulmonary PET outcomes.^[13–15]

Additionally, the serum angiotensin-converting enzyme (SACE) has been the most frequently used laboratory test in sarcoidosis. Some studies have shown that SACE is produced by the alveolar macrophages in the sarcoid granuloma, and SACE level reflects the total sarcoidosis granuloma burden.^[1,2] SACE level is commonly elevated and may correlate with disease activity.^[20–23]

To date, high-resolution computed tomography (HRCT) has been a routine item for airway or interstitial involvement diseases. Various studies have demonstrated that HRCT is superior to conventional radiography in detecting nodules, early fibrosis, and parenchymal distortion.^[6,9–12,15–19] Some HRCT features have the potential to discriminate between reversible disease (active inflammation) and irreversible disease (fibrosis).^[9]

Furthermore, HRCT abnormalities appeared to be useful in evaluating parameters of disease severity and lung functional impairment.^[9–12,16,17,20,25] However, the results of the correlation between HRCT scores and disease activity and/or lung function appeared to be conflicting for variable HRCT scoring systems. To achieve a valid, reliable evaluation of lung abnormalities, a standard quantitative estimation of radiological abnormalities is necessary.

Currently, the HRCT scoring system proposed by Benamore et al^[25]-CT activity score (CTAS) takes the extent of radiological abnormalities in pulmonary parenchyma into account, showing significant correlation with forced vital capacity (FVC) response to treatment. In addition, extent scores 4 radiological features (ground-glass opacity [GGO], interlobular septal thickening [IST], nodularity and consolidation) enrolled in CTAS correlated with at least one of the surrogates of disease activity, suggesting the validation of the relationship of CTAS to disease activity in sarcoidosis.

However, given that the limited patients were followed up in Benamore et al^[25] study, the relationship between CTAS and the changes of lung function after treatment will benefit from further verification with a larger cohort. In addition, whether the extent scores of CT abnormalities mentioned above would be different in patients with different SACE status, in other words, the relationship between CT features and serum marker-ACE was still debated. Therefore, the aims of the article were to address the reliability of CTAS and investigate the relationship between CTAS and lung function changes, aiming to provide a more reliable reference for assessment of disease activity; and to compare CTAS in patients with different SACE status, exploring the potential relationship between CTAS and SACE.

2. Materials and methods

2.1. Subjects

The Institutional Review Board granted approval for our retrospective study, waiving informed consent because of its retrospective nature. This retrospective study included 57 patients with newly diagnosed pulmonary sarcoidosis between December 2010 and September 2016. Inclusion criteria in the study: the initial laboratory test and spirometry were obtained within a 2-week interval before or after the HRCT; patients without corticosteroids therapy or comorbidity before HRCT examination. To assess pulmonary function changes that have occurred over time, follow-up spirometry in each patient was obtained about 6 months after the initial spirometry.

The 57 patients included 16 males and 41 females, 27 to 66 years of age (mean age 49 ± 10 years). Of these patients, 11 were ex-smoker/current smoker and 46 were nonsmoker. The diagnosis was confirmed by histology examination of lymph nodes including 16 (28.1%) transbronchial lung biopsy (TBLB), 18 (31.6%) endobronchial ultrasound-guided transbronchial needle aspiration (EBUS-TBNA), 8 (14.0%) thoracoscope, and 7 (12.3%) mediastinal biopsy. Two patients (3.5%) initially presented with a classic Löfgren's syndrome (fever, erythema nodosum, arthralgias, and bilateral hilar lymphadenopathy) without biopsy. For the other 6 patients (10.5%) without histological evidence, clinical features and bronchoalveolar fluid analysis consistent with the WASOG guidelines^[26] confirmed the final diagnosis. All the patients received systemic corticosteroids therapy after HRCT examination, but the dose and treatment

duration were adjusted according to clinical presentation. None of them have received immunosuppressive therapy during the 6 months.

2.2. HRCT technique and image analysis

HRCT scans were performed on either a 16-slice (Toshiba Aquilion), 320-slice (Toshiba Aquilion One) or a 256-slice CT scanner (Philips Brilliance iCT). All scans were acquired using the high-resolution technique. Images were acquired in the supine position after end-inspiration and extended from the lung apices to the costophrenic angles by using the following parameters: section thickness, 5 mm; section intervals, 5 mm; pitch, 0.75; rotation time, 330 ms; tube voltage, 120 kV; tube current, 200 mA; thin collimation 0.75 mm; reconstruction matrix, 512×512 . From raw data, 1-mm-thick section images were reconstructed at 1-mm intervals by using a high-spatial-frequency algorithm (B60S). All CT scans were obtained with window settings that were appropriate for lung parenchyma (window width, 1300 Hounsfield units [HU]; level, -450 HU) and mediastinum (window width, 400 HU; level, 40 HU). All data were analyzed on the postprocessing workstation EBW4.52 (Extended Brilliant Workshop 4.52, Philips Healthcare Systems).

The CT images were assessed in totally random order by 2 radiologists (with 6 years and 10 years of experience in chest CT imaging, respectively) without reference to the clinical or laboratory test results. Sarcoidosis-related HRCT abnormalities (including GGO (Fig. 1A), IST, nodule (Fig. 1B), conglomeration, consolidation (Fig. 1C), intrathoracic lymphadenopathy, fibrosis (Fig. 1D)) were scored for the presence, character, and extent follow the criteria defined in the previous study.^[25] Specifically, the sum of the scores for GGO, IST, nodularity and consolidation was defined as the CT activity score or CTAS and recorded. In addition, the pleural effusion and the fibrosis were also recorded without enrolling in CTAS scoring system. The fibrosis was defined as the presence of any honeycombing, reticulation, traction bronchiectasis or intralobular linear opacities with or without architectural distortion or lobar volume loss (Tables 1 and 2).

Each lung was divided into 3 zones on HRCT as follows: the upper zone above the carina in the cranio-caudal plane; the lower zone below the inferior pulmonary veins in the cranio-caudal plane; the middle zone between the upper and lower zones.

The extent of CT abnormalities was estimated visually in each aforementioned zone and measured by quartiles (25%) for GGO and consolidation, number of IST (≤ 5 or > 5) per zone, number of nodules per zone (0–25/26–50/ > 50), 2.5 cm intervals of short-axis diameter for conglomeration.^[25] In addition, the sub-1 mm nodules were considered GGO since indistinguishability between innumerable sub-1 mm and GGO with current HRCT resolution.

2.3. SACE examination

SACE examination was performed with 3 mL venous blood on fasting state in the morning, all specimen were sent to our clinical laboratory by immunoturbidimetry (reagent kit were provided by Beijing Strong Biotechnologies, Inc. The instrument was adopted by BECKMAN COULTER AU5800 type automatic biochemical analyzer, America). The normal range of the SACE level was 17 U/mL to 55 U/mL in our institution, and the upper limit of normal of the SACE level is above 55 U/mL.

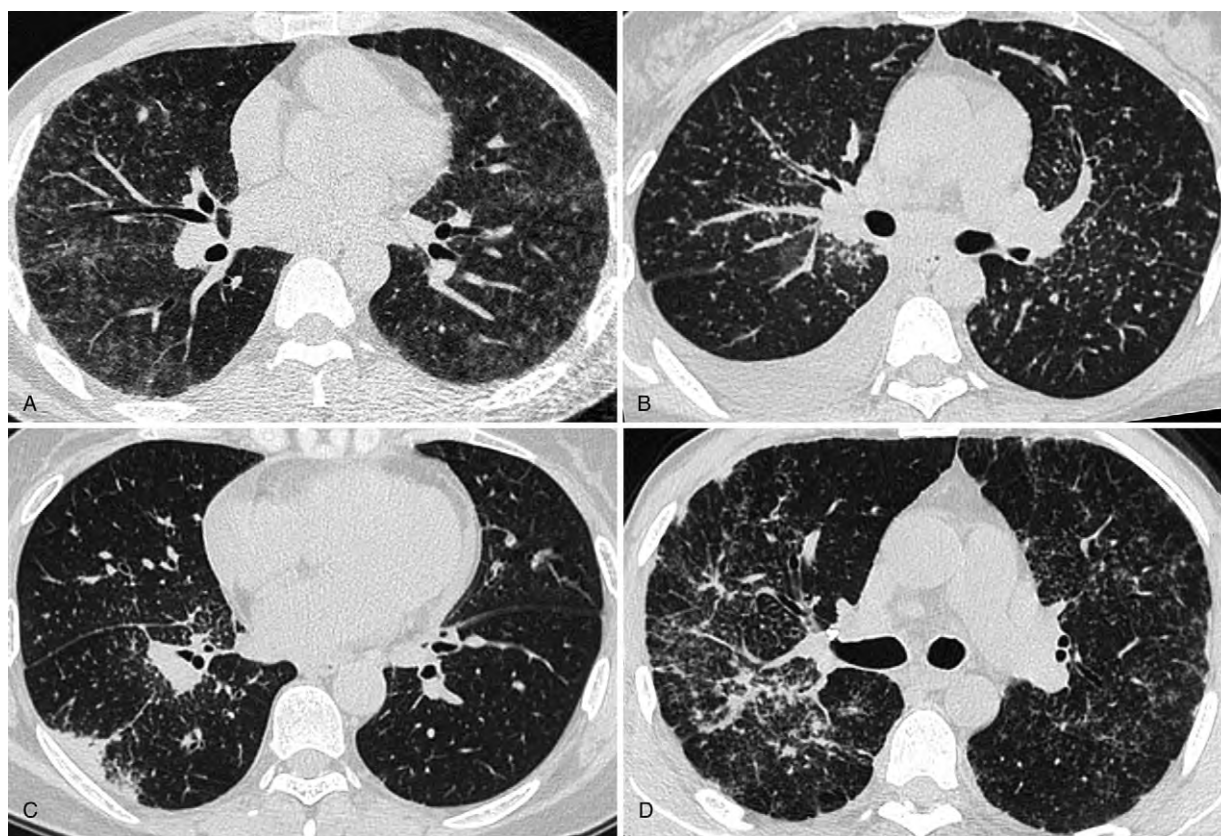


Figure 1. A, HRCT obtained at the level of right lower bronchus displayed bilateral diffuse ground-glass opacities in a 41-year-old male patient. Note the right hilar lymphadenopathy. The SACE level was 60.1 U/mL. B, HRCT showed micronodules with a perivascular distribution and thickening of bronchovascular bundles accompanied with right pleural effusion in a 43-year female patient. The SACE value was 68.1 U/mL. C, HRCT demonstrated consolidation in subpleural region, multiple micronodules clustered interlobar fissures and centrilobular interstitium of right lower lobe in a 50-year-old female patient, enlarged right hilar lymph nodes were also seen, the SACE level was 28.3 U/mL. D, HRCT depicted right bronchovascular bundles distortion in a 48-year male patient, a usual finding of pulmonary fibrosis. Note the bilateral irregular thickening of the pleura (pseudoplaque) and multiple miliary nodules. The SACE value was 33.7 U/mL. HRCT = high-resolution CT, SACE = serum angiotensin converting enzyme.

2.4. Pulmonary function test

All subjects performed spirometry, including vital capacity as the percent of the predicted value (%VC), forced expiratory volume in the first second (FEV_{1.0}), forced vital capacity (FVC), and total lung capacity as the percent of the predicted value (%TLC). The initial spirometry was performed within 2 weeks before or after HRCT examination, and the second spirometry was performed with a 6-month interval. The initial spirometric values (Table 3) and the changes between the twice spirometric results were both recorded.

Table 1
Definition of terms for abnormalities on HRCT.

Terms	Definition
Ground glass opacity	Increased lung attenuation, with preserved bronchial and vascular margins; nodules < 1 mm
Consolidation	Obviously increased pulmonary parenchymal attenuation with obscured vessels and airway walls
Internal septal thickening	Thickening of the septa between lobules (smooth or nodular)
Conglomeration	A large opacity > 3 cm surrounding and encompassing hilar bronchi and vessels

2.5. Statistical analysis

All data were expressed as mean ± standard deviation (SD) or median± interquartile range (IQR). The correlations between pulmonary function changes, SACE values, and CT activity score (CTAS), between SACE values and pulmonary function changes were evaluated by Spearman correlation analysis or Pearson

Table 2
Scoring system for abnormalities on HRCT.

Abnormalities	Score for extent
GGO (or nodules < 1 mm)	One zone 1–25% =1 point; one zone 26–50%=2 point; one zone 51–75%=3 point; one zone 76–100%=4 point
Consolidation	One zone 1–25%=1 point; 1 zone 26–50%=2 point; 1 zone 51–75%=3 point; 1 zone 76–100%=4 point
Interlobular septal thickening (IST)	One zone, up to 5=1 point; 1 zone >5=2 point
Nodules 1 mm or greater	One zone 1–25 nodules=1 point; 1 zone 26–50 nodules=2 point; 1 zone >50 nodules=3 point;
Conglomeration	Yes =1 point; no =0 point; each 2.5 cm dimension (right or left) =1
Lymphadenopathy	Yes =1 point; no =0 point.

Table 3**Clinical characteristics of 57 subjects.**

Factors	Mean±SD	Range
Gender (male: female)	(16:41)	—
Age, y	48.75±10.30	27–66
Smoking status (ex-/current smoker: nonsmoker)	(11:46)	—
SACE, U/mL	63.20±3.45	11.70–137.10
%VC	98.74±15.15	55.20–129.70
FEV _{1.0} /FVC, %	74.18±9.88	50.31–99.56
%TLC	88.65±12.86	52–116

%TLC=total lung capacity as percent of the predicted value, %VC=vital capacity as percent of the predicted value, FEV_{1.0}=forced expiratory volume in the first second, FVC=forced vital capacity, SACE=serum angiotensin converting enzyme, SD=standard deviation.

correlation analysis. According to SACE status, patients were divided into normal and high level 2 subgroups. Comparisons of pulmonary function parameters, HRCT abnormalities extent scores between SACE normal, and high 2 subgroups were performed using Mann–Whitney *U* test or Independent samples *t* test. Concordance rates and kappa values were calculated to show the reliability of calculating HRCT features and CTAS between observers. All statistical analyses were performed using a statistical software package (SPSS 17.0 for Windows, SPSS, Chicago, IL). A *P* values <.05 was considered to be significant.

3. Results

The concordance rates and kappa values were 91.2% to 95.4% and 0.85 to 0.91 for different HRCT features and CTAS. Clinical characteristics of subjects are summarized in Table 3. Extent scores for HRCT abnormalities are listed in Table 4. In addition, 4 patients (7.02%) presented with pleural effusion, 14 (24.56%) patients showed evidence of pulmonary fibrosis.

3.1. Correlations between pulmonary function changes, SACE and HRCT abnormality extent score

Following the scoring criterion for disease activity suggested by Benamore et al,^[25] the sum score of GGO, IST, consolidation, and nodularity is termed CTAS. Correlations between pulmonary function changes, SACE, and CTAS are summarized in Table 5. Pulmonary function changes and SACE both demonstrated significant correlations with CTAS.

Table 4**HRCT abnormalities and extent score.**

Abnormalities	N (percentage)	Median±IQR	Range
GGO	44 (77.19%)	3±4.5	0–24
IST	9 (15.79%)	0±0	0–12
Nodule	39 (68.42%)	2±3	0–18
Consolidation	18 (31.58%)	0±1.5	0–8
Conglomeration	12 (21.05%)	0±0	0–4
Intrathoracic lymphadenopathy	57 (100%)	1±0	1–1
Total score		7±8	1–36
CTAS		6±8	0–35

CTAS=the CT activity score, defined as the sum of the scores for GGO, IST, nodule and consolidation, GGO=ground glass opacity, HRCT=high-resolution computed tomography, IQR=interquartile range, IST=interlobular septal thickening.

Table 5**Correlation between pulmonary function changes, SACE values, and CT activity score (CTAS).**

Variables	Correlation to CTAS	
	Coefficient (ρ)	<i>P</i> value
Δ %VC	0.543	<.001
Δ FEV _{1.0} /FVC	0.417	.001
Δ %TLC	0.309	.019
SACE	0.435	.001

%TLC=total lung capacity as percent of the predicted value, %VC=vital capacity as percent of the predicted value, Δ =the value change after six months, FEV_{1.0}=forced expiratory volume in the first second, FVC=forced vital capacity, SACE=serum angiotensin converting enzyme.

We also have evaluated the relationships between pulmonary function changes, SACE values, and total score of the HRCT features (excluding fibrosis), and have observed similar results to CTAS's (Δ %VC: ρ = 0.509, *P*<.001; Δ FEV_{1.0}/FVC: ρ = 0.382, *P*=.003; Δ %TLC: ρ = 0.327, *P*=.013; SACE: ρ = 0.440, *P*=.001).

In addition, the SACE value showed significant correlations with pulmonary function changes (Δ %VC: ρ = 0.413, *P*=.001; Δ FEV_{1.0}/FVC: ρ = 0.317, *P*=.016; Δ %TLC: ρ = 0.439, *P*=.001).

3.2. Pulmonary function parameters, HRCT scores between different SACE status

The values of pulmonary function parameters and HRCT scores in patients with different SACE status were described in Table 6. Worse initial lung function, larger changes of %TLC values, and higher HRCT scores were observed in SACE high-level subgroup.

4. Discussion

In the present study, CTAS demonstrated the significant correlations with lung function changes (Δ %VC: ρ = 0.543, *P*<.001; Δ FEV_{1.0}/FVC: ρ = 0.417, *P*=.001; Δ %TLC: ρ = 0.309, *P*=.019). Interestingly, similar outcomes were observed in the total score of HRCT abnormalities. The results suggest that

Table 6**Comparisons of pulmonary function parameters, HRCT abnormalities scores between different SACE status.**

	SACE status		<i>P</i> value
	Normal level (n=32)	High level (n=25)	
Initial pulmonary function			
%VC	104.62±9.21	91.20±17.91	.001
FEV _{1.0} /FVC (%)	78.95±7.03	68.07±9.74	<.001
%TLC	94.13±9.14	81.63±13.67	<.001
Pulmonary function changes			
Δ %VC	0.60±6.63	2.60±13.05	.096
Δ FEV _{1.0} /FVC (%)	1.93±7.86	2.00±9.33	.317
Δ %TLC	0.90±3.28	2.30±7.90	.037
HRCT score			
Total score	7±3.75	11±11	<.001
CTAS	5±3.5	10±12	<.001

Note: data were expressed as median± interquartile range (IQR).

%TLC=total lung capacity as percent of the predicted value, %VC=vital capacity as percent of the predicted value, Δ =the value change after six months, CTAS=the CT activity score, FEV_{1.0}=forced expiratory volume in the first second, FVC=forced vital capacity, HRCT=high-resolution computed tomography, SACE=serum angiotensin converting enzyme.

CTAS is useful in evaluating disease activity in sarcoidosis. In addition, higher extent scores of HRCT and larger changes of lung function were also observed in SACE high-level subgroup, which further supported the aforementioned outcome to some degree.

Chest HRCT is an important modality to identify chest involvement of sarcoidosis. It has been demonstrated that 15% of symptomatic patients have normal chest X-ray but abnormal findings on CT scans.^[27] The correlation between HRCT abnormalities and impaired lung function at rest has been well estimated in previous studies.^[9–12,16,17,20,25] Thus far, most of the previous studies have been focused on the disease severity (not activity) on HRCT, and its relationship with lung function impairment. The HRCT features of pulmonary sarcoidosis could be divided into reversible and irreversible ones,^[6,7,9] in other words, “reversible” feature could be improved after treatment over time, while “irreversible” ones would be unchangeable with or without treatment. GGO, IST and nodular has been proved to be potentially reversible changes in sarcoidosis.^[9] Furthermore, HRCT features including GGO, IST, nodular, and consolidation have been demonstrated the significant correlation with lung function,^[11,16,19] although the sample size and, more importantly, the scoring system were different. Therefore, it is reasonable to predict that the disease activity scoring system CTAS involving of GGO, IST, nodular, and consolidation associated with lung function changes after treatment in this study.

The increased level of SACE is thought to be secondary to increased expression by the epithelioid cells present in the granulomas.^[28] One study showed that SACE was produced by the alveolar macrophages in the sarcoid granuloma, and SACE levels reflected the secreted total granuloma burden.^[1,2] Many studies have confirmed that SACE levels can reflect the activity of the disease,^[3,21–24] furthermore, it has been reported that the baseline and serial SACE levels correlate with lung function improvement during methotrexate therapy in sarcoidosis patients.^[21] Therefore, SACE could be supposed to be an index for disease activity in some degree.

Although it was quite difficult to speculate about the intrinsic reason that underlay this observation, pathologic correlation factors may lead to the correlation between morphology score and SACE in sarcoidosis. First of all, the high percent of GGO (77.19%) and nodular (68.42%) were observed in the lung parenchyma. More recently, studies have shown that ground-glass opacities actually pointed to numerous granulomas along the interlobular fissures and septa and within the centrilobular interstitium surrounding arterioles and bronchioles.^[20] They demonstrated as ground-glass opacities, because of beyond the resolution of HRCT.^[3,4,29,30] In addition, ground-glass opacities also represented centrilobular interstitial disease in some cases.^[23,30] Also, thickened bronchovascular bundles and the surrounding micronodules on HRCT, pathologically corresponded to granulomas surrounding the connective tissue sheath of bronchovascular bundles, which caused bronchovascular bundles nodular or irregular thickening.^[4] Whether granulomas stand in the peribronchial interstitium or centrilobular interstitium, these 2 signs are representative of accumulation of granuloma in the lung. Nodules located in bronchovascular bundles distribute more widespread than that located in subpleural regions, the interlobular septa, centrilobular interstitium, and parts of subpleural nodules represent intrapulmonary lymph nodes.^[31] Second, 100% lymphadenopathy presented in this study, although it was not enrolled in the CTAS. The bilateral hilar lymph node enlargement also

undoubtedly added the total granuloma burden, although the corresponding influence on SACE may be variable in individuals. Together, these factors may explain the significant correlation between CTAS and SACE.

Our study has the following clinical significances. First, CTAS has potential clinical value to judge the disease activity of patients with sarcoidosis. CTAS showed the significant correlations with lung function and the SACE in pulmonary sarcoidosis. Second, we can indirectly judge treatment response and determine the clinical outcome with HRCT features. Finally, based on CTAS and SACE, pulmonary function and improvement after treatment might be predicted in some degree.

Our study has some limitations that need to be addressed. First, the number of cases is limited, and the study is a retrospective study. Studies with larger patients are needed to reduce selective bias. Second, considering the limited subjects, the potential effects of smoking on HRCT appearance, function test, and SACE level were not analyzed; this is a monocentric study focusing on the scoring system proposed by Benamore et al^[25] without comparison with other scoring systems on HRCT. Third, in this study 100% intrathoracic lymphadenopathy was observed, similar as in Benamore et al^[25] study. However, for the subjects without intrathoracic lymphadenopathy, the CTAS scoring system still needs to be discussed. Finally, it is necessary to follow up patients and to make a dynamic longitudinal study between HRCT activity score and clinical parameters (including pulmonary function, serum ACE) in order to reflect the outcome of the disease.

5. Conclusion

In conclusion, our results suggest that CTAS involving of GGO, IST, nodular and consolidation on HRCT could be a promising index for disease activity; CTAS demonstrated significant correlations both with lung function changes after treatment and SACE; subjects with high SACE prefer to behave higher CTAS on HRCT and worse initial lung function to some degree. Prospective studies with a large cohort designed to address further verification are warranted before wide clinical practice.

Author contributions

Conceptualization: Jianghui Duan, Hongliang Sun, Wu Wang.

Data curation: Jianghui Duan, Yanyan Xu, Haixu Zhu, Haibo Zhang, Shilong Sun, Hongliang Sun.

Formal analysis: Jianghui Duan, Yanyan Xu, Haibo Zhang, Hongliang Sun.

Funding acquisition: Hongliang Sun, Wu Wang.

Investigation: Hongliang Sun.

Methodology: Yanyan Xu, Hongliang Sun.

Project administration: Hongliang Sun, Sheng Xie.

Resources: Jianghui Duan, Haibo Zhang, Sheng Xie.

Software: Jianghui Duan, Haixu Zhu.

Supervision: Wu Wang.

Writing – original draft: Jianghui Duan, Yanyan Xu.

Writing – review & editing: Yanyan Xu, Haixu Zhu, Hongliang Sun, Wu Wang, Sheng Xie.

References

- [1] Rosen Y. Pathology of sarcoidosis. *Semin Respir Crit Care Med* 2007;28:36–52.
- [2] Sheffield EA. Pathology of sarcoidosis. *Clin Chest Med* 1997;18:741–54.

- [3] Wessendorf TE, Bonella F, Costabel U. Diagnosis of sarcoidosis. *Clin Rev Allergy Immunol* 2015;49:54–62.
- [4] Little BP. Sarcoidosis: overview of pulmonary manifestations and imaging. *Semin Roentgenol* 2015;50:52–64.
- [5] Koyama T, Ueda H, Togashi K, et al. Radiologic manifestations of sarcoidosis in various organs. *Radiographics* 2004;24:87–104.
- [6] Criado E, Sánchez M, Ramírez J, et al. Pulmonary sarcoidosis: typical and atypical manifestations at high-resolution CT with pathologic correlation. *Radiographics* 2010;30:1567–86.
- [7] Nishimura K, Itoh H, Kitaichi M, et al. Pulmonary sarcoidosis: correlation of CT and histopathologic findings. *Radiology* 1993;189:105–9. Erratum in: *Radiology* 1994;190:907.
- [8] Reich JM. Mortality of intrathoracic sarcoidosis in referral vs population-based settings: influence of stage, ethnicity, and corticosteroid therapy. *Chest* 2002;121:32–9.
- [9] Murdoch J, Müller NL. Pulmonary sarcoidosis: changes on follow-up CT examination. *AJR Am J Roentgenol* 1992;159:473–7.
- [10] Oberstein A, von Zitzewitz H, Schweden F, et al. Non invasive evaluation of the inflammatory activity in sarcoidosis with high-resolution computed tomography. *Sarcoidosis Vasc Diffuse Lung Dis* 1997;14:65–72.
- [11] Drent M, De Vries J, Lenters M, et al. Sarcoidosis: assessment of disease severity using HRCT. *Eur Radiol* 2003;13:2462–71.
- [12] Akira M, Kozuka T, Inoue Y, et al. Long-term follow-up CT scan evaluation in patients with pulmonary sarcoidosis. *Chest* 2005;127:185–91.
- [13] Keijsers RG, Verzijlbergen EJ, van den Bosch JM, et al. 18F-FDG PET as a predictor of pulmonary function in sarcoidosis. *Sarcoidosis Vasc Diffuse Lung Dis* 2011;28:123–9.
- [14] Mostard RL, Vöö S, van Kroonenburgh MJ, et al. Inflammatory activity assessment by F18 FDG-PET/CT in persistent symptomatic sarcoidosis. *Respir Med* 2011;105:1917–24.
- [15] Mostard RL, Verschakelen JA, van Kroonenburgh MJ, et al. Severity of pulmonary involvement and (18)F-FDG PET activity in sarcoidosis. *Respir Med* 2013;107:439–47.
- [16] Sileo C, Epaud R, Mahloul M, et al. Sarcoidosis in children: HRCT findings and correlation with pulmonary function tests. *Pediatr Pulmonol* 2014;49:1223–33.
- [17] Polverosi R, Russo R, Coran A, et al. Typical and atypical pattern of pulmonary sarcoidosis at high-resolution CT: relation to clinical evolution and therapeutic procedures. *Radiol Med* 2014;119:384–92.
- [18] Keijsers RG, van den Heuvel DA, Grutters JC. Imaging the inflammatory activity of sarcoidosis. *Eur Respir J* 2013;41:743–51.
- [19] Remy-Jardin M, Giraud F, Remy J, et al. Pulmonary sarcoidosis: role of CT in the evaluation of disease activity and functional impairment and in prognosis assessment. *Radiology* 1994;191:675–80.
- [20] Ors F, Gumus S, Aydogan M, et al. HRCT findings of pulmonary sarcoidosis; relation to pulmonary function tests. *Multidiscip Respir Med* 2013;8:8.
- [21] Vorselaars AD, van Moorsel CH, Zanen P, et al. ACE and sIL-2R correlate with lung function improvement in sarcoidosis during methotrexate therapy. *Respir Med* 2015;109:279–85.
- [22] Popević S, Šumarac Z, Jovanović D, et al. Verifying sarcoidosis activity: chitotriosidase versus ace in sarcoidosis— case-control study. *J Med Biochem* 2016;35:390–400.
- [23] Mathur RS, Kurdikar VL, Shah JR. Serum angiotensin converting enzyme in the diagnosis of pulmonary sarcoidosis. *J Assoc Physicians India* 1990;38:474–5.
- [24] Sainani GS, Mahbubani V, Trikannad V. Serum angiotensin converting enzyme activity in sarcoidosis and pulmonary tuberculosis. *J Assoc Physicians India* 1996;44:29–30.
- [25] Benamore R, Kendrick YR, Repapi E, et al. CTAS: a CT score to quantify disease activity in pulmonary sarcoidosis. *Thorax* 2016;71:1161–3.
- [26] Statement on sarcoidosis Joint Statement of the American Thoracic Society (ATS), the European Respiratory Society (ERS) and the World Association of Sarcoidosis and Other Granulomatous Disorders (WASOG) adopted by the ATS Board of Directors and by the ERS Executive Committee, February 1999. *Am J Respir Crit Care Med* 1999;160:736–55.
- [27] Epler GR, McCloud TC, Gaensler EA, et al. Normal chest roentgenograms in chronic diffuse infiltrative lung disease. *N Engl J Med* 1978;298:934–9.
- [28] Silverstein E, Pertschuk LP, Friedland J. Immunofluorescent localization of angiotensin converting enzyme in epithelioid and giant cells of sarcoidosis granulomas. *Proc Natl Acad Sci U S A* 1979;76:6646–8.
- [29] Nakatsu M, Hatabu H, Morikawa K, et al. Large coalescent parenchymal nodules in pulmonary sarcoidosis: "sarcoid galaxy" sign. *AJR Am J Roentgenol* 2002;178:1389–93.
- [30] Marchiori E, Zanetti G, Barreto MM, et al. Atypical distribution of small nodules on high resolution CT studies: patterns and differentials. *Respir Med* 2011;105:1263–7.
- [31] Koo HJ, Chae EJ, Kim JE, et al. Presence of macronodules in thoracic sarcoidosis: prevalence and computed tomographic findings. *Clin Radiol* 2015;70:815–21.



Could IVIM and ADC help in predicting the KRAS status in patients with rectal cancer?

Yanyan Xu¹ · Qiaoyu Xu¹ · Hongliang Sun¹ · Tongxi Liu¹ · Kaining Shi² · Wu Wang¹

Received: 5 December 2017 / Revised: 8 January 2018 / Accepted: 12 January 2018 / Published online: 15 February 2018
© European Society of Radiology 2018

Abstract

Purpose To evaluate the diagnostic potential of DW-MRI relative parameters for differentiation of rectal cancers with different Kirsten rat sarcoma viral oncogene homologue (KRAS) mutation status.

Methods Fifty-one patients with rectal cancer underwent diffusion-weighted MR imaging with eight b values. ADCs (including Max-ADC, Min-ADC and Mean-ADC) and IVIM parameters (*D*, pure diffusion; *f*, perfusion fraction; *D**, pseudodiffusion coefficient) were respectively calculated by mono- and bi-exponential analysis. Patients were stratified into two groups: KRAS wild type and mutant. The DW-MRI-derived parameters between the KRAS wild-type group and KRAS mutant group were compared using the Mann-Whitney U test. Receiver-operating characteristic (ROC) analysis of discrimination between KRAS wild-type and KRAS mutant rectal cancer was performed for the DW-MRI-derived parameters.

Results Max-ADC, Mean-ADC and *D* values were significantly lower in the KRAS mutant group than in the KRAS wild-type group, whereas a higher *D** value was demonstrated in the KRAS mutant group. According to the ROC curve, Mean-ADC and *D** values showed moderate diagnostic significance with the AUC values of 0.756 and 0.710, respectively. The cut-off values for Mean-ADC and *D** were $1.43 \times 10^{-3} \text{mm}^2/\text{s}$ and $26.58 \times 10^{-3} \text{mm}^2/\text{s}$, respectively.

Conclusion Rectal cancers had distinctive diffusion/perfusion characteristics in different KRAS mutation statuses. The DW-MRI-derived parameters, specifically Mean-ADC and *D**, show a moderate diagnostic significance for KRAS status.

Key Points

- Rectal cancers with different KRAS mutation statuses demonstrated distinctive diffusion/perfusion characteristics.
- Max-ADC, Mean-ADC and *D* values were lower in the KRAS mutant group.
- A higher *D** value was demonstrated in the KRAS mutant group.
- IVIM-DW MRI may potentially help preoperative KRAS mutant status prediction.

Keywords Rectal cancer · Magnetic resonance imaging · Diffusion · Perfusion · Mutation

Abbreviations

ADC	Apparent diffusion coefficient
CRC	Colorectal cancer
<i>D</i>	Diffusion coefficient
<i>D*</i>	Pseudo-diffusion coefficient
DWI	Diffusion-weighted imaging
EGFR	Epidermal growth factor receptor
<i>f</i>	Perfusion fraction

IVIM	Intravoxel incoherent motion
KRAS	Kirsten rat sarcoma viral oncogene homologue
MRI	Magnetic resonance imaging
NCCN	National Comprehensive Cancer Network
ROI	Region of interest
ROC	Receiver-operating characteristic
TE	Echo time
TR	Repetition time
TSE	Turbo spin echo

✉ Hongliang Sun
stentorsun@gmail.com

¹ Department of Radiology, China-Japan Friendship Hospital, No.2 Yinghua East Street, Chaoyang District, Beijing 100029, China

² Philips Healthcare, Beijing 100600, China

Introduction

Rectal cancer, which accounts for 30–35% [1] of all colorectal cancer (CRC) cases, is distinctive from the rest of the colon, and local recurrence is a major problem for clinical

management. Currently, it is considered that CRC occurs as a result of the accumulation of both mutations and epigenetic alterations in several key genes [2]. Kirsten rat sarcoma viral oncogene homologue (KRAS) is one of those key genes, and its mutations were observed in approximately 35–40% of CRCs [3, 4]. Generally, metastatic CRCs with KRAS mutations tended to be resistant to anti-EGFR (epidermal growth factor receptor) monoclonal antibody-targeted therapy [5, 6]. It has been explicitly pointed out in the National Comprehensive Cancer Network (NCCN) clinical practice guidelines [5, 6] that the KRAS mutation is a highly specific negative biomarker for benefitting from anti-EGFR monoclonal antibody-targeted therapy. In general, postoperative pathology specimens are required for KRAS mutation status testing; however, patients with more advanced rectal cancer may not be treated surgically to obtain specimens for testing. Therefore, further effort is desirable for the development of a relatively simple and noninvasive method that can be helpful for the differentiation of KRAS mutations and then assisting in selecting the most suitable adjuvant therapeutic methods.

Much work has been focused on the MR functional imaging, such as diffusion-weighted magnetic resonance imaging (DW-MRI), providing objective and quantitative parameters [ADCs (including Max-ADC, Min-ADC and Mean-ADC) and IVIM parameters (D , pure diffusion; f , perfusion fraction; D^* , pseudodiffusion coefficient)] in vivo. Currently, most interest is focussed on developing the role of various DW-MRI-derived parameters in tumour characterisation, predicting tumour aggressiveness or monitoring treatment response [7–9]. DW-MRI has rarely been investigated in genomic expression. As we know, most of the tumour's aggressive bio-behaviour can be considered the result of interior genetic regulation, so we assume that rectal cancers with different KRAS genetic phenotypes might present with variable DW-MRI characteristics. To date, the DW-MRI relative parameter characteristics in rectal cancers with different KRAS mutation statuses are unknown. Thus, the aim of this retrospective study was to detect if the DW-MRI-derived parameters can predict the genotype of rectal cancer (KRAS mutant/wild type).

Materials and Methods

Patients and tissue samples

This retrospective study was approved by the institutional review board of the hospital, and waived the requirement for written informed consent. Between August 2013 and December 2014, 109 patients with biopsy-proven rectal adenocarcinoma underwent pelvic MR examination (including multi- b value DW-MRI sequences). Exclusion criteria were: (1) previous rectal surgery ($n = 3$); (2) pre-examination

neoadjuvant chemoradiotherapy or unidentified herbal medicine therapy for the rectal lesion ($n = 25$); (3) heavy intestinal peristalsis artefacts ($n = 4$); (4) small lesions (< 5 mm) hard to identify on images ($n = 3$); (5) without KRAS testing ($n = 12$); (6) mucinous adenocarcinoma ($n = 11$). Finally, 51 patients were enrolled in this study. The relevant detailed clinical data are illustrated in Table 1. Surgical pathology results of all patients were analysed by a pathologist with 6 years' experience in gastrointestinal pathological diagnosis. Genomic DNA was extracted from formalin-fixed paraffin-embedded (FFPE) tissue using the QLAamp DNA FFPE Tissue kit (Qiagen), and KRAS mutations were examined by the amplification refractory mutation system (ARMS) method. According to the test results, patients were stratified into two groups: KRAS wild type and mutant, and the patients with KRAS mutation were further divided into codon 12 and codon 13 subgroups based on different mutation locations. From the analysis of the surgical specimens, 38 patients had the KRAS wild type and 13 patients had the KRAS mutation including eight codon 12 mutations (G12A, G12C, G12S, G12V) and five codon 13 mutations (G13A).

Patient preparation and imaging protocol

The patients were on a low-residue diet before the MRI examination and were asked to fast on the day of the examination. An intramuscular injection of 10 mg anisodamine hydrochloride was given to each patient to prevent intestine peristalsis 10 min prior to the MR examination. Pelvis MR scanning was performed on a 3-T whole-body scanner (Ingenia, Philips Medical Systems) with a gradient strength of 45 mT/m and a gradient switching rate of 200 mT/m/ms, using a 16-channel anterior torso dS coil and a 16-channel posterior table dS coil.

The 2D sagittal and oblique coronal T2W (parallel to long axis of the tumour) Turbo spin echo (TSE) sequences were performed with the following parameters: repetition time (TR), 3761 ms; echo time (TE), 110 ms; field of view (FOV), 24 × 24 cm; slice thickness, 3 mm with 0.3-mm gap;

Table 1 Basic clinical information of rectal cancers ($n = 51$)

Factors	Numbers/values
Patient age (years)*	61.3 ± 13.6
Gender n (%)	
Male	29 (57.7%; 29/51)
Female	22 (42.3%; 22/51)
KRAS status	
Wild type	38 (74.5%; 38/51)
Mutant codon 12	8 (15.7%; 8/51)
Mutant codon 13	5 (9.8%; 5/51)

Note. * Data are means ± standard deviation

slice number, 24 acquisition matrix, 336×252 ; number of sample (signals) averaged (NSA) 1; an oblique axial T2W-high resolution sequence was planned perpendicularly to the tumour axis in the sagittal view: TR 3865 ms, TE 100 ms, FOV 14×14 cm, slice thickness 3 mm with 0.3-mm gap, slice number 20, acquisition matrix 232×228 .

An oblique axial multi-b value DW-MRI sequence perpendicular to the tumoral axis in sagittal view was performed with the parallel acquisition technique (sensitivity encoding, SENSE) using a single-shot echo-planar imaging (SE-EPI) pulse sequence with free breathing using the following parameters: TE/TR 76/6000 ms, FOV 20×30 cm, slice thickness 5 mm with 0.2-mm gap, slice number 24, acquisition matrix 80×144 , NSA 6 and eight b values (0, 25, 50, 75, 150, 400, 800 and 1000s/mm^2). Frequency selection plus the inversion recovery fat-suppression technique (spectral attenuated inversion recovery) was adopted in the DWI sequence. The scan time for the DWI sequence was about 6 min 30 s.

Image processing and analysis

The raw data of multi-b value DW images were transferred to a workstation (Extended Workspace 4.1; Philips Healthcare Systems) and analysed with in-house software (IDL6.3 software). The ADC was obtained by using all b values ($0\text{--}1000\text{s/mm}^2$) fitted to the following equation:

$$S_b/S_0 = \exp(-bADC) \quad (1)$$

where S_b is the signal intensity at a given b value and S_0 is the signal intensity observed in the absence of a diffusion gradient. In the bi-exponential model, the IVIM parameters were calculated by the following equation [10]:

$$S_b/S_0 = (1-f)\exp(-bD) + f\exp(-bD^*) \quad (2)$$

where S_b is the signal intensity in the pixel with the diffusion gradient, S_0 is the signal intensity in the pixel without a diffusion gradient, D is the true diffusion as reflected by pure molecular diffusion, f is the fractional perfusion related to microcirculation, and D^* is the pseudodiffusion coefficient related to perfusion.

Conventional T2WI and DWI ($b = 1000\text{s/mm}^2$) images were used as references to determine lesion areas on corresponding DWI colour-coded maps. Regions of interest (ROIs) were manually drawn covering the entire tumour area on all continuous slices (T2WI, DWI images; Fig. 1a–b), avoiding the inclusion of intestinal gas, liquid and anatomical structures by one radiologist (H.S., 10 years' experience in gastrointestinal imaging). Macroscopic necrosis, if any, would be excluded. The DW-MRI-derived parameter values (ADCs, D , f , D^* ; Fig. 1c–f) for each tumour were calculated by the pixel-by-pixel fitting method and expressed as mean values of all pixels within the all ROIs. Inter-observer reliability of DW-MRI

derived-parameters (ADC, D , f and D^*) used in this study were proved to be good to excellent, as reported in a previous study with the same observers (the intraclass correlation coefficient, abbreviated ICC, ranged from 0.7444 to 0.9106) [11]. Furthermore, volumetric analysis demonstrated better-interobserver reproducibility when compared with single-section ROI analysis [12]. Accordingly, in the present study, volumetric measurement by a single radiologist was regarded as sufficient.

Statistical Analysis

All analyses were performed with JMP 12.0 statistical software (SAS Institute). Continuous variables were expressed as the mean \pm standard deviation. Comparisons of continuous variables, including DW-MRI parameters of rectal cancers with the codon 12 subgroup versus codon 13 subgroup, were made using the Mann-Whitney test. Then, receiver-operating characteristic (ROC) analysis was performed to evaluate the diagnostic performance of the DW-MRI-derived parameters (ADCs, D , f , D^* values) for KRAS status. The areas under the ROC curve (AUC) were calculated: an AUC value < 0.50 indicated poor diagnostic accuracy; an AUC value of 0.51–0.70, fair diagnostic accuracy; an AUC value of 0.71–0.90, moderate diagnostic accuracy; an AUC value > 0.91 , high diagnostic accuracy. The cut-off values with the largest Youden index [(sensitivity + specificity) - 1] were calculated from the ROC curves. The final KRAS testing results were used as the standard. For all the analyses mentioned above, $p < 0.05$ was considered statistically significant.

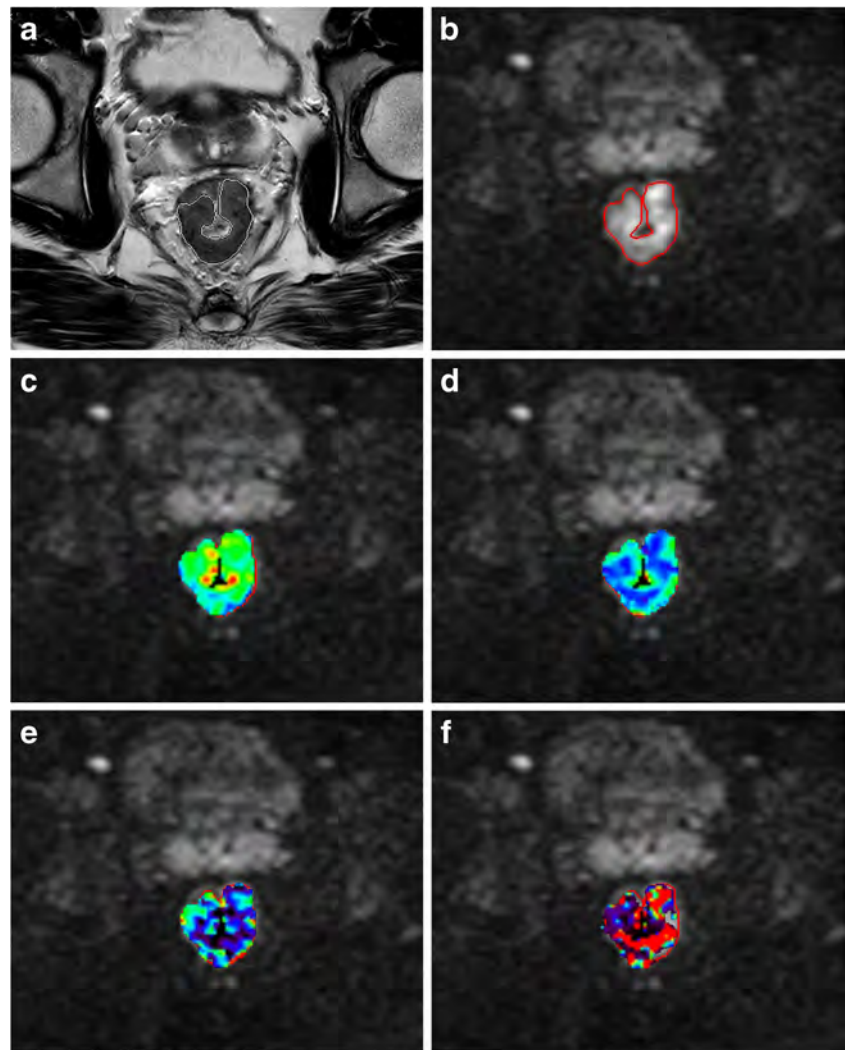
Results

DW-MRI-derived parameters in the KRAS wild-type and mutant groups

Values of DW-MRI-derived parameters (Max-ADC, Min-ADC, Mean-ADC, D , f , D^*) of the KRAS wild-type and mutant groups are described in Table 2. Regarding the differentiation of the KRAS mutant group from the KRAS wild-type group, the values of Max-ADC, Mean-ADC and D in the mutant group were significantly lower than those in the wild-type group ($p = 0.04$, $p = 0.01$ and $p = 0.03$, respectively), while a higher D^* value was demonstrated in the mutant group ($p = 0.03$). However, no significant differences were demonstrated in the values of Min-ADC and f between the two groups ($p = 0.27$ and $p = 0.29$, respectively).

In addition, the values of DW-MRI-derived parameters between the codon 12 and codon 13 subgroups showed no statistical differences (Max-ADC: $z = 0.66$, $p = 0.51$; Min-ADC: $z = 0.29$, $p = 0.77$; Mean-ADC: $z = 0.52$, $p = 0.61$; D : $z = 0.51$, $p = 0.61$; f : $z = 0.22$, $p = 0.83$; D^* : $z = 0.66$, $p = 0.51$).

Fig. 1 Images of 46-year-old male patient with rectal cancer. **a** Oblique axial T2W-high resolution sequence planned perpendicularly to the bowel with tumour; outline indicates tumour region. **b** Diffusion-weighted image (DWI) obtained at b of 1000s/mm^2 ; outline indicates tumour region. **c-f**: D : parametric maps (ADC, D , f and D^* , respectively) fused with relevant DWIs



Predictive significance of DW-MRI-derived parameters for KRAS mutation status

In the ROC analysis for the differentiation between the *KRAS* wild-type and mutant group, AUC values of Max-ADC, Min-ADC, Mean-ADC, D , f and D^* were 0.695, 0.604, 0.756, 0.701, 0.599 and 0.710, respectively. These findings suggested that Mean-ADC and D^* showed moderate diagnostic significance for KRAS mutation in rectal cancer, while the

diagnostic values of Max-ADC, Min-ADC, D and f showed fair diagnostic accuracy. According to the ROC curve (Fig. 2a), the cut-off value for Mean-ADC was $1.43 \times 10^{-3} \text{mm}^2/\text{s}$. The Mean-ADC value for the KRAS mutant group was lower than the cut-off value and that for the KRAS wild-type group was greater than the cut-off value, with an accuracy rate of 78.43%, sensitivity of 69.23% and specificity of 81.58%. The cut-off value for D^* was $26.58 \times 10^{-3} \text{mm}^2/\text{s}$. The D^* value for the KRAS mutant group was higher than the cut-off value and

Table 2 Rectal cancer DW-MRI relative parameters in different KRAS statuses

DW-MRI -derived parameters	<i>KRAS</i> mutant ($n = 13$)	<i>KRAS</i> wild type ($n = 38$)	z	p
Max-ADC ($\times 10^{-3} \text{mm}^2/\text{s}$)	2.08 ± 0.49	2.35 ± 0.42	2.08	0.04
Min-ADC ($\times 10^{-3} \text{mm}^2/\text{s}$)	0.71 ± 0.32	0.74 ± 0.18	1.10	0.27
Mean-ADC ($\times 10^{-3} \text{mm}^2/\text{s}$)	1.26 ± 0.36	1.43 ± 0.22	2.72	0.01
D ($\times 10^{-3} \text{mm}^2/\text{s}$)	0.94 ± 0.27	1.13 ± 0.33	2.14	0.03
f (%)	19.47 ± 12.25	16.78 ± 14.04	-1.05	0.29
D^* ($\times 10^{-3} \text{mm}^2/\text{s}$)	70.77 ± 67.77	32.98 ± 43.74	2.22	0.03

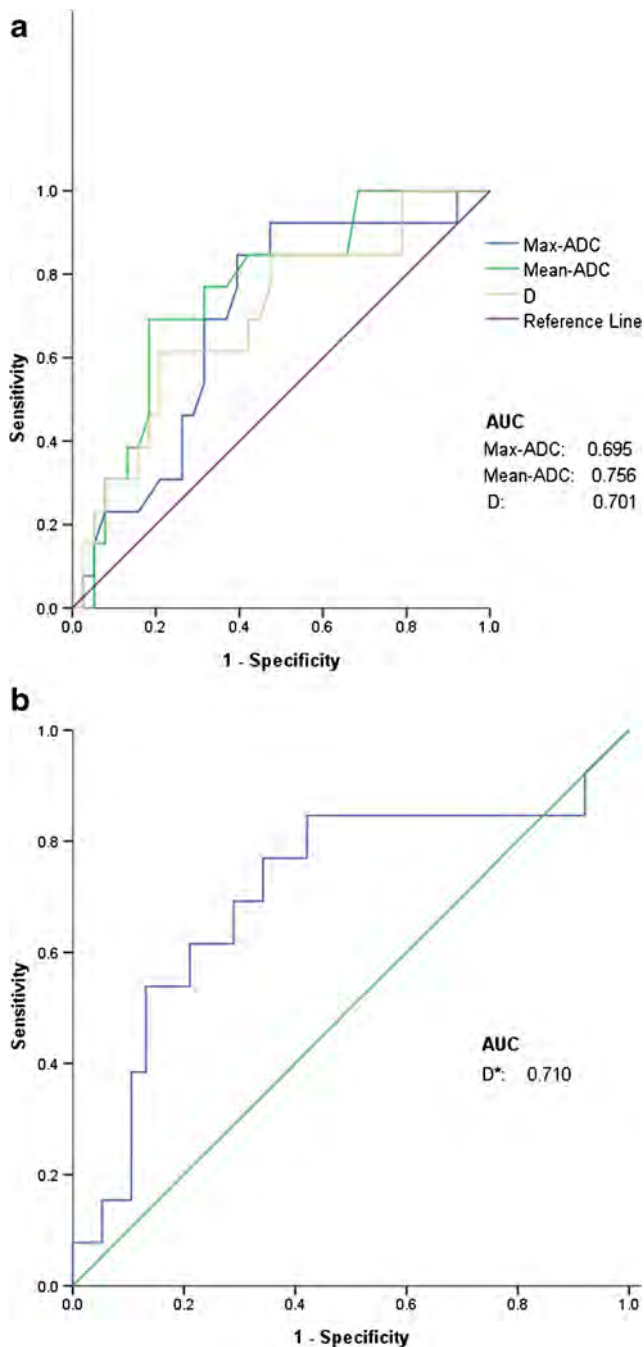


Fig. 2 Receiver-operating characteristic curves for Max-ADC, Mean-ADC, D (**a**) and D^* (**b**) in distinguishing KRAS mutant rectal cancers from wild-type ones

that for the KRAS wild-type group was lower than the cut-off value, with an accuracy rate of 68.62%, sensitivity of 76.92% and specificity of 65.79% (Fig. 2b).

Discussion

In the present study, lower Max-ADC, Mean-ADC, D and higher D^* values were observed in rectal cancers with the

KRAS mutant than in those with the wild type. According to the ROC analysis, Mean-ADC and D^* values showed moderate diagnostic significance for the KRAS mutant status with the AUC values of 0.756 and 0.710, respectively. Theoretically, ADC integrates the effects of both diffusion (D) and perfusion (D^*), reflecting the total diffusion in tissues. However, ADC is mainly a diffusion-related parameter rather than a perfusion-related parameter at high b values (> 200 s/mm²). As the diffusion coefficient level is mainly decided by the ratio of the intra- and extracellular space in tissue [10], both ADC and D are generally considered to be negatively correlated with the cellularity and positively correlated with necrosis and cystic changes in tissue [13, 14]. According to IVIM theory [10], D^* (pseudo-diffusion coefficient) is associated with perfusion with the equation stating that $D^* = (l \cdot v) / 6$, where l means the length of the voxel capillary and v is the average velocity of blood in the capillary [15]. Thus, lower Max-ADC, Mean-ADC and D and higher D^* values observed in the KRAS mutant group in the present study may suggest a relatively tight tumour cell structure and hypervascularity in the tumour.

It has been reported that the DW-MRI-derived parameters have clinical value in characterising tumour biological behaviour [9] and predicting tumour prognosis [12]. The values of ADC and D tended to decrease with higher T stages, and f and D^* were independent predictors for T staging [16, 17]. In addition, diffusion-related IVIM-based parameters (D and ADC) have been helpful to predict the treatment response to CRT for locally advanced cancers and nasopharyngeal carcinoma [13, 18].

Mutations of the KRAS oncogene result in the constitutive activation of the G-protein signal transduction pathway, associating with diffuse proliferation and decreased apoptosis [19, 20]. However, to date, there are no consistent results about the associations between KRAS mutations and CRC prognosis. Shigenori et al. [21] reported that CRC with KRAS mutations were associated with poor prognosis. Similar results were also observed in the Kirsten Ras Colorectal Cancer Collaborative Group Study II (RASCAL II) on more than 3000 patients with CRCs, particularly in patients with higher stage [22]. Conversely, negative results were reported by Roth et al. [23]. In our results, the relationship between DW-MRI-derived parameters and KRAS mutant status indirectly confirmed the potential relationship between KRAS mutation and prognosis in rectal cancer.

The KRAS oncogene is one of the important effectors in EGFR signalling pathways, located in chromosome 12 p12. 1 and ultimately controlling processes such as cell growth and survival [24]. The incidence of KRAS mutation in the present study is 25.5%, slightly lower than that in previous studies [3, 4]. This is possibly due to several factors including the limited study sample size and only patients with rectal cancer being enrolled in study. Up to 90% of activating KRAS mutations

were detected in codons 12 and 13 [24]. In our study, there were eight codon 12 mutations and five codon 13 mutations. It is intriguing that specific KRAS mutations may be heterogeneous in their phenotype. For example, Bazanet et al, [25] found that KRAS codon 12 mutations were associated with a mucinous phenotype of CRC as well as more aggressive tumour behaviour with greater metastatic potential [26]. However, the values of DW-MRI-derived parameters between the codon 12 and codon 13 subgroup showed no statistical differences. Considering the limited sample size and multiple alternative genetic pathways in CRC [27], further analysis needs to be performed with much larger patients cohort.

The present study has a number of limitations. First, there were a limited number of patients with rectal cancer in the study; thus, preliminary results by using a relatively small sample size were provided. Second, it is a retrospective study, so unintended selective bias may exist. Third, the f values were not T2 corrected and thus may be impacted by the T2 relaxation times of blood and tissues. Fourth, only KRAS status was investigated in the present study; other mutations in key genes [28], such as APC, CTNNB1 and BRAF, and the potential crosstalk among these mutations were not involved. A meta-analysis showed that patients with CRCs harbouring the BRAF mutation may not benefit from treatment with anti-EGFR antibodies, and the BRAF mutation is an adverse prognostic biomarker for the survival of patients with metastatic CRC [29]. Therefore, further BRAF testing should be recommended for rectal cancers with wild-type KRAS, which is beyond the scope of the current study.

In conclusion, the DW-MRI-derived parameters, specifically Mean-ADC and D^* , showed moderate diagnostic performance in differentiating rectal cancers with different KRAS mutant statuses from wild type in rectal cancer, suggesting potential for predicting the genotype of rectal cancer (KRAS mutant/wild type).

Funding This work was supported by grants from the National Natural Science Foundation of China (no. 81501469) and the Health Industry Special Scientific Research Project of the National Health and Family Planning Commission of the People's Republic of China (no. 201402019).

Compliance with ethical standards

Guarantor The scientific guarantor of this publication is Dr. Hongliang Sun.

Conflict of interest The authors of this manuscript declare no relationships with any companies, whose products or services may be related to the subject matter of the article.

Statistics and biometry One of the authors has significant statistical expertise.

No complex statistical methods were necessary for this paper.

Informed consent Written informed consent was waived in this study.

Ethical approval Institutional Review Board approval was obtained.

Methodology

- retrospective
- observational
- performed at one institution

References

1. Weitz J, Koch M, Debus J, Höhler T, Galle PR, Büchler MW (2005) Colorectal cancer. *Lancet* 365:153–165
2. Migliore L, Migheli F, Spisni R, Coppedè F (2011) Genetics, cytogenetics, and epigenetics of colorectal cancer. *J Biomed Biotechnol*. 2011:792362
3. Brand TM, Wheeler DL (2012) KRAS mutant colorectal tumors: past and present. *Small GTPases* 3:34–39
4. Wang HL, Lopategui J, Amin MB, Patterson SD (2010) KRAS mutation testing in human cancers: The pathologist's role in the era of personalized medicine. *Adv Anat Pathol* 17:23–32
5. NCCN Clinical Practice Guidelines in Oncology: Colon Cancer (2016)-NCCN Evidence Blocks. National Comprehensive Cancer Network Web site. http://www.nccn.org/professionals/physician_gls/pdf/colon.pdf. Published February 8, 2016.
6. NCCN Clinical Practice Guidelines in Oncology: Rectal Cancer (2016)\ National Comprehensive Cancer Network Web site. http://www.nccn.org/professionals/physician_gls/pdf/rectal.pdf. Published November 4, 2015.
7. Bae H, Yoshida S, Matsuoka Y et al (2014) Apparent diffusion coefficient value as a biomarker reflecting morphological and biological features of prostate cancer. *Int Urol Nephrol* 46:555–561
8. Higano S, Yun X, Kumabe T et al (2006) Malignant astrocytic tumors: clinical importance of apparent diffusion coefficient in prediction of grade and prognosis. *Radiology* 241:839–846
9. Curvo-Semedo L, Lambregts DM, Maas M, Beets GL, Caseiro-Alves F, Beets-Tan RG (2012) Diffusion-weighted MRI in rectal cancer: apparent diffusion coefficient as a potential noninvasive marker of tumor aggressiveness. *J Magn Reson Imaging* 35: 1365–1371
10. Le Bihan D, Breton E, Lallemand D, Aubin ML, Vignaud J, Laval-Jeantet M (1988) Separation of diffusion and perfusion in intravoxel incoherent motion MR imaging. *Radiology* 168:497–505
11. Sun H, Xu Y, Xu Q et al (2017) Rectal cancer: Short-term reproducibility of intravoxel incoherent motion parameters in 3.0T magnetic resonance imaging. *Medicine (Baltimore)* 96:e6866
12. Nougaret S, Vargas HA, Lakhman Y et al (2016) Intravoxel incoherent motion-derived histogram metrics for assessment of response after combined chemotherapy and radiation therapy in rectal cancer: initial experience and comparison between single-section and volumetric analyses. *Radiology* 280:446–454
13. Xiao-ping Y, Jing H, Fei-ping L et al (2016) Intravoxel incoherent motion MRI for predicting early response to induction chemotherapy and chemoradiotherapy in patients with nasopharyngeal carcinoma. *J Magn Reson Imaging* 43:1179–1190
14. Jenkinson MD, du Plessis DG, Smith TS, Brodbelt AR, Joyce KA, Walker C (2010) Cellularity and apparent diffusion coefficient in oligodendroglial tumours characterized by genotype. *J Neuro oncol* 96:385–392
15. Guiu B, Petit JM, Capitan V et al (2012) Intravoxel incoherent motion diffusion-weighted imaging in nonalcoholic fatty liver disease: a 3.0-T MR study. *Radiology* 265:96–103

16. Sun Y, Tong T, Cai S, Bi R, Xin C, Gu Y (2014) Apparent Diffusion Coefficient (ADC) Value: a potential imaging biomarker that reflects the biological features of rectal cancer. *Plos One* 9:e109371
17. Lai V, Li X, Lee VH et al (2014) Nasopharyngeal carcinoma: comparison of diffusion and perfusion characteristics between different tumour stages using intravoxel incoherent motion MR imaging. *Eur Radiol* 24:176–183
18. Jung SH, Heo SH, Kim JW et al (2012) Predicting response to neoadjuvant chemoradiation therapy in locally advanced rectal cancer: diffusion-weighted 3 Tesla MR imaging. *J Magn Reson Imaging* 35:110–116
19. Ward RL, Todd AV, Santiago F, O'Connor T, Hawkins NJ (1997) Activation of the K-ras oncogene in colorectal neoplasms is associated with decreased apoptosis. *Cancer* 79:1106–1113
20. Kobayashi M, Watanabe H, Ajioka Y, Honma T, Asakura H (1996) Effect of K-ras mutation on morphogenesis of colorectal adenomas and early cancers: relationship to distribution of proliferating cells. *Hum Pathol* 27:1042–1049
21. Shigenori K, Miho K, Shuhei T et al (2015) Prognostic value of KRAS and BRAF mutations in curatively resected colorectal cancer. *World J Gastroenterol* 21:1275–1283
22. Andreyev HJ, Norman AR, Cunningham D et al (2001) Kirsten ras mutations in patients with colorectal cancer: the 'RASCAL II' study. *Br J Cancer* 85:692–696
23. Roth AD, Tejpar S, Delorenzi M et al (2010) Prognostic role of KRAS and BRAF in stage II and III resected colon cancer: results of the translational study on the PETACC-3, EORTC 40993, SAKK 60-00 trial. *J Clin Oncol* 28:466–474
24. Downward J (2003) Targeting RAS signaling pathways in the cancer therapy. *Nat Rev Cancer* 3:11–322
25. Bazan V, Agnese V, Corsale S et al (2005) Specific TP53 and/ or K-ras mutations as independent predictors of clinical outcome in sporadic colorectal adenocarcinomas: results of 5-year Gruppo Oncologico dell'Italia Meridionale (GOIM) prospective study. *Ann Oncol* 16:iv50–iv55
26. Li W, Qiu T, Zhi W et al (2015) Colorectal carcinomas with KRAS codon 12 mutation are associated with more advanced tumor stages. *BMC Cancer* 15:340
27. Smith G, Carey FA, Beattie J et al (2002) Proc Natl Acad Sci USA 99:9433–9438. [Mutations in APC, Kirsten-ras, and p53—alternative genetic pathways to colorectal cancer](#)
28. Coppède F, Lopomo A, Spisni R, Migliore L (2014) Genetic and epigenetic biomarkers for diagnosis, prognosis and treatment of colorectal cancer. *World J Gastroenterol* 20:943–956
29. Xu Q, Xu AT, Zhu MM, Tong JL, Xu XT, Ran ZH (2013) Predictive and prognostic roles of BRAF mutation in patients with metastatic colorectal cancer treated with anti-epidermal growth factor receptor monoclonal antibodies: a meta-analysis. *J Dig Dis* 14: 409–416

Quantitative Intravoxel Incoherent Motion Parameters Derived From Whole-Tumor Volume for Assessing Pathological Complete Response to Neoadjuvant Chemotherapy in Locally Advanced Rectal Cancer

Qiaoyu Xu, MD,¹ Yanyan Xu, MD,¹ Hongliang Sun, MD,^{1*} Queenie Chan, PhD,²
Kaining Shi, PhD,³ Aiping Song, MD,⁴ and Wu Wang, MD, PhD¹

Background: Many locally advanced rectal cancer (LARC) patients can benefit from neoadjuvant chemotherapy (NACT), with some achieving a pathological complete response (pCR). However, there is limited research reporting on the value of intravoxel incoherent motion (IVIM) in monitoring pCR in patients with LARC.

Purpose: To identify whether IVIM parameters derived from whole-tumor volume (WTV) before and after NACT could accurately assess pCR in patients with LARC.

Study Type: Prospective patient control study.

Population: Fifty-one patients with LARC before and after NACT, prior to surgery.

Field Strength/Sequence: IVIM-diffusion imaging at 3T.

Assessment: Apparent diffusion coefficient (ADC), slow diffusion coefficient (D), fast diffusion coefficient (D*), and perfusion-related diffusion fraction (*f*) values were obtained on diffusion-weighted magnetic resonance images (DW-MRI) using WTV methods and calculated using a biexponential model before and after NACT.

Statistical Tests: DWI-derived ADC and IVIM-derived parameters and their percentage changes ($\Delta\text{ADC}\%$, $\Delta\text{D}\%$, $\Delta\text{D}^*\%$, and $\Delta f\%$) were compared using independent-samples t-test and Mann-Whitney *U*-test between the pCR and non-pCR groups. The diagnostic performance of IVIM parameters and their percentage changes were evaluated using receiver operating characteristic curves.

Results: Compared with the non-pCR group, the pCR group exhibited significantly lower pre- ADC_{mean} ($P = 0.003$) and pre-D values ($P = 0.024$), and significantly higher post-*f* ($P = 0.002$), $\Delta\text{ADC}_{\text{mean}}\%$ ($P = 0.002$), $\Delta\text{D}\%$ ($P = 0.001$), and $\Delta f\%$ values ($P = 0.017$). Receiver operating characteristic curves showed that the pre-D value had the best specificity (95.12%) and accuracy (86.27%) in predicting the pCR status, and $\Delta\text{D}\%$ had the highest area under the curve (0.832) in assessing the pCR response to NACT.

Data Conclusions: The IVIM-derived D value is a promising tool in predicting the pCR status before therapy. The percentage changes in D values after therapy may help assess the pCR status prior to surgery.

Level of Evidence: 2

Technical Efficacy: Stage 2

J. MAGN. RESON. IMAGING 2018;48:248–258.

Colorectal cancer is the third most commonly diagnosed cancer in men and the second most commonly diagnosed cancer in women worldwide.¹ Approximately one-third of colorectal cancer is located in the rectum, and

View this article online at wileyonlinelibrary.com. DOI: 10.1002/jmri.25931

Received Oct 24, 2017, Accepted for publication Dec 7, 2017.

*Address reprint requests to: H.S., Department of Radiology, China-Japan Friendship Hospital, No. 2 Yinghua East Street, Chaoyang District, Beijing 100029, China. E-mail: stentorsun@gmail.com

From the ¹Department of Radiology, China-Japan Friendship Hospital, Beijing, China; ²Philips Healthcare, Shatin, New Territories, Hong Kong, China; ³Philips Healthcare, Beijing, China; and ⁴Department of Pathology, China-Japan Friendship Hospital, Beijing, China

a fair number of patients are in the locally advanced stage at initial diagnosis. Neoadjuvant chemotherapy (NACT) has been widely applied in treating locally advanced rectal cancer (LARC) for effectively decreasing local recurrence after total mesorectal excision (TME).² Most of the patients can benefit substantially from NACT. After neoadjuvant treatment, approximately 10–30% of LARC patients may achieve a pathological complete response (pCR), which is defined as the absence of viable tumor cells after full pathologic examination of the resected specimen.^{3–6} For these patients, surgical resection may not lead to an increase in overall and disease-free survival, but may result in extensive comorbidities, such as sexual, urinary, and bowel dysfunction, and even mortality.^{7–10} On the contrary, other patients who have a lesser degree of response to therapy may also benefit from early prediction because they can be prevented from ineffectively toxic therapy and alerted for a timely therapeutic regimen. Recently, a paradigm of “nonoperative” or “watch-and-wait” strategy has been proposed for patients with LARC who have a good response to adjuvant therapy.^{10–13} However, there is still a lack of an accurate diagnosis method to predict and identify complete responders without relying on the pathological examination of surgical specimens.^{14,15} Thus, reliable noninvasive diagnostic tools are needed.

Although conventional morphologic magnetic resonance imaging (MRI) can accurately evaluate local invasiveness of the rectal tumor and lymph node metastasis in pretherapeutic patients, restaging after therapy is still challenging.^{14,16,17} The difficulty in distinguishing residual tumor from posttherapeutic fibrosis and edema can potentially lead to overstaging.¹⁸ Diffusion-weighted imaging (DWI) may be helpful in solving this problem. Apparent diffusion coefficient (ADC), the quantitative parameter of DWI, has been used as an imaging marker to evaluate rectal tumor response to therapy.² Several recent studies demonstrated the potential of ADC in distinguishing pCR from non-pCR, but the results remained inconsistent.^{2,19–26} This is possibly because the ADC value could reflect the rate of diffusion in cellular tissues but failed to distinguish the perfusion effects from true tissue diffusion, thereby introducing the signal attenuation of imaging.^{27,28} Intravoxel incoherent motion (IVIM) model, which could estimate tissue perfusion and diffusion components individually using multi-b-values, was introduced to overcome this limitation.^{27,29} It was used in predicting the treatment response of nasopharyngeal carcinoma. The IVIM-derived D values exhibited a higher diagnostic performance compared with ADC values.³⁰

Furthermore, most of the previous studies used a single section of tumor to represent the whole tumor, such as contouring tumor or placing regions of interest (ROIs) on one representative section of tumor.^{21,31,32} However, considering tumor’s heterogeneity, the researchers are subjective in choosing the measurement section, which may result in the

measured deviation. Recently, Nougaret et al³³ used whole-tumor volume (WTV) analyses in assessing the response to chemotherapy and radiation therapy in rectal cancer. They demonstrated better interobserver reproducibility compared with single-section ROI analysis.³³ The WTV analysis method was adopted in the present study for minimizing subjectivity of drawing ROIs on tumors among different observers and obtaining more reliable results. IVIM parameters derived from WTV analysis were not used in assessing the response to NACT therapy in LARC. Therefore, this study aimed to evaluate the utility of IVIM parameters by using WTV analysis in assessing the pCR response to NACT.

Materials and Methods

Patients

This prospective study was approved by the Institutional Review Board of our hospital, and written informed consent was obtained from all patients. A 3Tesla MRI scanner was used for pelvic MRI examination of 179 patients with pathologically proven rectal adenocarcinoma between March 2015 and March 2017. The inclusion criteria were: 1) histologically confirmed rectal adenocarcinoma; 2) LARC (stage IIIA and above) at pre-NACT MRI; 3) pre- and post-NACT MRI, including DWI sequences with 16 b values; 4) neoadjuvant chemotherapy; and 5) surgical resection. A total of 128 patients were excluded for the following reasons: i) lack of NACT treatment ($n = 88$); ii) heavy susceptibility artifact or lack of DWI sequences with 16 b values ($n = 6$); iii) lack of pre- or post-NACT MRI ($n = 15$); or iv) mucinous adenocarcinoma or signet-ring cell carcinoma ($n = 19$). Thus, 51 patients (mean age, 60.2 years; range, 35–79 years), including 41 men (mean age, 60.1 years; range, 35–79 years) and 10 women (mean age, 60.8 years; range, 42–79 years) were enrolled in this study.

The median time intervals were as follows: 94 days (range, 30–202 days) between pre-NACT MRI and surgery; 82 days (range, 28–182 days) between pre- and post-NACT MRI imaging; and 6 days (range, 0–72 days) between post-NACT MRI and surgery. The median time interval between the completion of NACT and surgery was 37 days (range, 5–105 days).

The NACT regimens consisted of oxaliplatin, 5-fluorouracil, and calcium folinate once every 2 weeks. All patients were treated with two to four cycles according to their treatment response and physical situation. The patients in this study did not receive radiation therapy.

MRI

On the day of examination, the patients were asked to fast and were intramuscularly injected with 10 mg anisodamine hydrochloride to prevent intestinal peristalsis 10 minutes before MRI. Pre- and post-NACT MRI was performed on a 3T whole-body scanner (Ingenia, Philips Medical Systems, Best, the Netherlands) with a gradient strength of 45 mT/m and a gradient switching rate of 200 mT/m/ms, using a 16-channel anterior torso dS coil and a 16-channel posterior table dS coil. T₂-weighted (T₂W) imaging was performed in the oblique axial, coronal, and sagittal planes, and 2D sagittal T₂W turbo spin echo (TSE) sequences were

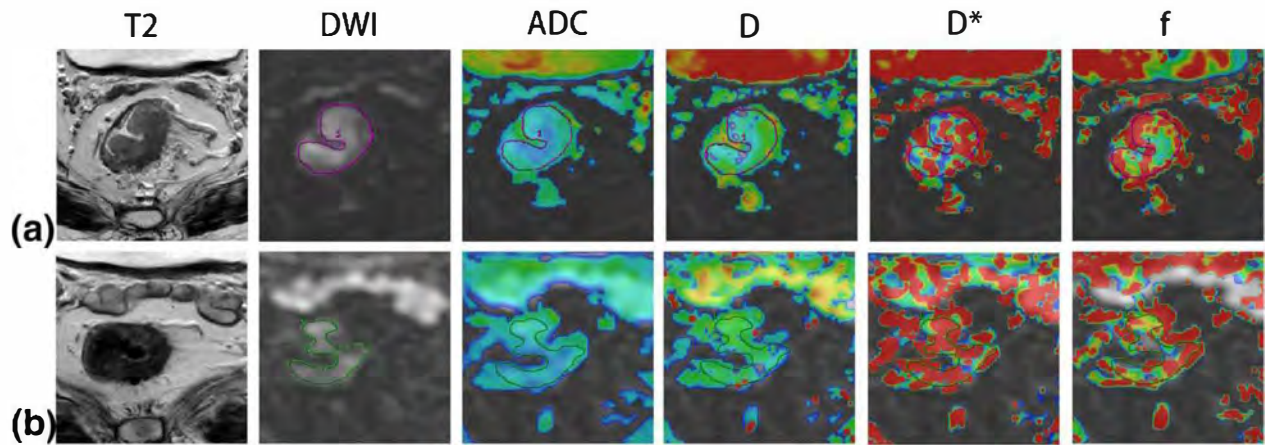


FIGURE 1: A 61-year-old man with LARC from the pCR group (TRG 4). Images in row A are T₂, DWI, ADC, D, D*, and *f* maps before NACT. The ADC, D, D*, and *f* values were $0.840 \times 10^{-3} \text{mm}^2/\text{s}$, $0.804 \times 10^{-3} \text{mm}^2/\text{s}$, $9.321 \times 10^{-3} \text{mm}^2/\text{s}$, and 0.319, respectively. Images in row B are T₂, DWI, ADC, D, D*, and *f* maps after NACT. The ADC, D, D*, and *f* values were $1.270 \times 10^{-3} \text{mm}^2/\text{s}$, $1.094 \times 10^{-3} \text{mm}^2/\text{s}$, $7.460 \times 10^{-3} \text{mm}^2/\text{s}$, and 0.362, respectively.

obtained using the following parameters: repetition time (TR), 4203 msec; echo time (TE), 102 msec; field of view (FOV), $24 \times 24 \text{cm}^2$; slice thickness, 4 mm with a 0.4-mm gap; acquisition matrix, 336×246 ; and NSA, 3. Coronal T₂W TSE sequences were obtained using the following parameters: TR, 4515 msec; TE, 110 msec; FOV, $24 \times 24 \text{cm}^2$; slice thickness, 3 mm with a 0.3-mm gap; acquisition matrix, 336×253 ; and NSA, 3. 2D axial T₂W TSE sequences were obtained perpendicular to the tumoral axis using the sagittal plane³⁴: TR, 5191 msec; TE, 102 msec; FOV, $18 \times 18 \text{cm}^2$; slice thickness, 3.5 mm with a 0.35-mm gap; acquisition matrix, 200×296 ; and NSA, 3.

The DWI pulse sequence was obtained in the same orientation as oblique axial T₂W imaging by using a single-shot echo-planar imaging pulse sequence using the following parameters: echo time / repetition time (TE/TR), 76/4000 msec; field of view (FOV), $40 \times 32 \text{cm}^2$; slice thickness, 6 mm with a 0.6-mm gap; acquisition matrix, 160×104 ; pixel size, $2.5 \times 3.12 \text{mm}^2$; NSA, 3; and 16 b values (0, 10, 20, 30, 40, 60, 80, 100, 150, 200, 400, 800, 1000, 1200, 1500, and 2000 s/mm²). The frequency selection plus inversion recovery fat-suppression technique (spectral attenuated inversion recovery) was used in the DWI sequence. The scan time for DWI sequence was about 5 minutes.

Image Analysis

Conventional scan sequences were used for radiological diagnosis by morphological evaluation of parameters, such as the depth of invasion and lymph node involvement.

MatLab (MathWorks, Natick, MA) was used to analyze the raw data from diffusion-weighted images. The ADC was obtained using b values fitted to a monoexponential model, whereas IVIM parameters were calculated with a biexponential model using 16 b values (0–2000 s/mm²) described by Le Bihan et al.²⁹

$$Sb/S0 = (1-f) \exp(-bD) + f \exp(-bD^*)$$

where *Sb* is the signal intensity in the pixel with diffusion gradient *b*; *S0* is the mean signal intensity in the pixel without diffusion gradient; *D* (given in units of $\times 10^{-3} \text{mm}^2/\text{s}$) is the diffusion

coefficient of slow or nonperfusion-related diffusion, which represents true molecular diffusion; *D** (given in units of $\times 10^{-3} \text{mm}^2/\text{s}$) is the diffusion coefficient of fast or perfusion-related diffusion; and *f* (given as a percentage) is the perfusion-related diffusion fraction, which represents fractional volume occupied in the voxel by flowing spins.

For each patient, ROIs were manually drawn to contour the border of the rectal cancers on each slice (DWI images, $b = 800 \text{ s/mm}^2$) of tumor with reference to the T₂W image before and after NACT, avoiding the inclusion of intestinal gas, liquid, and necrotic regions (those showing fluid-like signal characteristics) by two experienced radiologists (10 years and 6 years in gastrointestinal imaging) blinded to the histopathology results (Figs. 1 and 2). All the parameters were measured twice 2 weeks later by one of the radiologists. When no residual tumor was seen on the post-NACT images obtained with the DWI pulse sequence, tracings were placed on the rectal wall at the prior tumor site.

Percentage changes in ADC, *D*, *D**, and *f* were calculated as follows:

$$\begin{aligned} \Delta ADC\% &= (\text{postADC} - \text{preADC}) / \text{preADC} \times 100 \\ \Delta D\% &= (\text{postD} - \text{preD}) / \text{preD} \times 100 \\ \Delta D^*\% &= (\text{postD}^* - \text{preD}^*) / \text{preD}^* \times 100 \\ \Delta f\% &= (\text{postf} - \text{pref}) / \text{pref} \times 100 \end{aligned}$$

where preADC, postADC, preD, postD, preD*, postD*, pref, and postf refer to ADC, *D*, *D**, and *f* values before and after NACT, respectively.

Surgical Resection and Histopathological Examination

All patients underwent TME. One experienced gastrointestinal pathologist (9 years of experience) assessed the surgical resection specimens according to the TNM staging system of the 7th edition of the American Joint Committee on Cancer.³⁵ The degree of tumor differentiation was categorized as highly, moderately, and poorly differentiated according to the WHO classification system.³⁶ The tumor response to NACT was evaluated according to tumor regression grade (TRG) system proposed by Dworak et al.³⁷

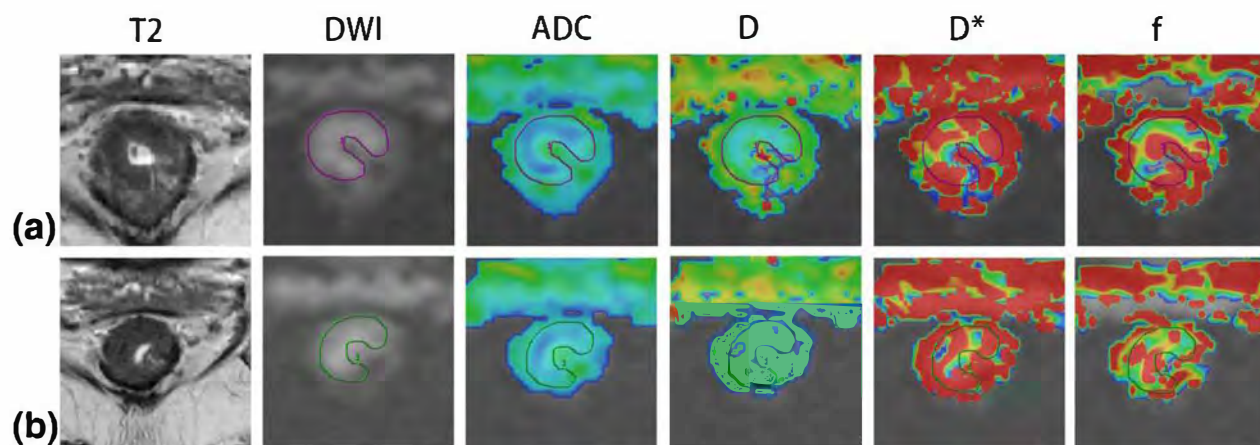


FIGURE 2: A 75-year-old man with LARC from the non-pCR group (TRG 2). Images in row A are T₂, DWI, ADC, D, D*, and *f* maps before NACT. The ADC, D, D*, and *f* values were $1.140 \times 10^{-3} \text{mm}^2/\text{s}$, $0.811 \times 10^{-3} \text{mm}^2/\text{s}$, $11.384 \times 10^{-3} \text{mm}^2/\text{s}$, and 0.320, respectively. Images in row B are T₂, DWI, ADC, D, D*, and *f* maps after NACT. The ADC, D, D*, and *f* values were $1.180 \times 10^{-3} \text{mm}^2/\text{s}$, $0.852 \times 10^{-3} \text{mm}^2/\text{s}$, $10.539 \times 10^{-3} \text{mm}^2/\text{s}$, and 0.313, respectively.

Patients with TRG grades 0–3 were put into the no-pCR group, whereas patients with TRG 4 were put into the pCR group.

Statistical Analysis

The one-sample Kolmogorov–Smirnov test was first used to analyze continuous variables for normality. Continuous variables were expressed as mean ± standard deviation (normal distribution) or median ± interquartile range (abnormal distribution). The intra-class correlation coefficient (ICC) was calculated to evaluate intra- and interobserver reproducibility. ICC values smaller than 0.4 indicated poor reproducibility, values ranging from 0.4 to 0.59 indicated fair reproducibility, values ranging from 0.6 to 0.74 indicated good reproducibility, and values above 0.75 indicated excellent reproducibility. Independent-samples *t*-test and Mann–Whitney *U*-test were employed to estimate the differences in continuous variables between pCR and non-pCR groups. The paired *t*-test was used to compare the parameters between pre-NACT and post-NACT. The diagnostic accuracy of indicators (pre-ADC_{mean}, pre-D, post-*f*, ΔADC_{mean}%, ΔD%, and Δ*f*%) was evaluated in terms of sensitivity, specificity, positive predictive value (PPV), negative predictive value (NPV), and area under the receiver operating characteristic (ROC) curve (AUC). A two-tailed test pattern was used in all statistical analyses with the level of statistical significance determined as *P* < 0.05. All statistical calculations were performed using SPSS (17.0 for Windows, SPSS, Chicago, IL).

Results

Clinical Characteristics

This study was performed on 51 patients with rectal cancer, including 41 men (80.4%) and 10 women (19.6%) who conformed to the selection criteria. Ten patients (pCR rate, 19.6%) had pCR to NACT, and 41 patients had no pCR to NACT. Table 1 summarizes the clinicopathological characteristics of the patients.

Parameters Before and After NACT

The ADC_{min} (*P* = 0.020), ADC_{mean} (*P* = 0.001), and D (*P* < 0.001) values were significantly higher after NACT,

f (*P* = 0.004) values were significantly lower after NACT, whereas ADC_{max} and D* values did not significantly change (*P* = 0.563 and 0.451, respectively) in the pCR group. In non-pCR group, only ADC_{min} values (*P* = 0.004) were significantly higher after NACT, whereas ADC_{max}, ADC_{mean}, D, D*, and *f* values did not significantly change after NACT (*P* = 0.242, 0.205, 0.266, 0.269, and 0.309, respectively) (Table 2, Fig. 3).

Comparison of Parameters Between pCR and Non-pCR groups

The values of pre-ADC_{mean} and pre-D in the pCR group were much lower than that in the non-pCR group (*P* = 0.003 and 0.024, respectively), whereas no significant differences were found in the values of pre-ADC_{min}, pre-ADC_{max}, pre-D*, and pre-*f* (*P* = 0.569, 0.245, 0.687, and 0.448, respectively). Significant differences in post-*f* values were found (*P* = 0.002), whereas no significant differences in other post-NACT parameters were found, including post-ADC_{min}, post-ADC_{mean}, post-ADC_{max}, post-D, and post-D* (*P* = 0.151, 0.217, 0.499, 0.063, and 0.831, respectively). The values of ΔADC_{mean}%, ΔD%, and Δ*f*% were significantly higher in the pCR group than in the non-pCR group (*P* = 0.002, 0.001, and 0.017, respectively); however, no significant difference in the values of ΔADC_{min}%, ΔADC_{max}%, and ΔD*% was observed (*P* = 0.155, 0.868, and 0.618, respectively) (Table 3, Figs. (3 and 4)).

Diagnostic Performance for Assessing pCR

The diagnostic performance of ADC and IVIM-derived parameters were evaluated using the ROC curves to assess a pCR. Pre-ADC_{mean}, pre-D, post-*f*, ΔADC_{mean}%, ΔD%, and Δ*f*% located in the area under the curve were 0.802, 0.732, 0.812, 0.761, 0.832, and 0.746, respectively (Fig. 5). The optimal cutoff value for accurately identifying patients

TABLE 1. Baseline and Demographic Data of 51 Patients

Characteristic	Value
Age (year)	
Male	60.1 (35–79)
Female	60.8 (42–79)
All	60.2 (35–79)
Sex (%)	
Male	41 (80.4%)
Female	10 (19.6%)
Distance of the primary tumor from the anal verge	
0–5.0cm	20 (39.2%)
5.1–10.0cm	27 (52.9%)
10.1–15.0cm	4 (7.8%)
Post-NACT pathologic T(y <p>T) classification</p>	
ypT0	10 (19.6%)
ypT1	2 (3.9%)
ypT2	14 (27.5)
ypT3	25 (49.0%)
ypT4	0 (0%)
Post-NACT pathologic N (ypN) classification	
ypN0	39 (76.5%)
ypN1	10 (19.6%)
ypN2	2 (3.9%)
Tumoral regression grade	
Grade 4	10 (19.6%)
Grade 3	5 (9.8%)
Grade 2	17 (33.3%)
Grade 1	16 (31.4%)
Grade 0	2 (3.9%)
Post-NACT pathological differentiation	
High	5 (12.2%)
Moderate	31 (75.6%)
Poor	5 (12.2%)

Continuous data are expressed as means, with ranges in parentheses. Categorical data are expressed as numbers of patients, with percentages in parentheses.

with pCR was $0.89 \times 10^{-3} \text{mm}^2/\text{s}$ for pre- ADC_{mean} (80% sensitivity, 73.17% specificity, 42.11% PPV, 93.75% NPV, and 74.51% accuracy), $0.58 \times 10^{-3} \text{mm}^2/\text{s}$ for pre-D (50% sensitivity, 95.12% specificity, 71.43% PPV, 88.64% NPV, and 86.27% accuracy), 33.25% for post- f (80% sensitivity, 78.05% specificity, 47.06% PPV, 94.12% NPV, and

TABLE 2. ADC and IVIM Parameters Before and After NACT

Parameters	Before NACT	After NACT	<i>P</i>
ADC_{max}			
pCR	1.59 ± 0.46	1.48 ± 0.23	0.563
non-pCR	1.75 ± 0.42	1.63 ± 0.50	0.242
ADC_{min}			
pCR	0.44 ± 0.21	0.75 ± 0.29	0.020
non-pCR	0.50 ± 0.21	0.66 ± 0.28	0.004
ADC_{mean}			
pCR	0.80 ± 0.18	1.10 ± 0.09	0.001
non-pCR	0.99 ± 0.18	1.05 ± 0.26	0.205
D			
pCR	0.63 ± 0.10	0.82 ± 0.14	<0.001
non-pCR	0.71 ± 0.08	0.74 ± 0.16	0.266
D*			
pCR	9.59 ± 0.84	9.10 ± 1.62	0.451
non-pCR	9.31 ± 1.35	8.98 ± 2.09	0.269
$f(\%)$			
pCR	31.34 ± 1.80	34.64 ± 3.75	0.004
non-pCR	30.69 ± 3.22	29.70 ± 5.95	0.309

Data are presented as mean \pm standard deviation; ADC, apparent diffusion coefficient; D, slow diffusion coefficient; D*, fast diffusion coefficient; and f , perfusion-related diffusion fraction; ADC, D, and D* value = $\times 10^{-3} \text{mm}^2/\text{s}$.

78.43% accuracy), 18% for $\Delta \text{ADC}_{\text{mean}}\%$ (90% sensitivity, 65.85% specificity, 39.13% PPV, 96.43% NPV, and 70.59% accuracy), 23.35% for ΔD (80% sensitivity, 80.49% specificity, 50% PPV, 94.29% NPV, and 80.39% accuracy), -5.31% for Δf (100% sensitivity, 51.22% specificity, 33.33% PPV, 100% NPV, and 60.78% accuracy) (Table 4).

Intra- and Interobserver Repeatability of the Parameters Derived from WTV

No significant intra- and interobserver differences were found in the parameters (D, D*, and f) derived from WTV. All parameters showed excellent reproducibility (Table 5).

Discussion

The present study demonstrated that the pCR group had significantly lower ADC and D values before NACT compared with the non-pCR group, which might help clinicians predict the pCR to NACT in LARC. The percentage changes in ADC, D, and f values before and after NACT were significantly higher in the pCR group, suggesting that ADC, D, and f values

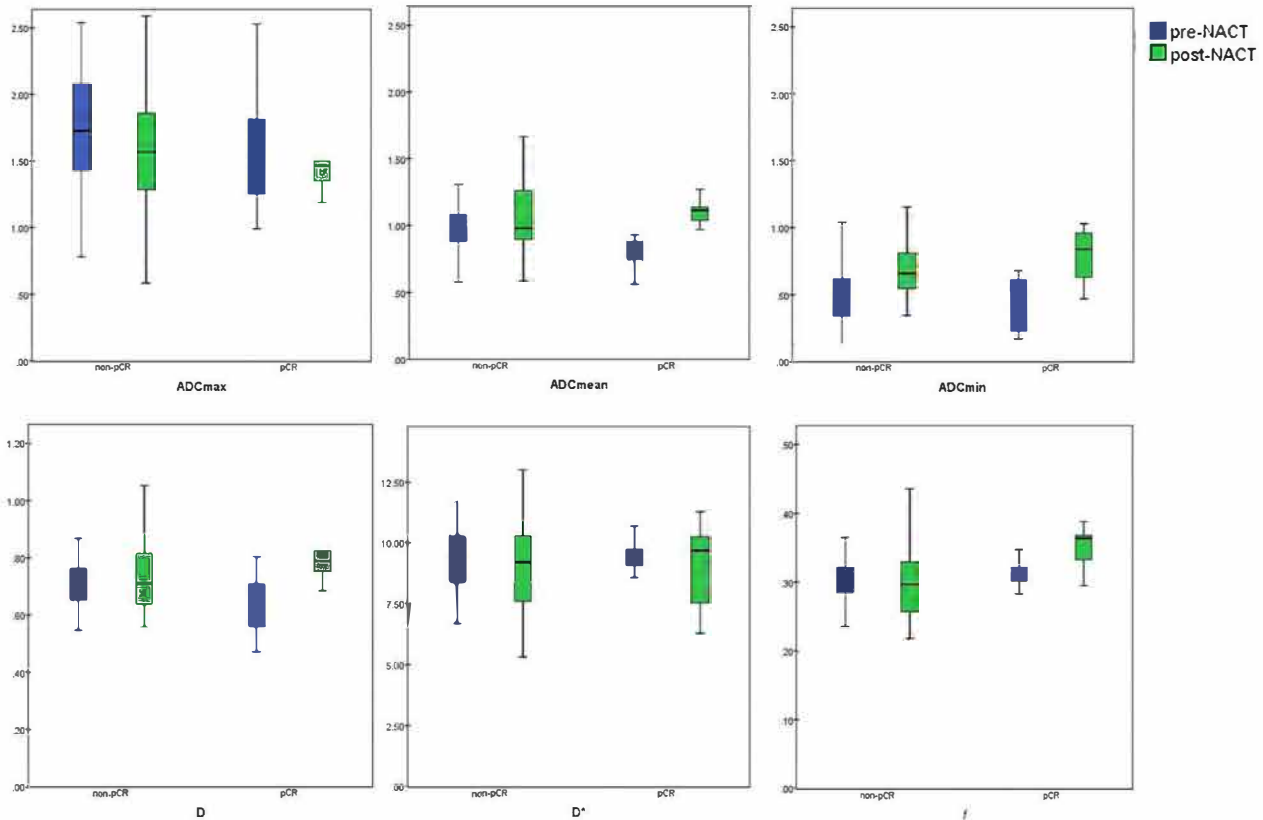


FIGURE 3: Box-and-whisker plots of ADC and IVIM parameters before and after NACT in non-pCR and pCR groups.

might be useful in assessing the pCR response before surgery. In addition, the percentage changes in D values before and after NACT showed the highest diagnostic performance, and D values before therapy showed the best specificity and accuracy among all parameters. The WTV measurement showed excellent reproducibility.

Preoperative pelvic radiation therapy could result in long-term bowel and sexual functional changes.³⁸ Moreover, Schrag et al demonstrated that adding radiation therapy to neoadjuvant chemotherapy could not improve treatment outcomes, but delayed administration of optimal chemotherapy.³⁹ Therefore, patients in this study did not receive radiation therapy. Early prediction of rectal tumor response to therapy can help clinicians choose the optimal treatment regimen, and finding a tool to predict pCR before therapy and assessing it accurately after therapy is important. However, assessing the tumor residual and nodal statuses after therapy was usually limited because the morphologic imaging of tumor was similar to fibrous replacement of the tumor tissues.¹⁸ DWI-derived ADC values were regarded as a reasonable imaging biomarker, which could quantitatively measure random diffusion of water molecules in biologic tissues. The increase in ADC values was related to decreased cellular density and increased interstitial space, which was useful when evaluating the malignancy of the tumor and monitoring the tumor response to treatment.^{22,25,40,41}

However, this technique did not consider the influence of microcirculation perfusion. Therefore, it could not accurately reflect the diffusion characteristics. IVIM DW-MRI could distinguish perfusion information from diffusion using a biexponential model and multi-b-value sampling. Hence, the true molecular diffusion and microcirculation perfusion could be obtained simultaneously.^{27,29} This notion was supported by the results of the present study that IVIM-derived D values were significantly lower than DWI-derived ADC values both before and after NACT, which were also consistent with previous findings in various tumor and organs.⁴²⁻⁴⁴

Furthermore, the ADC and D values were found to be significantly lower before the start of therapy in the pCR group compared with the non-pCR group. Similarly, Lambrecht et al showed that the low ADC values before therapy were significantly associated with the pCR status.²⁶ Perhaps the necrotic area in the tumor could decrease the movement of water molecules and also inhibit the delivery of therapy due to lack of vascularization. Conversely, several studies reported that pretreatment ADC²¹⁻²⁴ and D values^{31,32} were not associated with the pCR status. These differences might be because of the variations in the MRI technique and the difference in measurement methodology such as ROI selection.

In addition, this study found that pre-ADC and pre-D values significantly increased in the pCR group compared with

TABLE 3. Comparison of ADC and IVIM Parameters Before and After NACT Between pCR and Non-pCR Groups

	Parameters	PCR (n = 10)	Non-pCR (n = 41)	P
Pre-NACT	ADC _{max}	1.59 ± 0.46	1.75 ± 0.42	0.245
	ADC _{min}	0.44 ± 0.21	0.50 ± 0.21	0.569
	ADC _{mean}	0.80 ± 0.18	0.99 ± 0.18	0.003
	D	0.63 ± 0.10	0.71 ± 0.08	0.024
	D*	9.59 ± 0.84	9.31 ± 1.35	0.687
	f(%)	31.34 ± 1.80	30.69 ± 3.22	0.448
Post-NACT	ADC _{max}	1.48 ± 0.23	1.63 ± 0.50	0.499
	ADC _{min}	0.75 ± 0.29	0.66 ± 0.28	0.151
	ADC _{mean}	1.10 ± 0.09	1.05 ± 0.26	0.217
	D	0.82 ± 0.14	0.74 ± 0.16	0.063
	D*	9.10 ± 1.62	8.98 ± 2.09	0.831
	f(%)	34.64 ± 3.75	29.70 ± 5.95	0.002
*Δ(%)	ADC _{max}	-9.21 ± 45.37	-7.813 ± 40.12	0.868
	ADC _{min}	91.50 ± 138.22	47.76 ± 114.72	0.155
	ADC _{mean}	42.49 ± 33.63	-1.18 ± 47.15	0.002
	D	36.23 ± 24.30	-0.08 ± 31.65	0.001
	D*	-4.61 ± 33.03	-1.85 ± 24.65	0.618
	f	11.77 ± 12.73	-5.63 ± 28.60	0.017

Data are presented as mean ± standard deviation or median ± interquartile range (*); ADC, apparent diffusion coefficient; D, slow diffusion coefficient; D*, fast diffusion coefficient; and f, perfusion-related diffusion fraction; ADC, D, and D* value = ×10⁻³ mm²/s; Δ(%) = (post-γ-pre)/pre × 100; (γ=ADC_{max}, ADC_{min}, ADC_{mean}, D, D*, or f).

post-ADC and post-D values. It was different from several previous studies that obtained increased ADC values in the pCR and non-pCR groups.^{21,31} Furthermore, several studies showed that posttreatment ADC^{22,32} and D³¹ values could help distinguish pCR from non-pCR in patients with LARC. However, several other studies did not demonstrate this utility.^{23,24} In this study, post-ADC and post-D values were not

found to be significantly different between the two groups. However, the percentage changes in ADC and D before and after NACT were significantly higher in the pCR group than in the non-pCR group. This suggested that these two groups of patients had different sensitivities to NACT. Cytotoxic chemotherapy could more effectively eradicate tumor cells, which was reflected in an increase in ADC and D values.

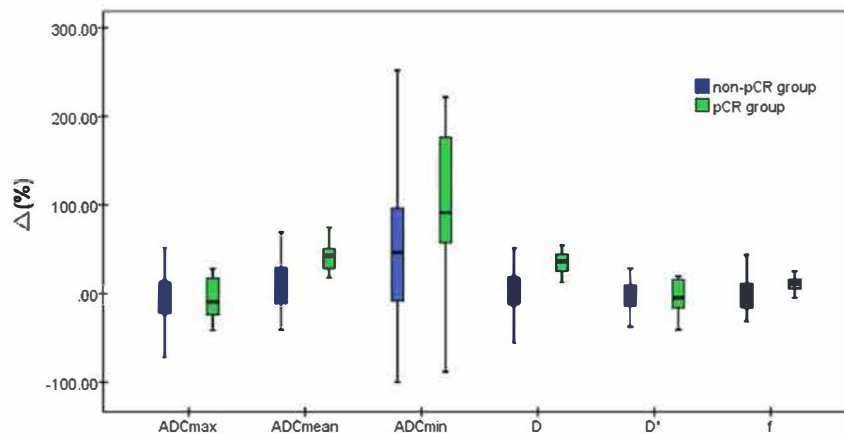


FIGURE 4: The percentage changes of ADC and IVIM parameters before and after NACT in non-pCR and pCR groups.

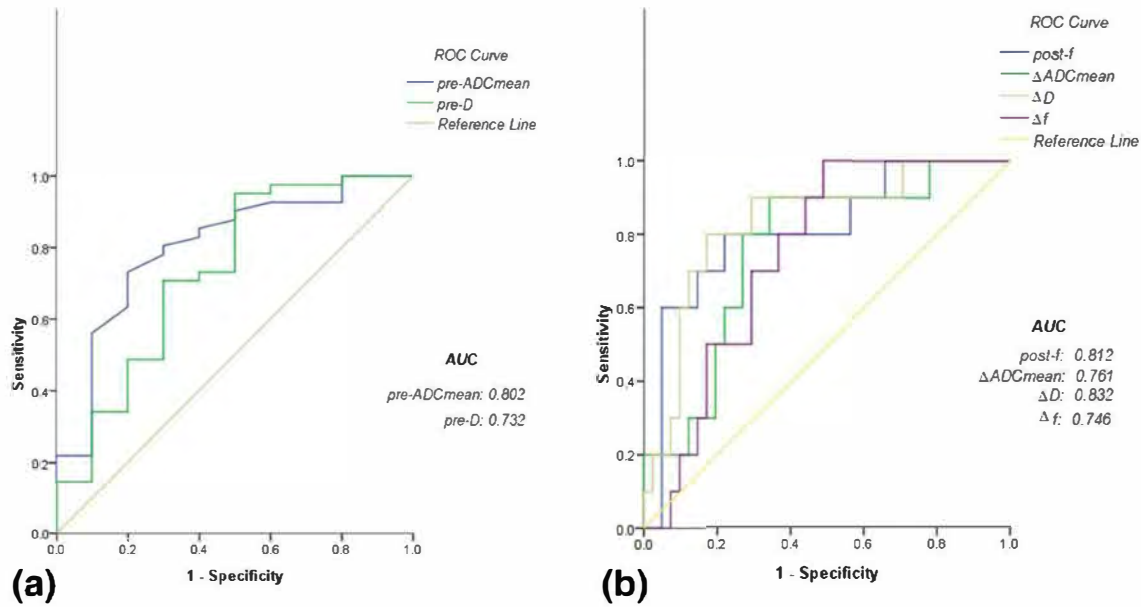


FIGURE 5: (a) ROC curve analysis of pre-ADC_{mean} and pre-D values for predicting pCR. (b) ROC curve analysis of post-f, ΔADC_{mean}, ΔD, and Δf values for assessing pCR.

However, the results of the present study and prior studies might be different because the investigators used various methods of placing ROIs in rectal tumor when evaluating the parameters on DW-MRI. Contouring lesions on a representative section of rectal tumor was the most common and convenient method. However, the distribution of signal intensity in rectal cancer was heterogeneous, and a single section of tumor may not represent the information on tumor heterogeneity.^{19–22,45,46} Moreover, the selection of section and the position of ROIs highly depended on the subjective judgment of different observers. Thus, its accuracy was limited. Recently, Nougaret et al indicated that the WTV analysis of IVIM-derived parameters had better reproducibility than single-section ROI analysis when assessing the treatment response in patients with LARC.³³

Additionally, Goh et al suggested that WTV analysis might improve the assessment of tumor by capturing inherent intratumoral heterogeneity better.⁴⁷ The WTV analysis was adopted in the present study for minimizing sampling bias and obtaining more reliable results. The ADC_{mean} values were significantly different from both ADC_{min} ($P < 0.001$) and ADC_{max} ($P < 0.001$) values, further proving heterogeneity in the tumor. Moreover, the data showed that WTV analysis had excellent reproducibility, which was consistent with the findings of previous studies.³³ The present study showed that the pre-D values had the highest specificity and accuracy when predicting the pCR response and ΔD% had the highest AUC when assessing the pCR status after therapy. This suggested that IVIM-derived D values were significantly associated with pCR.

Parameters	Sensitivity (%)	Specificity (%)	PPV (%)	NPV (%)	Accuracy (%)	AUC (95%CI)	Cutoff value
Pre-ADC _{mean} ($\times 10^{-3} \text{mm}^2/\text{s}$)	80	73.17	42.11	93.75	74.51	0.802 (0.646–0.959)	0.89
Pre-D ($\times 10^{-3} \text{mm}^2/\text{s}$)	50	95.12	71.43	88.64	86.27	0.732 (0.538–0.926)	0.58
Post-f (%)	80	78.05	47.06	94.12	78.43	0.812 (0.658–0.966)	33.25
ΔADC _{mean} (%)	90	65.85	39.13	96.43	70.59	0.761 (0.604–0.918)	18.00
ΔD (%)	80	80.49	50	94.29	80.39	0.832 (0.690–0.973)	23.35
Δf (%)	100	51.22	33.33	100	60.78	0.746 (0.611–0.881)	-5.31

TABLE 5. Intra- and Interobserver Agreement for Whole-Tumor Volume Measurement

	Parameters	Intraobserver	Interobserver
Pre-NACT	ADC _{max}	0.8282	0.7593
	ADC _{min}	0.8812	0.8489
	ADC _{mean}	0.9786	0.9763
	D	0.9507	0.9433
	D*	0.9841	0.9774
	<i>f</i>	0.9660	0.9603
Post-NACT	ADC _{max}	0.7939	0.7550
	ADC _{min}	0.8017	0.7538
	ADC _{mean}	0.8807	0.8633
	D	0.9863	0.9836
	D*	0.9657	0.7949
	<i>f</i>	0.9582	0.9669

In addition, the results of *f* values in assessing the treatment response were variable across different studies. Lu et al found that pre-*f* values were significantly higher in the pCR group of rectal cancer,³¹ whereas other studies found that *f* values were not useful in assessing the treatment response in rectal tumor.^{32,33} These conflicting results might be due to the fact that *f* values represented the signal intensity ratio of blood capillaries and tumor tissues, which were both affected by the T₂ contribution.^{48,49} After treatment, the T₂ values of tumor tended to increase, leading to an underestimation of the increase in *f* values.⁴⁹ In the present study, post-*f* values and its percentage changes significantly increased after NACT in the pCR group, whereas no significant changes were found in the non-pCR group. However, the vascular damage and the influence of inflammation and edema were complex, limiting the utility of *f* values.⁵⁰ Therefore, although *f* values showed the highest sensitivity (100%) in the present study, the results still should be interpreted with caution.

The present study demonstrated that IVIM-derived D* values were useless in predicting or identifying pCR response. Similarly, Zhu et al did not find a significant difference in D* values between the two groups.³² Moreover, Yu et al proved that IVIM-derived diffusion parameters might be more helpful than IVIM-derived perfusion parameters in patients with nasopharyngeal carcinoma.³⁰ However, Lu et al reported higher pre-D* in the pCR group of rectal cancer. These conflicting results were possibly due to the poor reproducibility of D* values,^{32,33} which was also proved in the present study showing that the interobserver agreement of D* values after NACT was lower than that of

other parameters. This might also result from the relatively high sensitivity of D* values to noise.⁵¹

The present study had several limitations. First, the sample size was relatively small and confined to a single center, resulting in selection bias. Second, different timepoints of therapy were not taken into account. Further studies could monitor the parameters after every cycle of chemotherapy to obtain more information in predicting or assessing pCR. Third, the results were not compared with the dynamic contrast material-enhanced acquisition parameters, which could quantitatively assess tumor microcirculation after therapy directly. Fourth, in our study we excluded rectal mucinous adenocarcinoma, which is seen as abundant extracellular mucin exceeding 50% of the tumor stroma.⁵² However, the diffusion and perfusion characteristics of mucinous adenocarcinoma in DWI-derived images were different from typical rectal adenocarcinoma⁵³ and accumulating evidence indicates that the prognosis of mucinous adenocarcinoma is poorer than nonmucinous adenocarcinoma.^{54,55} Finally, the IVIM model required sufficient b values, but too many b values would increase the scan time. Therefore, the proper number and interval of b values need to be explored.

In conclusion, this study suggested that IVIM-derived D values before therapy might be a promising tool for predicting pCR, and the percentage changes in D values after therapy had the best diagnostic performance of pCR response. These results still need to be proved by conducting larger, multicenter, prospective studies. Furthermore, the WTV analysis showed excellent reproducibility, which can be applied in further studies for obtaining reliable results.

Conflict of Interest

Queenie Chan and Kaining Shi are employees of Philips Healthcare but they had no control over inclusion of any data or information that might have presented a conflict of interest. There are no actual or potential conflicts of interest to declare in relation to this article. The other authors have nothing to disclose.

Acknowledgment

Contract grant sponsor: National Natural Science Foundation of China; contract grant number: 81501469; Contract grant sponsor: Health Industry Special Scientific Research Project of National Health and Family Planning Commission of the People's Republic of China; contract grant number: 201402019

References

1. Torre LA, Bray F, Siegel RL, Ferlay J, Lortet-Tieulent J, Jemal A. Global cancer statistics, 2012. *CA Cancer J Clin* 2015;65:87–108.

2. Hötter AM, Garcia-Aguilar J, Gollub MJ. Multiparametric MRI of rectal cancer in the assessment of response to therapy. *Dis Colon Rectum* 2014;57:790–799.
3. Yeo S, Kim DY, Kim TH, et al. Pathologic complete response of primary tumor following preoperative chemoradiotherapy for locally advanced rectal cancer. *Ann Surg* 2010;252:998–1004.
4. Wallin U, Rothenberger D, Lowry A, Luepker R, Mellgren A. CEA — A predictor for pathologic complete response after neoadjuvant therapy for rectal cancer. *Dis Colon Rectum* 2013;56:859–868.
5. Habrgama A, Perez R, Nadalin W, et al. Long-term results of preoperative chemoradiation for distal rectal cancer correlation between final stage and survival. *J Gastrointest Surg* 2005;9:90–101.
6. Wheeler JMD, Dodds E, Warren BF, et al. Preoperative chemoradiotherapy and total mesorectal excision surgery for locally advanced rectal cancer: correlation with rectal cancer regression grade. *Dis Colon Rectum* 2004;47:2025–2031.
7. Pozo ME. Watch and wait approach to rectal cancer: A review. *World J Gastrointest Surg* 2015;7:306.
8. Kim M, Kim ES, Yeo S. Definitive high-dose radiotherapy with concurrent chemotherapy for locally advanced rectal cancer. *Medicine* 2016; 95:e5059.
9. Camilleri-Brennan J, Steele RJ. Objective assessment of morbidity and quality of life after surgery for low rectal cancer. *Colorectal Dis* 2002;4:61–66.
10. Habr-Gama A, Perez RO, Nadalin W, et al. Operative versus nonoperative treatment for stage 0 distal rectal cancer following chemoradiation therapy. *Ann Surg* 2004;240:711–718
11. Beets GL, Figueiredo NL, Habr-Gama A, van de Velde CJH. A new paradigm for rectal cancer: Organ preservation. *Eur J Surg Oncol* 2015;41:1562–1564.
12. Habr-Gama A, Perez RO, São Julião GP, Proscurshim I, Gama-Rodrigues J. Nonoperative approaches to rectal cancer: a critical evaluation. *Semin Radiat Oncol* 2011;21:234–239.
13. Maas M, Beets-Tan RG, Lambregts DM, et al. Wait-and-see policy for clinical complete responders after chemoradiation for rectal cancer. *J Clin Oncol* 2011;29:4633–4640.
14. Habr-Gama A, Gama-Rodrigues J, São Julião GP, et al. Local recurrence after complete clinical response and watch and wait in rectal cancer after neoadjuvant chemoradiation: impact of salvage therapy on local disease control. *Int J Radiat Oncol Biol Phys* 2014;88:822–828.
15. Habrgama A, Perez R, Proscurshim I, et al. Patterns of failure and survival for nonoperative treatment of stage c0 distal rectal cancer following neoadjuvant chemoradiation therapy. *J Gastrointest Surg* 2006;10:1319–1329.
16. Suppiah A, Hunter IA, Cowley J, et al. Magnetic resonance imaging accuracy in assessing tumour down-staging following chemoradiation in rectal cancer. *Colorectal Dis* 2009;11:249–253.
17. van der Paardt MP, Zagers MB, Beets-Tan RG, Stoker J, Bipat S. Patients who undergo preoperative chemoradiotherapy for locally advanced rectal cancer restaged by using diagnostic MR imaging: a systematic review and meta-analysis. *Radiology* 2013;269:101–112.
18. Beets-Tan RG, Beets GL, Vliegen RF, et al. Accuracy of magnetic resonance imaging in prediction of tumour-free resection margin in rectal cancer surgery. *Lancet* 2001;357:497–504.
19. Choi MH, Oh SN, Rha SE, et al. Diffusion-weighted imaging: Apparent diffusion coefficient histogram analysis for detecting pathologic complete response to chemoradiotherapy in locally advanced rectal cancer. *J Magn Reson Imaging* 2016;44:212–220.
20. Kim SH, Lee JM, Hong SH, et al. Locally advanced rectal cancer: added value of diffusion-weighted MR imaging in the evaluation of tumor response to neoadjuvant chemo- and radiation therapy. *Radiology* 2009;253:116–125.
21. Hu F, Tang W, Sun Y, et al. The value of diffusion kurtosis imaging in assessing pathological complete response to neoadjuvant chemoradiation therapy in rectal cancer: a comparison with conventional diffusion-weighted imaging. *Oncotarget* 2017 [Epub ahead of print].
22. Kim SH, Lee JY, Lee JM, Han JK, Choi BI. Apparent diffusion coefficient for evaluating tumour response to neoadjuvant chemoradiation therapy for locally advanced rectal cancer. *Eur Radiol* 2011;21:987–995.
23. Engin G, Sharifov R, Gural Z, et al. Can diffusion-weighted MRI determine complete responders after neoadjuvant chemoradiation for locally advanced rectal cancer? *Diagn Interv Radiol* 2012;574–581.
24. Curvo-Semedo L, Lambregts DM, Maas M, et al. Rectal cancer: assessment of complete response to preoperative combined radiation therapy with chemotherapy—conventional MR volumetry versus diffusion-weighted MR imaging. *Radiology* 2011;260:734–743.
25. Ha HI, Kim AY, Yu CS, Park SH, Ha HK. Locally advanced rectal cancer: diffusion-weighted MR tumour volumetry and the apparent diffusion coefficient for evaluating complete remission after preoperative chemoradiation therapy. *Eur Radiol* 2013;23:3345–3353.
26. Lambrecht M, Vandecaveye V, De Keyser F, et al. Value of diffusion-weighted magnetic resonance imaging for prediction and early assessment of response to neoadjuvant radiochemotherapy in rectal cancer: preliminary results. *Int J Radiat Oncol Biol Phys* 2012;82:863–870.
27. Iima M, Le Bihan D. Clinical intravoxel incoherent motion and diffusion MR imaging: past, present, and future. *Radiology* 2016;278:13–32.
28. Buijssen J, van Stiphout RG, Menheere PPCA, Lammering G, Lambin P. Blood biomarkers are helpful in the prediction of response to chemoradiation in rectal cancer: A prospective, hypothesis driven study on patients with locally advanced rectal cancer. *Radiother Oncol* 2014;111:237–242.
29. Le Bihan D, Breton E, Lallemand D, Aubin ML, Vignaud J, Laval-Jeantet M. Separation of diffusion and perfusion in intravoxel incoherent motion MR imaging. *Radiology* 1988;168:497–505.
30. Xiao-ping Y, Jing H, Fei-ping L, et al. Intravoxel incoherent motion MRI for predicting early response to induction chemotherapy and chemoradiotherapy in patients with nasopharyngeal carcinoma. *J Magn Reson Imaging* 2016;43:1179–1190.
31. Lu W, Jing H, Ju-Mei Z, et al. Intravoxel incoherent motion diffusion-weighted imaging for discriminating the pathological response to neoadjuvant chemoradiotherapy in locally advanced rectal cancer. *Sci Rep-UK* 2017;7.
32. Zhu H, Zhang X, Zhou X, et al. Assessment of pathological complete response to preoperative chemoradiotherapy by means of multiple mathematical models of diffusion-weighted MRI in locally advanced rectal cancer: A prospective single-center study. *J Magn Reson Imaging* 2017;46:175–183.
33. Nougaret S, Vargas HA, Lakhman Y, et al. Intravoxel incoherent motion-derived histogram metrics for assessment of response after combined chemotherapy and radiation therapy in rectal cancer: initial experience and comparison between single-section and volumetric analyses. *Radiology* 2016;280:446–454.
34. Brown G, Richards CJ, Newcombe RG, et al. Rectal carcinoma: thin-section MR imaging for staging in 28 patients. *Radiology* 1999;211: 215–222.
35. Edge SB, Compton CC. The American Joint Committee on Cancer: The 7th Edition of the AJCC Cancer Staging Manual and the Future of TNM. *Ann Surg Oncol* 2010;17:1471–1474.
36. World Health Organization Classification of Tumours of the Digestive System. Lyon: International Agency for Research on Cancer (IARC). 2010. p 134–146.
37. Dworak O, Keilholz L, Hoffmann A. Pathological features of rectal cancer after preoperative radiochemotherapy. *Int J Colorectal Dis* 1997; 12:19–23.
38. Bruheim K, Guren MG, Skovlund E, et al. Late side effects and quality of life after radiotherapy for rectal cancer. *Int J Radiat Oncol Biol Phys* 2010;76:1005–1011.

39. Schrag D, Weiser MR, Goodman KA, et al. Neoadjuvant chemotherapy without routine use of radiation therapy for patients with locally advanced rectal cancer: a pilot trial. *J Clin Oncol* 2014;32:513–518.
40. Genovesi D, Filippone A, Ausili Cèfaro G, et al. Diffusion-weighted magnetic resonance for prediction of response after neoadjuvant chemoradiation therapy for locally advanced rectal cancer: Preliminary results of a monoinstitutional prospective study. *Eur J Surg Oncol* 2013;39:1071–1078.
41. Jung SH, Heo SH, Kim JW, et al. Predicting response to neoadjuvant chemoradiation therapy in locally advanced rectal cancer: Diffusion-weighted 3 Tesla MR imaging. *J Magn Reson Imaging* 2012;35:110–116.
42. Woo S, Lee JM, Yoon JH, Joo I, Han JK, Choi BI. Intravoxel incoherent motion diffusion-weighted MR imaging of hepatocellular carcinoma: correlation with enhancement degree and histologic grade. *Radiology* 2014;270:758–767.
43. Joo I, Lee JM, Yoon JH, Jang JJ, Han JK, Choi BI. Nonalcoholic fatty liver disease: intravoxel incoherent motion diffusion-weighted MR imaging—An experimental study in a rabbit model. *Radiology* 2013:122506.
44. Andreou A, Koh DM, Collins DJ, et al. Measurement reproducibility of perfusion fraction and pseudodiffusion coefficient derived by intravoxel incoherent motion diffusion-weighted MR imaging in normal liver and metastases. *Eur Radiol* 2013;23:428–434.
45. Lambregts DMJ, Vandecaveye V, Barbaro B, et al. Diffusion-weighted MRI for selection of complete responders after chemoradiation for locally advanced rectal cancer: a multicenter study. *Ann Surg Oncol* 2011;18:2224–2231.
46. Park MJ, Kim SH, Lee SJ, Jang KM, Rhim H. Locally advanced rectal cancer: added value of diffusion-weighted MR imaging for predicting tumor clearance of the mesorectal fascia after neoadjuvant chemotherapy and radiation therapy. *Radiology* 2011;260:771–780.
47. Goh V, Halligan S, Gharpuray A, Wellsted D, Sundin J, Bartram CI. Quantitative assessment of colorectal cancer tumor vascular parameters by using perfusion CT: influence of tumor region of interest. *Radiology* 2008;247:726–732.
48. Guiu B, Petit JM, Capitan V, et al. Intravoxel incoherent motion diffusion-weighted imaging in nonalcoholic fatty liver disease: a 3.0-T MR study. *Radiology* 2012;265:96–103.
49. Lemke A, Laun FB, Simon D, Stieltjes B, Schad LR. An in vivo verification of the intravoxel incoherent motion effect in diffusion-weighted imaging of the abdomen. *Magn Reson Med* 2010;64:1580–1585.
50. Hauser T, Essig M, Jensen A, et al. Characterization and therapy monitoring of head and neck carcinomas using diffusion-imaging-based intravoxel incoherent motion parameters—preliminary results. *Neuroradiology* 2013;55:527–536.
51. Mazaheri Y, Afaq A, Rowe DB, Lu Y, Shukla-Dave A, Grover J. Diffusion-weighted magnetic resonance imaging of the prostate: improved robustness with stretched exponential modeling. *J Comput Assist Tomogr* 2012;36:695–703.
52. Hanski C. Is mucinous carcinoma of the colorectum a distinct genetic entity? *Br J Cancer* 1995;72:1350–1356.
53. Çolakoglu Er H, Erden A. Mean ADC values discriminate rectal mucinous carcinoma from rectal nonmucinous adenocarcinoma. *Turk J Med Sci* 2017;47:1520–1525.
54. Park JS, Huh JW, Park YA, et al. Prognostic comparison between mucinous and nonmucinous adenocarcinoma in colorectal cancer. *Medicine* 2015;94:e658.
55. Yu SKT, Chand M, Tait DM, Brown G. Magnetic resonance imaging defined mucinous rectal carcinoma is an independent imaging biomarker for poor prognosis and poor response to preoperative chemoradiotherapy. *Eur J Cancer* 2014;50:920–927.

Intravoxel Incoherent Motion MRI of Rectal Cancer: Correlation of Diffusion and Perfusion Characteristics With Prognostic Tumor Markers

Hongliang Sun¹
Yanyan Xu¹
Aiping Song²
Kaining Shi³
Wu Wang¹

Keywords: DWI, intravoxel incoherent motion, MRI, rectal cancer, tumor grading

doi.org/10.2214/AJR.17.18342

Received April 4, 2017; accepted after revision August 25, 2017.

Supported by grants 81501469 from the National Natural Science Foundation of China and 201402019 from the Health Industry Special Scientific Research Project of National Health and Family Planning Commission of the People's Republic of China.

The employment status of K. Shi at Philips Healthcare did not influence the data in this study.

¹Department of Radiology, China-Japan Friendship Hospital, No. 2 Yinghua E St, Chaoyang District, Beijing 100029, China. Address correspondence to H. Sun (stentorsun@gmail.com).

²Department of Pathology, China-Japan Friendship Hospital, Beijing, China.

³Philips Healthcare MR Research Institution, Beijing, China.

WEB

This is a web exclusive article.

AJR 2018; 210:W1–W9

0361–803X/18/2104–W1

© American Roentgen Ray Society

OBJECTIVE. The objective of our study was to evaluate the intravoxel incoherent motion (IVIM)–DWI derived parameters and their relationships with tumor prognostic markers using 3-T MRI in patients with rectal cancer.

SUBJECTS AND METHODS. Fifty-two patients with histopathologically proven rectal cancer who underwent preoperative pelvic MRI were prospectively enrolled in this study. Diffusion and perfusion parameters including the apparent diffusion coefficient (ADC), pure diffusion coefficient, perfusion fraction, and pseudodiffusion coefficient derived from IVIM–DWI were independently measured by two radiologists. Comparisons of IVIM–DWI–derived parameters in patients with different tumor prognostic markers were made using the independent-samples *t* test, ANOVA, and Mann-Whitney *U* test. The correlations between IVIM–DWI–derived parameters and tumor grade and tumor stage were further evaluated using Spearman correlation analysis. Interobserver agreement was evaluated using the intraclass correlation coefficient (ICC).

RESULTS. Excellent interobserver reproducibility was obtained for the IVIM–DWI–derived parameters (range of ICCs with 95% limits of agreement = 0.9309–0.9948, which is narrow). ADC, pseudodiffusion coefficient, and perfusion fraction tended to rise with greater tumor differentiation ($r = 0.520, p < 0.001$; $r = 0.447, p = 0.001$; $r = 0.354, p = 0.010$, respectively). The pure diffusion coefficient and pseudodiffusion coefficient showed a trend of decreasing with increasing tumor stages ($r = 0.479, p < 0.001$; $r = 0.517, p < 0.001$). The group of patients with extramural vascular invasion (EMVI) showed lower pseudodiffusion coefficient values than the group of patients with no EMVI ($p < 0.05$).

CONCLUSION. IVIM–DWI–derived parameters in patients with rectal cancer, especially the pseudodiffusion coefficient, are associated with tumor grade and tumor stage and show statistically significant differences between subjects with EMVI and those without EMVI. IVIM–DWI–derived parameters would be helpful in predicting tumor aggressiveness and prognosis.

Colorectal cancer (CRC) is a malignant tumor with a high morbidity and mortality. There were 1.4 million new cases worldwide in 2012 and approximately 0.7 million patients died of CRC in 2012 [1]. Rectal cancer accounts for approximately 30–35% of CRCs [1, 2]. The prognosis of patients with rectal cancer is closely related to tumor pathologic grade and stage. Higher tumor grade and advanced stage predict poor prognosis [3, 4]. In addition, the clinical treatment also depends on rectal cancer stage. Patients with advanced-stage rectal cancer often require preoperative chemotherapy or chemoradiotherapy [5–7]. Clinical studies have confirmed that neoadjuvant chemoradiation therapy is

effective for downstaging disease and reducing the rate of local recurrence [7, 8]. Therefore, preoperative staging and grading have important clinical significance in the management of rectal cancer.

Tumor markers, such as carcinoembryonic antigen (CEA) and cancer antigen 19-9 (CA19-9) [9, 10], and relevant imaging indicators based on MRI, such as involvement of the circumferential resection margin (CRM) [11, 12] and the presence of extramural vascular invasion (EMVI) [13–15], are also correlated with prognosis. Previous studies have shown that the probability of metastasis within 1 year is 3.7 times higher in rectal cancer patients with MRI-detected EMVI than in those with no EMVI detected on MRI [14].

It has been reported that tumor shape is associated with differentiation of colorectal adenocarcinoma and that the extramural depth of tumor invasion is related to prognostic factors (including tumor differentiation grade) [16–18]; thus, we hypothesized that the range of bowel circumferential invasion might be associated with tumor grade as a prognostic factor. However, the reference standard of tumor grading and staging is evaluation of postoperative pathologic specimens, whereas MRI indicators are relatively subjective with large interobserver variations [19, 20]; therefore, noninvasive quantitative preoperative evaluation methods are needed.

The DWI sequence has been gradually incorporated into the routine MRI protocol because of its proven advantages in tumor detection, tumor characterization, and monitoring of treatment response [21–27]. The apparent diffusion coefficient (ADC) has been proved to be a potential prognostic factor [22–26]. Intravoxel incoherent motion (IVIM) is based on a biexponential mathematical model with multiple b values, noninvasively measuring both the diffusion of free water molecules and the perfusion caused by microcirculation in vivo. The main parameters derived from the biexponential model are the pure diffusion coefficient, the perfusion fraction, and the pseudodiffusion coefficient [28]. Promising results have been reported in the relationship between IVIM parameters and histologic grade and tumor stage of various tumors [29–33]. However, in rectal cancer, research focusing on the relationships between IVIM parameters and clinicopathologic factors is rare [34, 35]. The only study in the literature that we found was by Surov et al. [35]. In that work, a negative relationship between IVIM parameters and tumor differentiation grade was reported. However, considering various factors, such as inconsistent IVIM protocol settings (especially b values), a limited number of subjects, and the use of different built-in analysis software programs by different vendors, further study of the relationship between IVIM parameters and the clinicopathologic factors of rectal cancer is needed. Therefore, the purpose of our study was to investigate the relationship between IVIM-DWI-derived parameters and clinicopathologic prognostic indicators in patients with rectal cancer to evaluate the feasibility of IVIM-DWI as a quantitative method for assessing tumor aggressiveness and predicting prognosis.

Subjects and Methods

Participants

This prospective study was approved by the institutional review board of China-Japan Friendship Hospital, and written informed consent was obtained from all patients. Between August 2013 and August 2014, 118 consecutive patients with rectal cancer confirmed by endoscopic biopsy and with complete clinical data underwent 3-T MRI. The exclusion criteria were as follows: preoperative neoadjuvant chemoradiotherapy ($n = 40$); an interval between surgery and MRI of more than 4 weeks ($n = 15$); non-rectal adenocarcinoma confirmed by postoperative pathologic results (i.e., neuroendocrine tumor [$n = 4$]); poor image quality (i.e., heavy intestinal peristalsis artifacts [$n = 5$]); and the lesion was too small (diameter < 5 mm) or was too difficult to identify on DW images ($n = 2$). A total of 52 patients were involved in the final analysis (Fig. 1). The clinical data of the 52 patients are listed in Table 1. The median interval between the primary staging MRI examination and surgery was 16 days (range, 7–27 days).

Patient Preparation and Imaging Protocol

Patients had a low-residue diet before the MRI examination and fasted on the day of the examination. Intramuscular injection of 10 mg of anisodamine hydrochloride was given to each patient approximately 10 minutes before MRI examination in the injection room to inhibit intestinal peristalsis.

Pelvic MRI scanning was performed on a 3-T whole-body scanner (Ingenia, Philips Healthcare) with a gradient strength of 45 mT/m and a gradient slew rate of 200 mT/m/ms using a 16-channel

anterior torso coil and a 16-channel posterior table coil. Two-dimensional sagittal and coronal T2-weighted turbo spin-echo (TSE) sequences were performed using the following parameters: TR/TE, 3761/110; FOV, 24×24 cm; slice thickness, 3 mm with a 0.3-mm gap; acquisition matrix, 336×252 ; and number of signals averaged (NSA), 3. A 2D axial T2-weighted TSE sequence was performed perpendicular to the long axis of the rectum at the level of the tumor using the following parameters: TR/TE, 3865/100; FOV, 14×14 cm; slice thickness, 3 mm with a 0.3-mm gap; and acquisition matrix, 232×228 .

Axial IVIM scanning was performed perpendicular to the lesion in the same direction as the axial TSE T2-weighted series using a single-shot DWI sequence with the following parameters: TR/TE, 6000/76; FOV, 20×30 cm; slice thickness, 4 mm with a 0.4-mm gap; acquisition matrix, 80×144 ; NSA, 6; and eight b values (0, 25, 50, 75, 150, 400, 800, and 1000 s/mm²). The scanning time of IVIM was approximately 6 minutes 30 seconds.

Image Analysis and Postprocessing

DW images were postprocessed on a workstation (Extended Workspace 4.1, Philips Healthcare) and analyzed using in-house software (IDL, version 6.3, IDL Software) [36]. The ADC was obtained using b values (0–1000 s/mm²) fitted to the monoexponential model. The IVIM parameters—that is, the diffusion coefficient (D), perfusion fraction (f), and pseudodiffusion coefficient (D^*)—were derived from the curve fit of the following equation [28]:

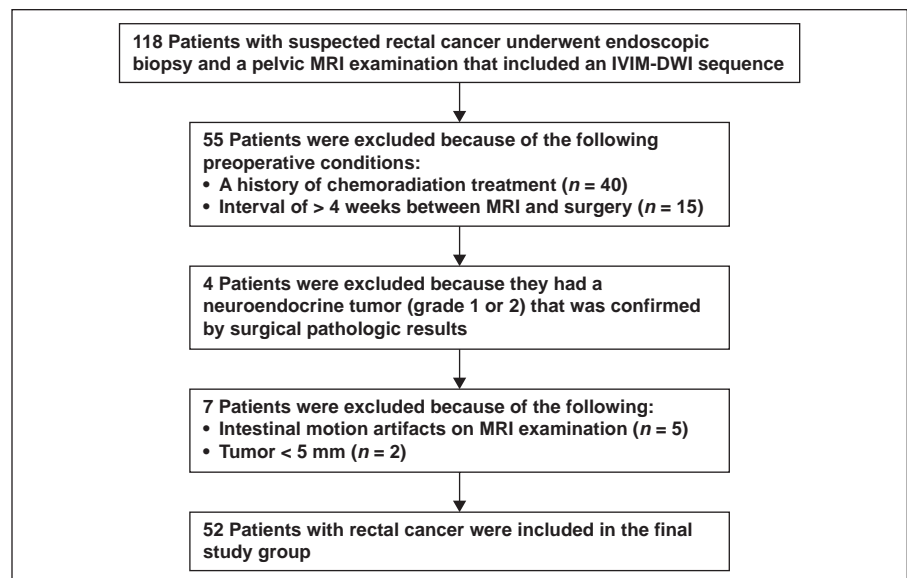


Fig. 1—Flowchart shows subject selection process and exclusion criteria. IVIM = intravoxel incoherent motion.

IVIM-MRI of Rectal Cancer

TABLE 1: Clinicopathologic Factors of 52 Patients With Rectal Cancer

Factors	Value
Age (y), mean ± SD	59.5 ± 13.7
Sex, no. (%) of patients	
Male	30 (57.7)
Female	22 (42.3)
Lesion length (cm), mean ± SD	4.9 ± 1.5
Location ^a , no. (%) of patients	
Upper (> 10 cm)	12 (23.1)
Middle (5–10 cm)	25 (48.1)
Lower (< 5 cm)	15 (28.8)
Tumor grade, no. (%) of patients	
Well differentiated	14 (26.9)
Moderately differentiated	22 (42.3)
Poorly differentiated	16 (30.8)
Tumor stage, no. (%) of patients	
Stage I	17 (32.7)
Stage II	19 (36.5)
Stage III	11 (21.2)
Stage IV	5 (9.6)
Surgical procedure, no. (%) of patients	
Dixon surgery	35 (67.3)
Miles operation	13 (25.0)
Hartmann surgery	4 (7.7)

^aLocation is the distance from the inferior part of the tumor to the anal verge.

$$S_b / S_0 = (1 - f) \exp(-bD) + f \exp(-bD^*),$$

where S_b is the signal intensity at a given b value, S_0 is the signal intensity for a b value of 0 s/mm^2 , and b is the b value. Two experienced radi-

ologists (10 and 8 years' experience in gastrointestinal imaging) who were blinded to the histologic results independently drew the ROI manually on all consecutive tumor slices of the DW images (b value = 1000 s/mm^2). Once the polygonal ROI was drawn along the border of the high-signal-intensi-

ty area comprising the tumor to cover the entire tumor area on images obtained with a b value of 1000 s/mm^2 , the position of the ROI was automatically placed on IVIM parametric maps. All ROIs were carefully defined not to involve necrosis by referring to T2-weighted imaging. The parameters of the ROIs on all slices (mean, 11 ± 3 slices; range, 5–20 slices) were averaged across all pixels in the ROIs (Fig. 2).

The imaging indicators were CRM, EMVI, and bowel circumferential invasion [37]. A positive CRM was defined as a tumor or suspicious lymph node lying within 1 mm of the mesorectal fascia. EMVI was considered positive if a suspicious tumor with intermediate signal intensity within the vessels was located beyond the muscularis propria in the mesorectal fat. Bowel circumferential invasion was assessed in the short axial plane; for this assessment, the bowel was divided into quarters: C1 indicated that the invasion was $\leq 1/4$ of the bowel circumference; C2, $> 1/4$ and $\leq 1/2$ of the bowel circumference; C3, $> 1/2$ and $\leq 3/4$ of the bowel circumference; and C4, $> 3/4$ of the bowel circumference. Two gastrointestinal radiologists who were blinded to the patients' clinical and pathologic information independently reviewed the MRI studies for the status of CRM, EMVI, and bowel circumferential invasion. Discrepancies were resolved at a third analysis session during which a decision was reached by consensus of the two radiologists.

Pathology Evaluation

Surgical pathology results of all patients were analyzed by a pathologist with 6 years' experience in gastrointestinal pathologic diagnosis. Specimens were prepared into 5-mm slices. Then, the pathologic type, tumor differentiation (well differentiated, moderately differentiated, or poorly dif-



Fig. 2—67-year-old man with newly diagnosed poorly differentiated rectal cancer (stage II; location, middle). **A**, Axial T2-weighted image. **B**, DW image obtained using b value of 1000 s/mm^2 shows ROI (1, green outline) of tumor. **C**, Pure diffusion color map shows ROI (1, outline) of tumor.

(Fig. 2 continues on next page)

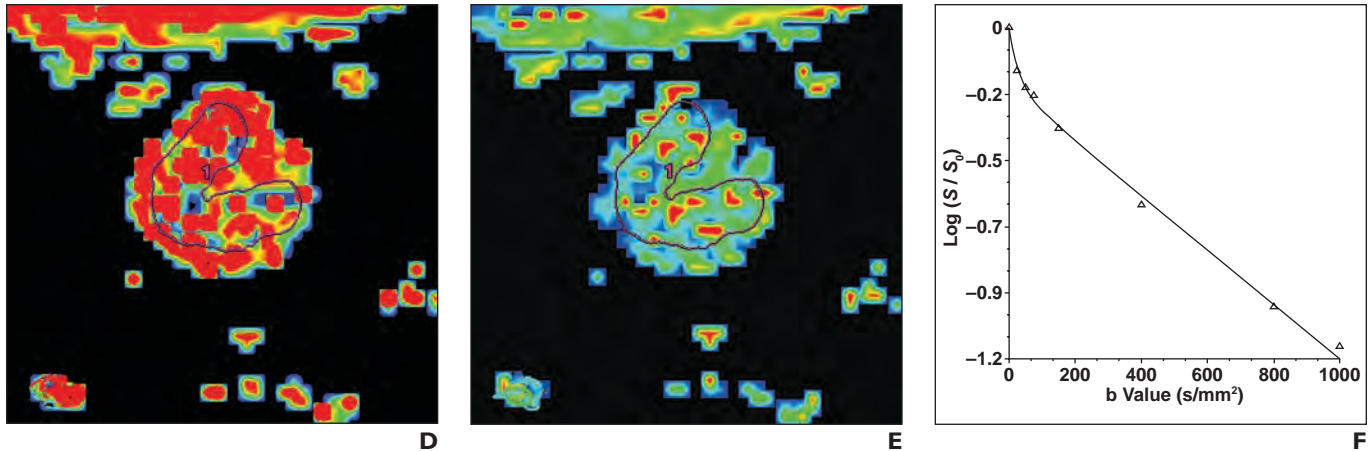


Fig. 2 (continued)—67-year-old man with newly diagnosed poorly differentiated rectal cancer (stage II; location, middle).

D, Pseudodiffusion coefficient color map shows ROI (1, *outline*) of tumor.

E, Perfusion fraction color map shows ROI (1, *outline*) of tumor.

F, Analysis curve based on biexponential model; x-axis shows b values, and y-axis shows logarithm of relative signal intensities, where S is signal intensity and S_0 is signal intensity for b value of 0 s/mm².

ferentiated), tumor stage (according to the 7th edition of the American Joint Committee on Cancer [AJCC] TNM staging system) [38], and the presence of lymph node metastases were evaluated.

Clinical Indicators

Clinical indicators including the plasma levels of CEA and CA19-9 before surgery were recorded. A CEA value of ≥ 5 ng/mL and a CA19-9 value of ≥ 27 U/mL were considered elevated.

Statistical Analysis

Statistical analysis was performed using statistical software (SPSS, version 17.0 for Microsoft Windows, IBM). The reproducibility of IVIM-MRI-derived parameters between different observers was evaluated using intraclass correlation coefficients (ICCs) and Bland-Altman limits of agreement. ICC values less than 0.40 were taken to indicate poor reproducibility, whereas those ranging from 0.40 to 0.59 were considered to indicate fair reproducibility, those ranging from 0.60 to 0.74 to indicate good reproducibility, and those 0.75 or greater to indicate excellent reproducibility. ANOVA analysis was used to compare IVIM-MRI-derived parameters among the various tumor grades, AJCC tu-

mor stages, and bowel circumferential invasion levels (i.e., C1–C4). The relationships between IVIM parameters and pathology results (tumor differentiation degrees and AJCC tumor stages) and bowel circumferential invasion were evaluated through Spearman correlation analysis. Considering the limited number of subjects with stage IV tumors, patients with stage IV tumors and those with stage III tumors were merged to become one group to be analyzed using the ANOVA and Spearman correlation analysis. Independent-samples *t* test and Mann-Whitney *U* test were conducted to test the differences between groups with positive and negative findings for lymph node metastases, normal and elevated CEA values, normal and elevated CA19-9 values, positive and negative CRM, and positive and negative findings for EMVI. A $p < 0.05$ was considered statistically significant.

Results

Interobserver Agreement

Excellent interobserver agreement was obtained for the IVIM-MRI-derived parameters ADC, pure diffusion coefficient, perfusion fraction, and pseudodiffusion coefficient, with ICC values ranging from 0.9309–

0.9767, 0.9844–0.9948, 0.9437–0.9811, and 0.9571–0.9857, respectively. According to Bland-Altman plots, the interobserver 95% limits of consistency of the IVIM-MRI-derived parameters (ADC, pure diffusion coefficient, and pseudodiffusion coefficient) were –8.9% to 9.0%, –11.7% to 9.7%, –14.1% to 11.5%, and –16.7% to 17.8%, respectively.

Correlation Between Intravoxel Incoherent Motion DWI Parameters and Tumor Grades

Fourteen cases of well-differentiated, 22 cases of moderately differentiated, and 16 cases of poorly differentiated tumors were confirmed by the pathology results. IVIM-MRI-derived parameters tended to rise with higher degree of tumor differentiation (Table 2). The ADC, pseudodiffusion coefficient, and perfusion fraction exhibited statistically significant differences ($p < 0.01$, $p < 0.05$, $p < 0.01$, respectively) among different tumor grades and were moderately correlated ($r = 0.520$, $p < 0.001$; $r = 0.447$, $p = 0.001$; and $r = 0.354$, $p = 0.010$, respectively) with tumor grades. The post hoc analysis in ANOVA was

TABLE 2: Intravoxel Incoherent Motion (IVIM) DWI-Derived Parameters of Rectal Cancers by Tumor Grade

IVIM-DWI Parameters	Tumor Grade			<i>p</i>
	Well Differentiated	Moderately Differentiated	Poorly Differentiated	
ADC ($\times 10^{-3}$ mm ² /s)	0.65 \pm 0.09	0.57 \pm 0.07	0.54 \pm 0.10	< 0.01
Pure diffusion coefficient ($\times 10^{-3}$ mm ² /s)	0.79 \pm 0.45	0.75 \pm 0.30	0.74 \pm 0.39	0.92
Perfusion fraction (%)	32.54 \pm 6.91	25.83 \pm 5.90	23.67 \pm 5.69	< 0.01
Pseudodiffusion coefficient ($\times 10^{-3}$ mm ² /s)	91.89 \pm 32.35	73.05 \pm 20.55	67.40 \pm 26.53	< 0.05

Note—Data are shown as mean \pm SD. ADC = apparent diffusion coefficient.

IVIM-MRI of Rectal Cancer

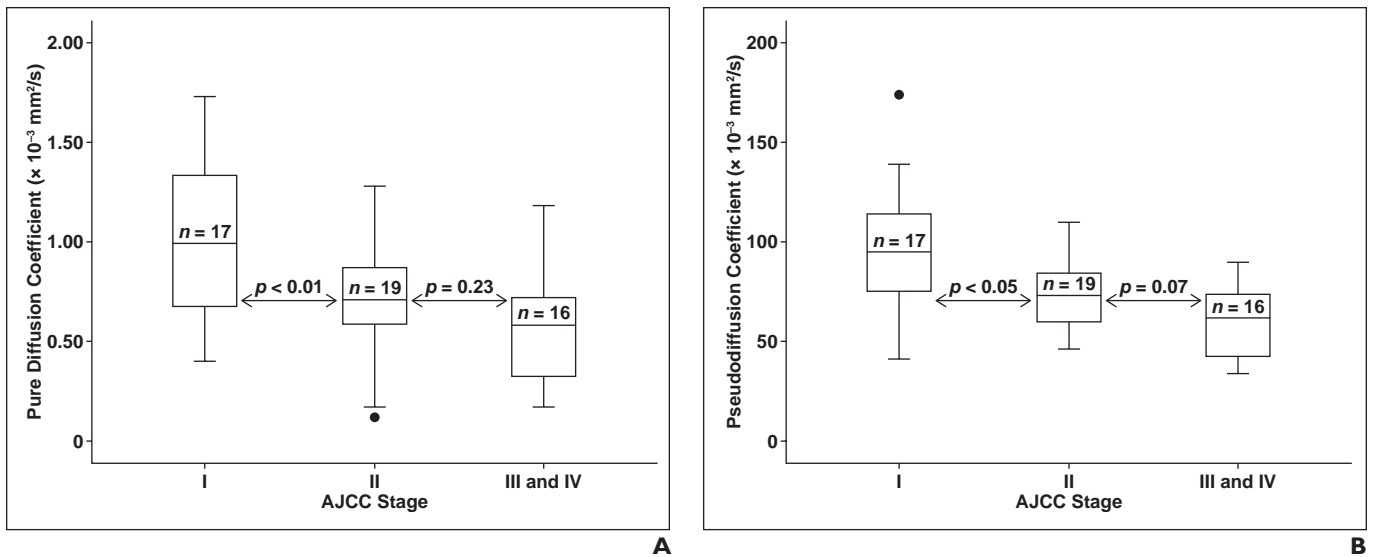


Fig. 3—Box plots.

A and B, Box plots of pure diffusion coefficients (**A**) and pseudodiffusion coefficients (**B**) in different tumor stages according to 7th edition of the American Joint Committee on Cancer (AJCC) TNM staging system [38]. Top and bottom of boxes are first and third quartiles, respectively. Length of box represents interquartile range within which 50% of values were located. Midline within box represents median value. Cross lines above and below mark maximum and minimum values, respectively. Data points (●) outside box are outliers and are smaller than lower quartile minus 1.5 times interquartile range or larger than upper quartile plus 1.5 times interquartile range.

selected to evaluate the differences between subgroups of tumor grade. We found that the ADC value of well-differentiated tumors was higher than that of moderately differentiated ($p < 0.05$) and poorly differentiated ($p < 0.05$) tumors, and similar differences between tumor grades were observed for the pseudodiffusion coefficient values (well differentiated vs moderately differentiated, $p < 0.05$; well differentiated vs poorly differentiated, $p < 0.05$) and perfusion fraction values (well differentiated vs moderately differentiated, $p < 0.01$; well differentiated vs poorly differentiated, $p < 0.001$). However, no significant differences in these parameters were seen between moderately differentiated tumors and poorly differentiated tumors ($p = 0.28$ for ADC, $p = 0.51$ for pseudodiffusion coefficient, and $p = 0.29$ for perfusion fraction).

Correlation Between Intravoxel Incoherent Motion MRI-Derived Parameters and the Presence of Lymph Node Metastases

Lymph node metastases were present in 16 of the 52 patients. Patients with metastases had lower values than patients without metastases for the following parameters: ADC (mean, 0.56 ± 0.07 vs $0.59 \pm 0.10 \times 10^{-3} \text{ mm}^2/\text{s}$), pure diffusion coefficient (0.56 ± 0.29 vs $0.85 \pm 0.36 \times 10^{-3} \text{ mm}^2/\text{s}$), perfusion fraction ($24.35\% \pm 7.16\%$ vs $28.14\% \pm 6.65\%$), and pseudodiffusion coefficient values (59.06 ± 16.44 vs $84.08 \pm 27.74 \times 10^{-3} \text{ mm}^2/\text{s}$).

Significant differences were observed in the pure diffusion coefficient ($p < 0.01$) and pseudodiffusion coefficient ($p < 0.01$).

Correlation Between Intravoxel Incoherent Motion MRI-Derived Parameters and Tumor Stage

Seventeen cases of stage I, 19 cases of stage II, 11 cases of stage III, and five cases of stage IV tumors were confirmed according to the seventh edition of AJCC tumor staging system [38].

The pure diffusion coefficient and pseudodiffusion coefficient showed statistically significant differences among different stages ($p < 0.01$; $p < 0.001$) and were moderately correlated ($r = 0.479$; $r = 0.517$) with different stages. The post hoc analysis using ANOVA was selected to determine the differences between subgroups of tumor stage. We found that the pure diffusion coefficient of stage I tumors was higher than that of stage II tumors ($p < 0.01$) and stage III and IV tumors ($p < 0.01$), but the pure diffusion coefficients showed no significant difference between the latter two subgroups ($p = 0.23$) (Fig. 3A). Similar differences were observed in pseudodiffusion coefficient (stage I vs stage II, $p < 0.05$; stage I vs stages III and IV, $p < 0.05$; stage II vs stages III and IV, $p = 0.07$) between subgroups of tumor stage (Fig. 3B). However, ADC and perfusion fraction values showed no statistically significant differences among the subgroups of tumor stages ($p = 0.33$; $p = 0.26$).

Correlation Between Intravoxel Incoherent Motion MRI-Derived Parameters and Carcinoembryonic Antigen and Cancer Antigen 19-9 Values

There was no statistically significant difference in IVIM-MRI-derived parameters between patients with a normal CEA value ($n = 35$) and those with a high CEA value ($n = 17$), or between patients with a normal CA19-9 value ($n = 41$) and those with a high CA19-9 value ($n = 11$). However, the ADC, pure diffusion coefficient, perfusion fraction, and pseudodiffusion coefficient tended to be lower in patients with a high CEA value and those with a high CA19-9 value than in patients with normal values (Table 3).

Correlation of Intravoxel Incoherent Motion MRI-Derived Parameters With Circumferential Resection Margin, Extramural Vascular Invasion, and Circumferential Involvement

There was no statistically significant difference in IVIM-MRI-derived parameters between groups with positive and negative CRM: ADC, 0.58 ± 0.10 versus $0.59 \pm 0.07 \times 10^{-3} \text{ mm}^2/\text{s}$; pure diffusion coefficient, 0.74 ± 0.38 versus $0.77 \pm 0.37 \times 10^{-3} \text{ mm}^2/\text{s}$; perfusion fraction, $27.71\% \pm 6.94\%$ versus $25.15\% \pm 6.91\%$; and pseudodiffusion coefficient, 74.63 ± 24.66 versus $80.71 \pm 33.42 \times 10^{-3} \text{ mm}^2/\text{s}$. The pseudodiffusion coefficient value of patients with positive EMVI was lower than that in patients with no EMVI ($p <$

TABLE 3: Intravoxel Incoherent Motion (IVIM) DWI-Derived Parameters of Rectal Cancers by Preoperative Plasma Carcinoembryonic Antigen (CEA) Level and Cancer Antigen 19-9 (CA19-9) Level

IVIM-DWI Parameters	High CEA Value (n = 17)	Normal CEA Value (n = 35)	p	High CA19-9 Value (n = 11)	Normal CA19-9 Value (n = 41)	p
ADC ($\times 10^{-3}$ mm ² /s)	0.56 \pm 0.06	0.59 \pm 0.11	0.31	0.58 \pm 0.03	0.58 \pm 0.11	0.78
Pure diffusion coefficient ($\times 10^{-3}$ mm ² /s)	0.67 \pm 0.31	0.80 \pm 0.39	0.22	0.63 \pm 0.29	0.80 \pm 0.38	0.18
Perfusion fraction (%)	24.46 \pm 5.80	28.19 \pm 7.23	0.07	25.00 \pm 7.55	27.50 \pm 6.80	0.54
Pseudodiffusion coefficient ($\times 10^{-3}$ mm ² /s)	71.59 \pm 21.56	78.71 \pm 29.66	0.38	71.90 \pm 21.54	77.59 \pm 78.73	0.55

Note—Data are shown as mean \pm SD. A CEA value of ≥ 5 ng/mL was considered to be high, and a CA19-9 value of ≥ 27 U/mL was considered to be high. ADC = apparent diffusion coefficient.

0.05). There was no statistically significant difference between the patients with EMVI and the patients with no EMVI for the following parameters: ADC (0.57 \pm 0.08 vs 0.59 \pm 0.10 $\times 10^{-3}$ mm²/s), pure diffusion coefficient (0.75 \pm 0.36 vs 0.79 \pm 0.40 $\times 10^{-3}$ mm²/s), and perfusion fraction (27.26% \pm 7.28% vs 26.27% \pm 6.29%). Patients with C1 involvement (n = 2) were grouped with patients with C2 involvement (n = 16) because of the limited number of patients with C1 involvement. There was no statistically significant difference in IVIM-MRI-derived parameters between patients with different levels of bowel circumferential invasion (Table 4).

Discussion

IVIM theory suggests that the signal intensity of DWI comes not only from the diffusion of free water in the intercellular space

but also from the perfusion of the blood capillary network. The diffusion component has a larger weighting factor when a higher b value is used. Sun et al. [22] reported that the ADC value in single-exponential DWI performed with a b value of 800 s/mm² is about 1.20–1.53 $\times 10^{-3}$ mm²/s for rectal adenocarcinoma. Curvo-Semedo et al. [24] reported that the ADC value of rectal tubular adenocarcinoma derived from the single-exponential model with b values of 0, 500, and 1000 s/mm² is about 0.98–1.32 $\times 10^{-3}$ mm²/s. To eliminate the influence of perfusion, Ha et al. [23] used a combination of b values (i.e., 150 and 1000 s/mm²) to calculate the ADC in their work and got an ADC value of 0.43–0.63 $\times 10^{-3}$ mm²/s. These previous studies have indicated that the ADC value in the single-exponential DWI model varies with different b value settings and that ADC values

are not consistent between studies because equipment from different vendors was used [22–26]. The ADC value decreases with higher b values because of the lower perfusion-weighted factor. IVIM theory using the biexponential DWI model not only has the ability to provide the perfusion fraction and pseudodiffusion coefficient as parameters that reflect perfusion but also can provide the pure diffusion coefficient as a parameter of the pure diffusion of free water [28].

Although few applications of IVIM-DWI in patients with rectal cancer have been published in the literature to our knowledge, the ADC value derived from the single-exponential model has already been applied to the grading of rectal cancer with mixed results [22, 24, 25]. No statistically significant difference was observed by Elmi et al. [26], although nonzero b values were used to calcu-

TABLE 4: Intravoxel Incoherent Motion DWI-Derived Parameters of Rectal Cancers by the Status of the Circumferential Resection Margin (CRM), Presence of Extramural Vascular Invasion (EMVI), and Extent of Bowel Circumferential Involvement

Imaging Indicators	ADC ($\times 10^{-3}$ mm ² /s)	p	Pure Diffusion Coefficient ($\times 10^{-3}$ mm ² /s)	p	Perfusion Fraction (%)	p	Pseudodiffusion Coefficient ($\times 10^{-3}$ mm ² /s)	p
CRM ^a		0.81		0.77		0.47		0.23
Positive (n = 15)	0.58 \pm 0.10		0.74 \pm 0.38		27.71 \pm 6.94		74.63 \pm 24.66	
Negative (n = 37)	0.59 \pm 0.07		0.77 \pm 0.37		25.15 \pm 6.91		80.71 \pm 33.42	
EMVI ^b		0.58		0.69		0.65		< 0.05
Positive (n = 17)	0.57 \pm 0.08		0.75 \pm 0.36		27.26 \pm 7.28		70.72 \pm 25.86	
Negative (n = 35)	0.59 \pm 0.10		0.79 \pm 0.40		26.27 \pm 6.29		90.35 \pm 26.39	
Bowel circumferential involvement ^c		0.24		0.63		0.89		0.49
C1 and C2 (n = 18) ^d	0.61 \pm 0.08		0.83 \pm 0.38		27.87 \pm 7.50		83.55 \pm 29.37	
C3 (n = 21)	0.56 \pm 0.11		0.65 \pm 0.37		26.99 \pm 6.94		66.23 \pm 22.31	
C4 (n = 13)	0.59 \pm 0.09		0.84 \pm 0.32		25.71 \pm 6.59		82.85 \pm 28.39	

Note—Data are shown as mean \pm SD. ADC = apparent diffusion coefficient.

^aA positive CRM was defined as a tumor or suspicious lymph node lying within 1 mm of the mesorectal fascia.

^bEMVI was considered positive if a suspicious tumor with intermediate signal intensity within the vessels was located beyond the muscularis propria in the mesorectal fat.

^cC1 indicated that the invasion was $\leq 1/4$ of the bowel circumference; C2, $> 1/4$ and $\leq 1/2$ of the bowel circumference; C3, $> 1/2$ and $\leq 3/4$ of the bowel circumference; and C4, $> 3/4$ of the bowel circumference.

^dPatients with C1 involvement (n = 2) were grouped with patients with C2 involvement (n = 16) because of the limited number of patients with C1 involvement.

late the ADC in another study [30]. That result may have been caused by the mixing of data from different scanners and different b values. Curvo-Semedo et al. [24] have reported that the ADC is lower with less differentiated rectal tumors ($p = 0.025$), and the same trend was evident in the study by Sun et al. [22] but with no statistically significant difference. In our study, the perfusion-related parameters perfusion fraction and pseudodiffusion coefficient showed statistically significant differences between tumor differentiation groups ($F = 8.503, p = 0.001$; $F = 3.635, p = 0.034$) and showed some correlation among differentiation groups ($r = 0.447, p = 0.001$; $r = 0.354, p = 0.010$). Although the pure diffusion coefficient also showed a decreasing trend along with poorer differentiation, there was no statistically significant difference between tumor differentiation groups. These findings confirming that there is no significant difference in water diffusion between tumor differentiation groups are consistent with previous work [39]. A previously reported positive correlation can be explained by the effect of a low b value setting on perfusion [40].

In the current study, the pseudodiffusion coefficient and perfusion fraction increased with greater tumor differentiation. According to IVIM theory [28], the pseudodiffusion coefficient (D^*) is related to perfusion according to the following equation:

$$D^* = (l \times v) / 6,$$

where l means the length of the capillary segment and v is the average velocity of blood in the capillary [41]. According to Le Bihan et al. [28], the perfusion fraction is the partial volume of the whole capillary vascular fraction, and Duong and Kim [40] further suggested that the component of the arterial blood played a more vital role than the venous component for the parameter perfusion fraction at low b values. Thus, the correlation between perfusion-related parameters and tumor differentiation may indicate that the capillary vascular network is relatively well developed in well-differentiated tumors. This result is consistent with previous findings using perfusion CT [42–44]. In poorly differentiated tumors, the tumor cells grow very fast, leading to poor structure of lumenized vessels, which results in less perfusion of the microcirculation. This phenomenon is reflected in lower perfusion-related parameters, such as the pseudodiffusion coefficient and perfusion

fraction, in poorly differentiated tumors. Recent studies have shown some correlation among the pseudodiffusion coefficient, perfusion fraction, and microvessel density in CRC tumors, confirming that IVIM parameters may provide important information for assessing tumor grade and other biologic features in patients with CRC [34, 35]. The TE—that is, the time between giving the radiofrequency pulse and the peak of the echo signal—is a factor that can affect the value of the perfusion fraction [45]. However, this effect would not have any impact on our conclusions because the same TE was used in every patient in our study.

Many studies have focused on the staging of rectal cancer using DWI. Curvo-Semedo et al. [24] reported that there was no correlation between the average ADC value of tumors and T stages or CEA values. On the other hand, Sun et al. [22] observed that ADC values decreased with higher tumor stages. In our study, ADC results showed a similar trend. However, our results also showed that there were statistically significant differences between different stages in both the pure diffusion and pseudodiffusion coefficient values, both of which were negatively correlated with the stages. In addition, the pure diffusion and pseudodiffusion coefficient values of tumors were lower in patients with lymph node metastases than in those without metastases, and similar findings, using ADC values, have been reported not only in rectal cancer [46], but also in nasopharyngeal carcinoma [33]. These results suggest that tumors with lower ADC, pure diffusion, and pseudodiffusion coefficient values might exhibit more aggressive biologic behavior.

The tumor marker level is one of the most important factors affecting prognosis [9, 10]. Although no statistically significant difference in DWI-derived parameters between patients with and those without increased CEA and CA19-9 levels was found in this study, all of these parameters showed a decreasing trend with the rise of CEA and CA19-9 levels. EMVI is an important imaging marker for surgery, because it can indicate that the tumor has broken through the muscularis propria [13–15, 17, 37]. In this study, the pseudodiffusion coefficient was lower in patients with positive EMVI than in those with no EMVI. These results are consistent with other tumor staging data, which also showed that tumors of an advanced stage had lower pseudodiffusion coefficient values. Further research is needed

to evaluate the prognostic value of IVIM-DWI parameters compared with existing tumor markers and other imaging indicators.

Our study had some limitations. One limitation is the selection bias that may have been caused by the fact that patients were limited to those who would undergo surgery without a history of radiation or chemotherapy. Another limitation is the small sample size, especially for some groups. This may be the reason that only a trend has been seen in several correlation analyses, without statistically significant differences. Further work with a larger sample size may reveal more statistically significant results. Third, considering the limited signal-to-noise ratio in DW images, a different slice thickness and gap were adopted for axial T2-weighted images and IVIM sequences. This difference in settings may result in a lack of direct comparison between the two sequences and may limit identification of areas of necrosis slice by slice. Moreover, tumor necrosis would be better observed on contrast-enhanced T1-weighted imaging [47, 48], which was not included in this study, than on T2-weighted imaging. Finally, the way in which the ROIs are drawn is critical in IVIM-DWI because of the huge variations in the parameters [49]: A single small ROI may highlight the extrema, whereas a large ROI can reduce the variation by averaging. The whole-tumor consecutive slices were chosen in this work to balance the representation and variation. Only the biexponential model was used in this work because its feasibility has already been tested widely. The ideal image-processing methodology to describe lesion heterogeneity, such as parameter histogram descriptors, should be explored in future studies.

In conclusion, IVIM parameters showed a decreasing trend with increasing tumor stages and grades in rectal cancer and could possibly provide useful information about diffusion and perfusion, which can be helpful in predicting tumor aggressiveness and prognosis.

References

1. Torre LA, Bray F, Siegel RL, Ferlay J, Lortet-Tieulent J, Jemal A. Global cancer statistics, 2012. *CA Cancer J Clin* 2015; 65:87–108
2. Brenner H, Kloor M, Pox CP. Colorectal cancer. *Lancet* 2014; 383:1490–1502
3. Bown EJ, Lloyd GM, Boyle KM, Miller AS. Rectal cancer: prognostic indicators of long-term outcome in patients considered for surgery. *Int J Colorectal Dis* 2014; 29:147–155
4. Wibe A, Law WL, Fazio V, Delaney CP. Tailored

- rectal cancer treatment: a time for implementing contemporary prognostic factors? *Colorectal Dis* 2013; 15:1333–1342
5. Sebag-Montefiore D, Stephens RJ, Steele R, et al. Preoperative radiotherapy versus selective postoperative chemoradiotherapy in patients with rectal cancer (MRC CR07 and NCIC-CTG C016): a multicentre, randomised trial. *Lancet* 2009; 373:811–820
 6. Sauer R, Becker H, Hohenberger W, et al. Preoperative versus postoperative chemoradiotherapy for rectal cancer. *N Engl J Med* 2004; 351:1731–1740
 7. Sauer R, Liersch T, Merkel S, et al. Preoperative versus postoperative chemoradiotherapy for locally advanced rectal cancer: results of the German CAO/ARO/AIO-94 randomized phase III trial after a median follow-up of 11 years. *J Clin Oncol* 2012; 30:1926–1933
 8. Vecchio FM, Valentini V, Minsky BD, et al. The relationship of pathologic tumor regression grade (TRG) and outcomes after preoperative therapy in rectal cancer. *Int J Radiat Oncol Biol Phys* 2005; 62:752–760
 9. Lee JH, Kim SH, Jang HS, et al. Preoperative elevation of carcinoembryonic antigen predicts poor tumor response and frequent distant recurrence for patients with rectal cancer who receive preoperative chemoradiotherapy and total mesorectal excision: a multi-institutional analysis in an Asian population. *Int J Colorectal Dis* 2013; 28:511–517
 10. Vukobrat-Bijedic Z, Husic-Selimovic A, Sofic A, et al. Cancer antigens (CEA and CA 19-9) as markers of advanced stage of colorectal carcinoma. *Med Arch* 2013; 67:397–401
 11. Park JS, Huh JW, Park YA, et al. A circumferential resection margin of 1 mm is a negative prognostic factor in rectal cancer patients with and without neoadjuvant chemoradiotherapy. *Dis Colon Rectum* 2014; 57:933–940
 12. Nikberg M, Kindler C, Chabok A, Letocha H, Shetye J, Smedh K. Circumferential resection margin as a prognostic marker in the modern multidisciplinary management of rectal cancer. *Dis Colon Rectum* 2015; 58:275–282
 13. Courtney ED, West NJ, Kaur C, et al. Extramural vascular invasion is an adverse prognostic indicator of survival in patients with colorectal cancer. *Colorectal Dis* 2009; 11:150–156
 14. Bugg WG, Andreou AK, Biswas D, Toms AP, Williams SM. The prognostic significance of MRI-detected extramural venous invasion in rectal carcinoma. *Clin Radiol* 2014; 69:619–623
 15. Sohn B, Lim JS, Kim H, et al. MRI-detected extramural vascular invasion is an independent prognostic factor for synchronous metastasis in patients with rectal cancer. *Eur Radiol* 2015; 25:1347–1355
 16. Kim JE, Lee JM, Baek JH, et al. Differentiation of poorly differentiated colorectal adenocarcinomas from well- or moderately differentiated colorectal adenocarcinomas at contrast-enhanced multidetector CT. *Abdom Imaging* 2015; 40:1–10
 17. Tong T, Yao Z, Xu L, et al. Extramural depth of tumor invasion at thin-section MR in rectal cancer: associating with prognostic factors and ADC value. *J Magn Reson Imaging* 2014; 40:738–744
 18. Cho SH, Kim SH, Bae JH, et al. Prognostic stratification by extramural depth of tumor invasion of primary rectal cancer based on the Radiological Society of North America proposal. *AJR* 2014; 202:1238–1244
 19. de Jong EA, ten Berge JC, Dwarkasing RS, Rijkers AP, van Eijck CH. The accuracy of MRI, endorectal ultrasonography, and computed tomography in predicting the response of locally advanced rectal cancer after preoperative therapy: a metaanalysis. *Surgery* 2016; 159:688–699
 20. Tsai C, Hague C, Xiong W, et al. Evaluation of endorectal ultrasound (ERUS) and MRI for prediction of circumferential resection margin (CRM) for rectal cancer. *Am J Surg* 2017; 213:936–942
 21. Koh DM, Collins DJ. Diffusion-weighted MRI in the body: applications and challenges in oncology. *AJR* 2007; 188:1622–1635
 22. Sun Y, Tong T, Cai S, Bi R, Xin C, Gu Y. Apparent diffusion coefficient (ADC) value: a potential imaging biomarker that reflects the biological features of rectal cancer. *PLoS One* 2014; 9:e109371
 23. Ha HI, Kim AY, Yu CS, Park SH, Ha HK. Locally advanced rectal cancer: diffusion-weighted MR tumour volumetry and the apparent diffusion coefficient for evaluating complete remission after preoperative chemoradiation therapy. *Eur Radiol* 2013; 23:3345–3353
 24. Curvo-Semedo L, Lambregts DM, Maas M, Beets GL, Caseiro-Alves F, Beets-Tan RG. Diffusion-weighted MRI in rectal cancer: apparent diffusion coefficient as a potential noninvasive marker of tumor aggressiveness. *J Magn Reson Imaging* 2012; 35:1365–1371
 25. Akashi M, Nakahusa Y, Yakabe T, et al. Assessment of aggressiveness of rectal cancer using 3-T MRI: correlation between the apparent diffusion coefficient as a potential imaging biomarker and histologic prognostic factors. *Acta Radiol* 2014; 55:524–531
 26. Elmi A, Hedgire SS, Covarrubias D, Abtahi SM, Hahn PF, Harisinghani M. Apparent diffusion coefficient as a non-invasive predictor of treatment response and recurrence in locally advanced rectal cancer. *Clin Radiol* 2013; 68:e524–e531
 27. Nougaret S, Vargas HA, Lakhman Y, et al. Intravoxel incoherent motion-derived histogram metrics for assessment of response after combined chemotherapy and radiation therapy in rectal cancer: initial experience and comparison between single-section and volumetric analyses. *Radiology* 2016; 280:446–454
 28. Le Bihan D, Breton E, Lallemand D, Aubin ML, Vignaud J, Laval-Jeantet M. Separation of diffusion and perfusion in intravoxel incoherent motion MR imaging. *Radiology* 1988; 168:497–505
 29. Hu YC, Yan LF, Wu L, et al. Intravoxel incoherent motion diffusion-weighted MR imaging of gliomas: efficacy in preoperative grading. *Sci Rep* 2014; 4:7208
 30. Hwang EJ, Lee JM, Yoon JH, et al. Intravoxel incoherent motion diffusion-weighted imaging of pancreatic neuroendocrine tumors: prediction of the histologic grade using pure diffusion coefficient and tumor size. *Invest Radiol* 2014; 49:396–402
 31. Kuru TH, Roethke MC, Stieltjes B, et al. Intravoxel incoherent motion (IVIM) diffusion imaging in prostate cancer: what does it add? *J Comput Assist Tomogr* 2014; 38:558–564
 32. Woo S, Lee JM, Yoon JH, Joo I, Han JK, Choi BI. Intravoxel incoherent motion diffusion-weighted MR imaging of hepatocellular carcinoma: correlation with enhancement degree and histologic grade. *Radiology* 2014; 270:758–767
 33. Lai V, Li X, Lee VH, et al. Nasopharyngeal carcinoma: comparison of diffusion and perfusion characteristics between different tumour stages using intravoxel incoherent motion MR imaging. *Eur Radiol* 2014; 24:176–183
 34. Lee HJ, Rha SY, Chung YE, et al. Tumor perfusion-related parameter of diffusion-weighted magnetic resonance imaging: correlation with histological microvessel density. *Magn Reson Med* 2014; 71:1554–1558
 35. Surov A, Meyer HJ, Höhn AK, et al. Correlations between intravoxel incoherent motion (IVIM) parameters and histological findings in rectal cancer: preliminary results. *Oncotarget* 2017; 8:21,974–21,983
 36. Sun H, Xu Y, Xu Q, Shi K, Wang W. Rectal cancer: short-term reproducibility of intravoxel incoherent motion parameters in 3.0T magnetic resonance imaging. *Medicine (Baltimore)* 2017; 96:e6866
 37. Nougaret S, Reinhold C, Mikhael HW, Rouanet P, Bibeau F, Brown G. The use of MR imaging in treatment planning for patients with rectal carcinoma: have you checked the “DISTANCE”? *Radiology* 2013; 268:330–344
 38. Edge SB, Compton CC. The American Joint Committee on Cancer: the 7th edition of the AJCC cancer staging manual and the future of TNM. *Ann Surg Oncol* 2010; 17:1471–1474
 39. Attenberger UI, Pilz LR, Morelli JN, et al. Multiparametric MRI of rectal cancer: do quantitative functional MR measurements correlate with radiologic and pathologic tumor stages? *Eur J Radiol* 2014; 83:1036–1043
 40. Duong TQ, Kim SG. In vivo MR measurements of regional arterial and venous blood volume fractions in intact rat brain. *Magn Reson Med* 2000; 43:393–402
 41. Guiu B, Petit JM, Capitan V, et al. Intravoxel inco-

IVIM-MRI of Rectal Cancer

- herent motion diffusion-weighted imaging in non-alcoholic fatty liver disease: a 3.0-T MR study. *Radiology* 2012; 265:96–103
42. Hayano K, Shuto K, Koda K, Yanagawa N, Okazumi S, Matsubara H. Quantitative measurement of blood flow using perfusion CT for assessing clinicopathologic features and prognosis in patients with rectal cancer. *Dis Colon Rectum* 2009; 52:1624–1629
43. Goh V, Halligan S, Wellsted DM, Bartram CI. Can perfusion CT assessment of primary colorectal adenocarcinoma blood flow at staging predict for subsequent metastatic disease? A pilot study. *Eur Radiol* 2009; 19:79–89
44. Sun H, Xu Y, Yang Q, Wang W. Assessment of tumor grade and angiogenesis in colorectal cancer: whole-volume perfusion CT. *Acad Radiol* 2014; 21:750–757
45. Lemke A, Laun FB, Simon D, Stieltjes B, Schad LR. An in vivo verification of the intravoxel incoherent motion effect in diffusion-weighted imaging of the abdomen. *Magn Reson Med* 2010; 64:1580–1585
46. Mizukami Y, Ueda S, Mizumoto A, et al. Diffusion-weighted magnetic resonance imaging for detecting lymph node metastasis of rectal cancer. *World J Surg* 2011; 35:895–899
47. Boss A, Martirosian P, Schraml C, et al. Morphological, contrast-enhanced and spin labeling perfusion imaging for monitoring of relapse after RF ablation of renal cell carcinomas. *Eur Radiol* 2006; 16:1226–1236
48. Breen MS, Lazebnik RS, Fitzmaurice M, Nour SG, Lewin JS, Wilson DL. Radiofrequency thermal ablation: correlation of hyperacute MR lesion images with tissue response. *J Magn Reson Imaging* 2004; 20:475–486
49. Andreou A, Koh DM, Collins DJ, et al. Measurement reproducibility of perfusion fraction and pseudodiffusion coefficient derived by intravoxel incoherent motion diffusion-weighted MR imaging in normal liver and metastases. *Eur Radiol* 2013; 23:428–434

协和医生访学日本，同样拼命工作的日本医生，待遇和我们有何不同？

海外访学 好医生 2018-10-01



好医生国际教育

专业 / 高效 / 低费 / 高质

出国访学 医路无忧

//

2017年4月有幸获得笹川奖学金资助，到日本冲绳“琉球大学医学研究科放射线诊断治疗学讲座”研修一年。

//

日本印象初体验

在来日本之前，我对冲绳的印象就只局限于“日本最南端的旅游城市”，另外因为历史上琉球王国的存在，对于这里有种莫名的好奇。



日本冲绳

冲绳包括许多离岛，与日本的本岛隔海相望，飞机行程大概两个半小时（羽田机场到那霸机场）。冲绳区域的公共交通远没有日本本岛便捷，出租车又超级贵，所以主要的交通工具其实是小汽车（私家车）。



冲绳单轨电车

我下了飞机，坐了一段单轨电车（モノレール）到达市中心之后，已经将近晚上十点，附近并没有直达琉球大学的公交车，山城先生把我安排到一家酒店住宿，等第二天让科里的椿本先生开车接我。

琉球大学附属医院所见所 感

别有特色的“懇親会”

琉球大学附属医院紧挨着琉大医学部，与琉球大学校本部稍微有点距离。琉大附属医院病床床位大概是600，和国内的医学院校附属医院相比，规模并不是很大，但只此一家，别无分号。

琉大的医学生大五开始下临床实习，大六中期就选择自己中意的科室。也许因为医学生数目不是很多，各个科室对于实习轮转学生都十分重视。我所在的放射科医局会给实习的学生订餐，会一对一给学生讲解报告的书写以及疾病诊断问题。



琉球大学附属医院

此外为了让更多的学生能够选择本科室，大概**每年七月开始陆续举办各种“懇親会”，宣传介绍本科室**。当然只有“懇親会”这种官方宣传是不够的。这时候本科室去年新入职的“前辈们”，就成了亲善大使，会和这些大六的后辈们有着各种形式私下小聚会（费用医局给予报销），解答后辈的疑问，介绍科室优势，尽可能的为科室招揽新人。总之，**整体感觉医学生很抢手。**

e

对于入职新人，科室也是很大胆的委以重任。每年的“懇親会、忘年会”等都是由前一年入职的新人筹备。事无巨细，从海报，聚会安排【一般分为聚餐会（19:00-21:00），饮酒会（21:00-23:00）以及唱K三场（23:00以后）】，聚会地点预订，每个聚会时段人数变动的统计，甚至聚会地点转移Taxi预订都是由他们安排。所以新人们其实压力都很大，但正是这种方式，强而有力地将新人融入到科室集体中。

自我介绍是一种礼仪

到了琉大放射科之后，第一个感受，自我介绍很重要。第一天到放射科医局的时候，就发现在医局通知栏那个位置，贴着之前我和村山教授在会议上的合影，上面标注着我的名字以及我要来琉大的日期。

村山教授先带着我在全科上下转了一圈，紧接着就是各种场合的自我介绍，包括本科室每周例会，和别的医院一起举办的学术会议，以及年末的琉球放射年会。也正是这样，一次次正式场合的自我介绍，让我对自己的存在，莫名有了一种底气，不再畏惧人前说话。也许会有人说，因为你是外国人所以会这样。其实并不是，来科室轮转实习的学生、进修医生、新调来的医生，**大家都要在这样正式场合一次次做自我介绍。对于日本人来说，好像这就是一项基本的礼仪。**

日本医院的仪式感

因为我的到来，科室的大BOSS村山教授办了一个欢迎会，聚餐的地方还特意选择了一个中华料理店（说来好笑，这是一个大阪人，在东京学艺，到冲绳开了一家中华料理店）。

来这边没多久，科室的奈々絵先生要去美国进修，同时岡田先生升迁到日本大学任教授，科室为两人举办了送别会（或者叫壮行会），壮行会上村山教授发言并送礼物。除了值班老师外，放射科几乎全员参加。



岡田先生（右一）的壮行会

从左至右依次是：椿本先生，村山教授，我，岡田先生

新年放假前（日本是按照阳历进行算，12月底到一月初，有1周的样子），在放射科休息室（医院内），几乎所有技师，大夫以及护士都集聚一起，搞了一个简单的年终聚会。教授和技师长简单总结一年工作，并和大家一起举杯，祝福大家新年快乐。年假结束，在相同的地方，大家又一起举杯迎接新一年的开始。



像这样无论是一个人的到来和离去，还是一年的开始和结束，日本人都会满怀真诚，认真对待。也许多年以后记不得中间的情节，但是在某个特别的节点，大家一

起欢笑，一起祝福，一起举杯的场景总会让人不自主想起，分外留恋。用稍微郑重的方式，好好开始认真告别，感恩相遇，这是身边的日本人用行动告诉我的生活方式。

拼命工作，放开玩

日本人工作很拼命，但是玩的时候也很放得开。

周一到周五午餐时间（一个小时），会有读文献学习或者病例讨论。中午不休息，边吃饭边学习，好像是种常态。在国内一直是“中午不睡，下午崩溃”的我，刚到这边的时候，完全无法适应，全靠咖啡提神，后来好久才调整过来。日本国内年初到年末有各种大大小小的会议，不过这边的老师基本都有自己的研究方向，一般只挑选自己领域的会议参加。倒是教授会忙一些，他被邀请做各种大会的座长、发言人，经常出差。

我的带教山城先生，典型对工作“热衷”的人，一年365天几乎无休。聚会11点结束后，依然要去医局。黄金周大家放假，他坐飞机去南美开放射学年会。医局有个不是笑话的笑话，有人问：山城先生在干嘛？（不分时候），答：山城先生在写论文。如此调侃山城先生是工作狂。



话说自己还闹了一个笑话，日本开学术会议最后一般都会有个“情报交流会”，我一开始以为是属于学术交流会，穿的很正式，兴冲冲地跑去参加，后来发现其实就是聚餐，不过是自助餐形式，你可以边吃饭边和身边人搭讪。当然如果这时候你有看到心仪崇拜的教授或者老师，这是个绝佳的套磁机会。

但是无论平时多严肃的老师，到了聚会活动的时候好像都会换一个样子。**健谈，拼酒，甚至是乐器演奏，随手就来。**K歌一唱就到后半宿，然后东倒西歪的坐上计程车回家（真心为冲绳良好的治安点赞）。当然拼酒并不是男人的特权，这边医局的有两三位女老师酒量也是好的惊人，到了飲み会，豪饮的做派丝毫不输给男同事。**也许平时太一本正经，玩的时候又如此放得开，反差实在太有冲击力。**

放射科的日常点滴

第四点感触比较深的，与琉大附院放射科老师工作相关。

这边社区的基础医疗做的很好，重病疑难病才会被转送到琉大附院，所以和国内相比，这边放射科医生的临床工作量真算的上轻松。另外，周一到周五5个工作日内，有1.5天算是他们的个人的科研时间，由自己安排，因而他们相对有更多时间专心做科研方面的工作。

放射诊断、治疗、介入以及核医学都属于放射线科，每周三有疑难病例的集体讨论（包括上面各个方面的），放射科医师基本都会参加。讨论结束后，如果近期需要外出开会发言的老师，会将PPT提前试讲一下，然后由大家一起挑问题。经过这么集体的“审核”后，才会拿到外面讲演。

此外，在日本国内学会上发表的内容，日本老师更注重的是经验总结以及知识的传

承，而不是研究领域新技术相关探索性研究。这边老师带教都很耐心，无论是对实习学生还是新入职的后辈，一步步的讲解，直到你明白为止。我的带教老师山城先生平时不苟言笑，很是严肃，简直是移动的冰山，但只要是专业上的问题请教他，他会很耐心讲解，不会因为有其他事情要做就敷衍了事，在他看来这是他工作的一部分。

PS. 有一次还认真地纠正了我的英文发音半天，感觉超级囧。他在美国波士顿进修过两年，英文比较纯正。



39期笹川奨学金研修生合影

除此以外，其他的日本老师和staff给予了我很多帮助，感觉自己一直被温暖地“守护着”，经常被他们的小细节感动到。跟着椿本先生去超市大采购，跟随與儀先生参加与美国驻军医生的联谊Party，和城间女士观看首里城祭り并且吃到最地道的冲绳料理，一点一滴他们给予了我最大的善意和帮助。

当繁忙的工作按下暂停键

这次来日本的研修，就像给繁忙的临床工作按了一下暂停键。从有些慵懒的舒适区跳到了一个完全陌生环境里，从最初到手忙脚乱到后面的渐渐习惯，自己多多少少会受到周围日本老师的影响，也在潜移默化接受他们的一些理念。

无论是日本还是中国，医生都不是一个轻松的行业。虽然医疗制度不同，从业环境也有差异，但从周围日本老师身上，依然能够汲取适合自己的正能量，希望借此可以更顺畅的走好下面的路。

投稿来源：中日友好医院放射科 徐妍妍

后记

国外医疗有很多值得我们借鉴学习的地方，医院只有依赖高素质、高质量专业技术人才，才能综合提升医院核心竞争力和可持续发展潜力，最终造福患者。医生个人也只有抓住机遇不断突破自我，才能拥有更广阔职业发展空间。

好医生国际教育专注于**医疗教育18年**，依托长年积累的优势资源，帮助无数医生拿到海外名校的访学邀请函，在**美国、英国、德国、日本**等医疗水平先进的国家有**众多成功案例**。好医生为助力医生的梦想而感到自豪。如果您也有一颗勇于攀登的心，请**点击下方“阅读原文”，开启访学之行！**

往期回顾

案例 | 5年工作经验的住院医，2周斩获哈佛医学院offer

案例 | 主治医师是如何收到牛津大学访学邀请函的？

热点 | 见证德国医院300多台手术，我明白了中国医疗为何摆脱不了“成长壁垒”

公益財団法人日中医学協会
TEL 03-5829-9123
FAX 03-3866-9080
〒101-0032 東京都千代田区岩本町 1-4-3
住 泉 K M ビ ル 6 階
URL : <https://www.jpcnma.or.jp/>